Degassing Processes at Persistently

Active Explosive Volcanoes

by

Jean-François Smekens

A Dissertation Presented in Partial Fulfillment
of the Requirements for the Degree
Doctor of Philosophy

Approved April 2015 by the
Graduate Supervisory Committee:

Amanda Clarke, Chair
Stanley Williams
Michael Burton
Philip Christensen
Gordon Moore
Jonathan Fink

ARIZONA STATE UNIVERSITY

May 2015

ABSTRACT

Among volcanic gases, sulfur dioxide (SO_2) is by far the most commonly measured. More than a monitoring proxy for volcanic degassing, SO_2 has the potential to alter climate patterns. Persistently active explosive volcanoes are characterized by short explosive bursts, which often occur at periodic intervals numerous times per day, spanning years to decades. SO_2 emissions at those volcanoes are poorly constrained, in large part because the current satellite monitoring techniques are unable to detect or quantify plumes of low concentration in the troposphere. Eruption plumes also often show high concentrations of ash and/or aerosols, which further inhibit the detection methods. In this work I focus on quantifying volcanic gas emissions at persistently active explosive volcanoes and their variations over short timescales (minutes to hours), in order to document their contribution to natural SO_2 flux as well as investigate the physical processes that control their behavior.

In order to make these measurements, I first develop and assemble a UV ground-based instrument, and validate it against an independently measured source of SO_2 at a coal-burning power plant in Arizona. I establish a measurement protocol and demonstrate that the instrument measures SO_2 fluxes with < 20 % error. Using the same protocol, I establish a record of the degassing patterns at Semeru volcano (Indonesia), a volcano that has been producing cycles of repeated explosions with periods of minutes to hours for the

past several decades. Semeru produces an average of 21-71 tons of SO_2 per day, amounting to a yearly output of 8-26 Mt.

Using the Semeru data, along with a 1-D transient numerical model of magma ascent, I test the validity of a model in which a viscous plug at the top of the conduit produces cycles of eruption and gas release. I find that it can be a valid hypothesis to explain the observed patterns of degassing at Semeru. Periodic behavior in such a system occurs for a very narrow range of conditions, for which the mass balance between magma flux and open-system gas escape repeatedly generates a viscous plug, pressurizes the magma beneath the plug, and then explosively disrupts it.

DEDICATION

To Bernard Beaujant, for unwittingly

inspiring a life changing adventure

ACKNOWLEDGMENTS

TABLE OF CONTENTS

LIST OF TABLES

LIST OF FIGURES

CHAPTER 1

INTRODUCTION

Persistent volcanic activity occurs at a number of volcanic centers around the globe. Based on of the longevity of this type of activity, it is thought to be the manifestation of an open (or at least semi-open) volcanic system where the magma is allowed to degas before or during its transport to the surface. The resulting activity often occurs in the form of lava flows or explosive activity of low magnitude (e.g., Hawaii, Reunion island, Stromboli volcano, all extremely active in the last 100+ years). This behavior is to be contrasted with systems where gases remain trapped in the magma until it reaches the surface and culminates in sometimes extremely violent explosions (e.g., Mount St-Helens in 1980, Pinatubo in 1991, Redoubt in 2009 or Chaiten in 2010), often manifesting in systems of silicic composition. But persistent activity is not limited to basaltic systems. Volcanic centers that have been the site of major explosive eruptions often go through phases of open-system activity. The higher viscosity typically associated with the magmas of those systems leads to a type of semi-open system, which in this work I call persistently active explosive activity. Small explosions (vulcanian or strombolian) are common at many volcanoes of intermediate composition. They consist of short-lived, discrete explosions, generally assumed to represent the sudden decompression of an overpressured, vesiculated magma (Self et al., 1979). The cause for this sudden release of volatiles can be one of several mechanisms. Repeated explosions at
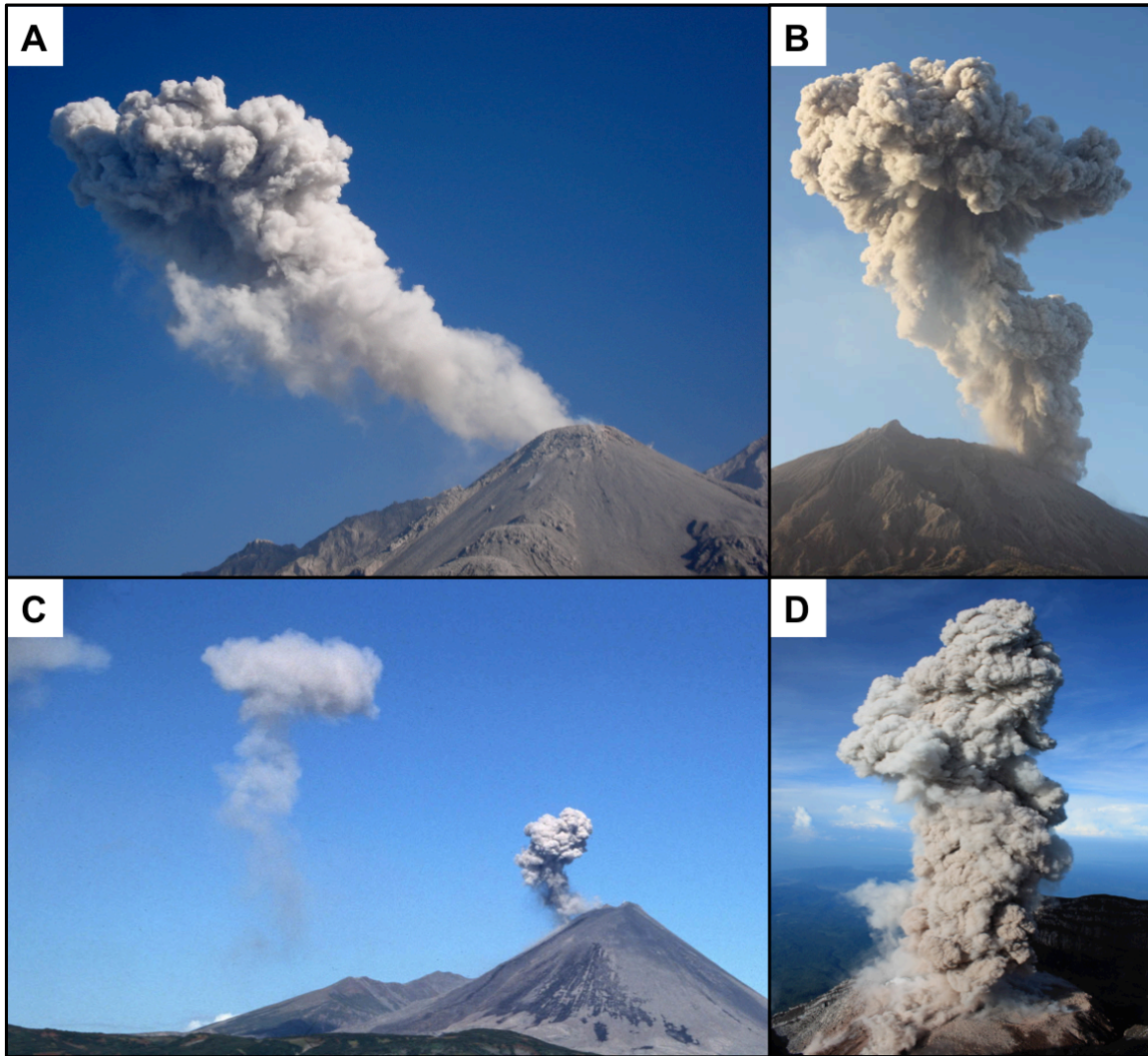
Figure 1.1: Examples of typical activity at selected persistently active explosive volcanoes: A) Santiaguito in 2007; B) Sakurajima in 2009; C) Karymsky in 2010; and D) Semeru in 2013.

Stromboli volcano, for example, are attributed to the coalescence of exsolved bubbles at the top of a shallow magma chamber, forming large bubbles which are periodically evacuated through the conduit and to the surface vent, a mechanism sometimes referred to as "slug flow" (Jaupart and Vergniolle, 1988). In more silicic (and more viscous) systems, a model known as "stick-slip" has been proposed (e.g., Barmin et al., 2002; Bluth and Rose, 2004; Lensky et al., 2008), in which a dense, viscous plug exists at the top of the conduit, preventing the free flow of volatiles to the surface. When the overpressure created beneath the plug ultimately overcomes the friction forces generated by the plug on the conduit walls, the plug is quickly extruded, or sometimes destroyed in an explosive fashion. This can generate shock waves and the expulsion of ballistics. A fragmentation wave descends along the conduit and disrupts the magma into a gas-pyroclast mixture, producing a buoyant column that may or may not collapse to form pyroclastic flows. The resulting Vulcanian explosions typically last seconds to minutes, erupting volumes less than 0.1 km^3 DRE in columns usually less than 10 km tall – although occasionally columns as high as 20 km have been observed (Morrissey and Mastin, 2000). Moreover the explosions usually occur in groups, with individual explosions separated by periods of minutes to days. This type of periodic explosive activity has often been observed as the transition between effusive and sustained explosive activity (e.g., Hoblitt et al., 1996; Hoblitt, 1986; Stix et al., 1997), although controls on the frequency and scale of explosions are not well constrained (Jaquet et al., 2006; Mason et al., 2006; Melnik and Sparks, 2002). Some volcanoes experience cyclic explosive activity on a regular basis for decades (e.g. Santiaguito in Guatemala, Semeru

3

in Indonesia, Karymsky in Russia, Sakurajima in Japan and others). They are of somewhat lower intensity but the regularity (and therefore predictability) of their eruptive behavior makes such volcanoes ideal objects for detailed observation of the dynamics of explosive eruptions.

Recent development in monitoring technologies and information communication has increased the awareness of persistently active explosive activity and forced the volcanology community to reevaluate their relative contribution to the global volcanic activity. Figure 1.2 shows a chart of the frequency of eruptions per year during the 20th century. The rate of occurrence of eruptions of smaller magnitude (Volcanic Explosivity Index - VEI<3) appears to be rising over the last decade. This apparent rise is likely the result of a sampling bias because small explosions such as those that are the subject of this work are now simply easier to detect or report. In either case, it is becoming evident that these eruptions must be studied in greater detail. Although the hazards they present are not as great as those of larger explosions, they can potentially affect a large number of people. Their relatively low hazards impact, combined with the repetitive nature of their activity, also presents an opportunity to study the physical parameters that control volcanic explosions, using the volcanoes as natural laboratories. In this work I strive to quantify the emissions of volcanic gases at the vent of persistently active explosive volcanoes and their temporal variability, in an effort to understand their role in constraining the conditions that lead to and control explosive eruptions. In particular I will focus on the measurement of sulfur dioxide (SO_2).
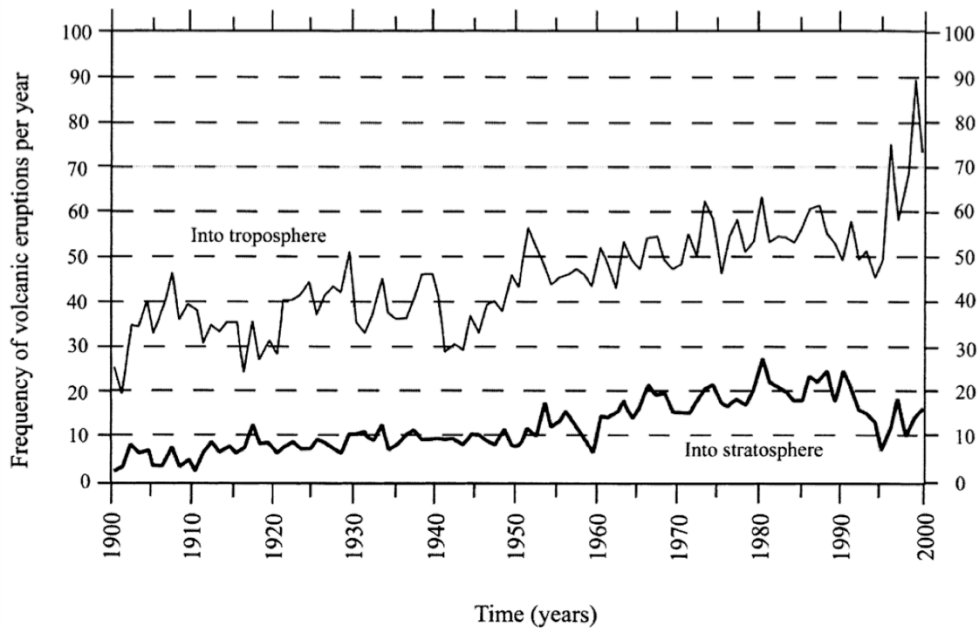
Figure 1.2: Frequency of volcanic eruptions from 1900 to 2000, divided based on their explosivity between explosions of VEI < 3 (thin line) and VEI > 3 (thick line). From Halmer et al. (2002).

In addition to the relevance of SO_2 emissions to volcanic processes, sulfate aerosols generated from the oxidation of sulfur-rich gases such as SO_2 have a potential influence on regional and global climate. The exact effect of sulfur dioxide on climate is not perfectly understood but the most accepted theory is that large amounts of SO_2 injected into the stratosphere have a cooling effect on surface temperature (see Figure 1.3). Sulfur-rich gases such as SO_2 and H_2S - the two most abundant sulfuric volcanic gases – are oxidized into sulfates to form aerosols that have a long residence time in the atmosphere, increasing cloud reflectivity and cooling the climate. Global cooling has been observed after large eruptions throughout the geologic (eg., Toba, 73.5 ky, Rampino

5

and Self, 1992) and historic records (e.g., Tambora, 1815, Oppenheimer, 2003; Pinatubo, 1991, Robock, 2002). Other natural sources of SO_2 include biological decay and forest fires. More recently however, human activities have become significant producers of sulfur-rich gases, mostly as a result of fossil fuel burning. In this regard it is crucial to constrain the exact contribution of human and individual natural sources such as volcanic activity in order to assess their total impact on global climate.

Studies have been conducted to estimate the amount of SO_2 produced by volcanic activity worldwide and its variability over a range of time periods. Such studies rely on sporadic measurements from the ground and, more recently, from satellite instruments. However the lack of continuous data over protracted periods of time has forced scientists to make assumptions and generalizations in their estimates that result in significant errors. This is particularly true in the case of volcanoes that exhibit low levels of activity for protracted periods of time. Table 1.1 presents a list of selected estimates of global volcanic SO_2 emissions. These estimates vary greatly and have improved with the rise of new technologies. But even the more recent studies produce significantly different numbers. With over 200 volcanoes active in the last 50 years and ~1500 centers active during the last 10,000 years, complete global coverage with ground-based instruments is unrealistic. Because of this lack of a complete data set, emission rates must be extrapolated in time and space, which can be done in many different ways. In the studies mentioned above, persistently active explosive volcanoes are often considered to make a negligible contribution to global SO_2 emissions, partly because their emissions are not
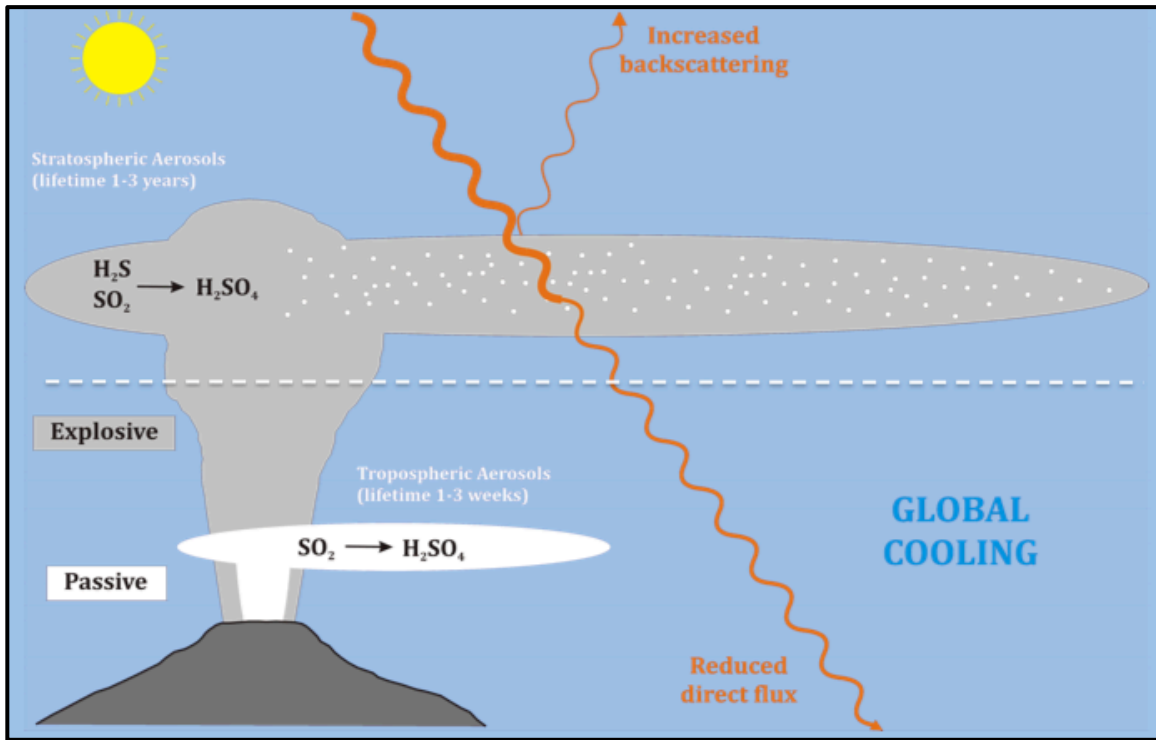
Figure 1.3: Schematic representation of the cooling effect of SO_2 on the climate.

SO_2 flux (Tg/yr)	Source
1.5	Kellogg et al. (1972)
10	Stoiber and Jepsen (1973)
6	Granat et al. (1976)
50	Le Guern (1982)
18.7	Stoiber et al. (1987)
13	Schnetzer (1993)
28 ± 12	Graf et al. (1997)
13	Andres and Kasgnoc (1998)
15-21	Halmer et al. (2002)

Table 1.1: Selected estimates of global volcanic SO_2 flux (in chronological order). Note the more than 1 order of magnitude spread in values.

very well constrained. A secondary objective of this work is to try and estimate the typical SO_2 emissions produced by this type of activity.

Chapters 2 and 3 describe the development, validation and application of a new tool for the monitoring of volcanic degassing from the ground. The SO_2 camera is capable of measuring sulfur dioxide emissions with an unprecedented sampling frequency. SO_2 is typically the third most abundant volatile species released from volcanoes, after H_2O and CO_2. Although it usually constitutes < 5% of the total gasses emitted (e.g., Burton et al., 2007) SO_2 is virtually absent from the background atmosphere, which together with a strong absorption band in the ultraviolet where scattered sunlight is abundant, makes it an ideal target gas to monitor volcanic emissions. Measurements of SO_2 emissions, whether ground-, air- or space-based, have been an integral part of monitoring networks at restless volcanoes for the past 40 years, and this era has seen the development of a variety of spectroscopic methods to detect and quantify SO_2 emissions from the ground such as the Correlation Spectrometer (COSPEC - Stoiber et al., 1983) or methods of Differential Optical Absorption Spectroscopy (e.g., Galle et al., 2003). Recently UV imaging techniques have emerged, commonly referred to as SO_2 cameras (e.g., Bluth et al., 2007; Kantzas et al., 2010; Mori and Burton, 2006; Tamburello et al., 2013). In chapter 2 I summarize my efforts in the development of my own version of the instrument and processing software, as well as the validation of the method against an independently measured source of SO_2 at a coal-burning power plant in Arizona. Chapter 3 presents the results of a measurement campaign using the SO_2

camera at Semeru volcano, Indonesia. Semeru is a persistently active volcano on the island of Java, characterized by small explosions occurring at a frequency of several events per hour. These measurements are the first reported values for SO_2 emissions at Semeru.

Chapter 4 explores the possibility of using satellite instruments to monitor the emissions of persistently active explosive volcanoes. A number of instruments are available that have the ability to detect and quantify SO_2 from orbit, exploiting absorption features of the gas in either the ultraviolet or thermal infrared part of the spectrum. I present the advantages and limitations of the various methods before focusing on the retrieval of SO_2 from a selection of images taken with the Advanced Spaceborne Thermal Emission Radiometer over persistently active volcanoes.

Finally, in Chapter 5 I use a numerical model to study the conditions that lead to and control periodicity in a system of basaltic andesitic composition, and test the validity of a model in which a viscous plug at the top of the conduit controls the eruption cycles. Numerical models have been used to study a variety of eruption styles (e.g., Melnik and Sparks, 1999; Ozerov et al., 2003; Papale and Dobran, 1993). I modified a 1-D transient model originally developed to study eruptive cycles at the Soufrière Hills Volcano on Montserrat (de' Michieli Vitturi et al., 2013), for use with more mafic compositions, and use it to simulate the periodic formation and disruption of a viscous plug to reproduce the cycles of magma and gas emissions at Semeru.

CHAPTER 2

DEVELOPMENT AND VALIDATION OF A TOOL TO MEASURE SO$_2$ EMISSIONS

AT HIGH TEMPORAL RESOLUTION: THE SO$_2$ CAMERA

The results from this chapter have been published in a peer-reviewed journal and can be found under the reference below. My co-authors have given me permission to reproduce the work here in my dissertation.

SMEKENS, J-F., BURTON, M. R. and CLARKE, A. B. (2014): Validation of the SO$_2$ camera for high temporal and spatial resolution monitoring of SO$_2$ emissions. *J. Volcanol. Geotherm. Res.,* http://dx.doi.org/10.1016/j.jvolgeores.2014.10.014.

2.1 Introduction and Motivations

Many atmospheric gases present absorption features in the ultraviolet spectrum (see Figure 2.1), a result of electronic transitions in the outer layers of the molecules. These features can be exploited to detect and quantify molecular gases using spectroscopic methods, including sulfur dioxide (SO2). In the 1970's the Correlation Spectrometer (COSPEC) was developed, initially for the purpose of monitoring anthropogenic emissions (Moffat and Millan, 1971), and was then applied to the measurement of volcanic emissions (e.g., Stoiber et al., 1983; Williams et al., 1986). The instrument exploits the differential absorption of the SO$_2$ molecule at two wavelengths in the UV. The incoming light is dispersed with a diffraction grid. The difference in

intensity at two selected wavelengths is converted to a proportional voltage and the instrument is calibrated by placing gas cells of known concentration in the light path inside the instrument. Later, a method of Differential Optical Spectroscopy (DOAS) was developed with the emergence of the CCD and the ability to easily collect high-resolution spectra. Relying on the same principle of differential absorption, the DOAS method uses a forward modeling approach and measured cross-section of the SO_2 molecule attempting to fit the absorption features as measured by the spectrometer. Most recently, a new type of instruments has been developed (Mori and Burton, 2006), which use band-pass filters to produce 2D images of a drifting plume. These new instruments, to which I will refer as SO_2 cameras, allow for higher temporal resolution, and the accurate determination of wind speed, two parameters that have been important error sources in previous methodologies. The unprecedentedly high temporal resolution achieved with SO_2 cameras allows for direct comparison with geophysical data sets, and thus can be used to better understand shallow conduit eruptive processes (e.g., Holland et al., 2011; Mori and Burton, 2009) and plume dynamics (e.g., Yamamoto et al., 2008). UV imaging has been tested against other UV methods such as COSPEC through side-by-side measurement campaigns (e.g., Kantzas et al., 2010), and SO_2 emission rates measured by DOAS techniques have been validated against industrial sources in the past (e.g., Frins et al., 2011; Rivera et al., 2009). A first validation of an SO_2 camera against a controlled source can be found in Dalton et al. (2009), in which they focus on a comparison of path concentrations rather than emission rates. This study, however, represents the first validation exercise in which SO_2 emission rates measured by an imaging method are
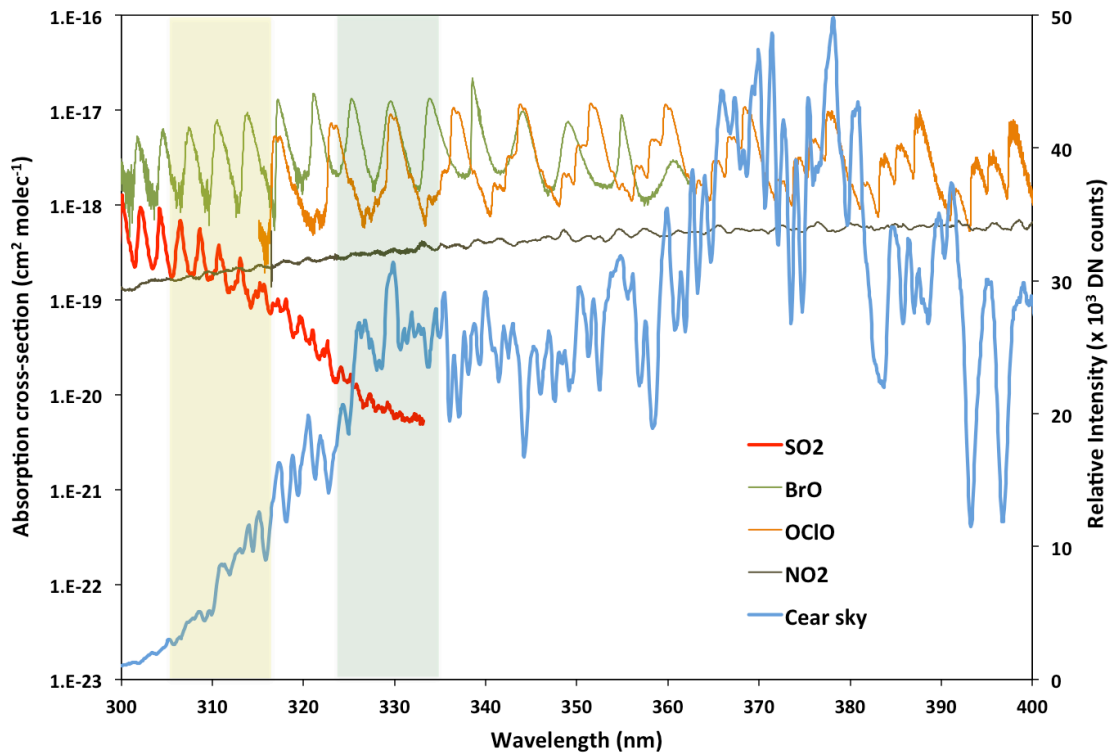
Figure 2.1: UV absorption spectra of various gaseous species of potential relevance to volcanic monitoring, shown over a spectrum of scattered sunlight. [blue] The sky spectrum was acquired with a USB2000+ spectrometer in Tempe on a clear day in October of 2011. [red] Sulfur dioxide - SO_2 (Vandaele et al., 1994); [green] Bromium oxide - BrO (Fleischmann et al., 2004); [orange] Symmetric chlorine dioxide - OClO (Kromminga et al., 1999); [brown] Nitrogen dioxide - NO_2 (Voigt et al., 2002). For reference, the bandwidths of the camera filters are shown with yellow (310 nm) and green (330 nm) rectangles.

compared against controlled SO_2 emissions that were independently measured using in-situ sensors.

The objective of this chapter is to validate, for the first time, the emission rates ($kg\ s^{-1}$, $t\ d^{-1}$) obtained with an SO_2 camera against an independently measured source of SO_2. Coal burning power plants are the largest anthropogenic contributors to global SO_2 emissions (Smith et al., 2011), and serve as reasonably scaled analogues of volcanic vents. In the US, SO_2 emissions from power plants are regulated and most facilities use SO_2 scrubbers to greatly reduce their emissions (> 90 % reduction), which while good for the environment makes them less ideal for comparison with volcanic sources. However, the Environmental Protection Agency (EPA) does make hourly data publicly available for all US plants. Data are accessible through an interactive query on the website of the Air Markets Program Data (AMPD - http://ampd.epa.gov/ampd/) where the time period, facilities and gas or gases of interest can be specified. On October 23rd, 2013, I measured the emissions of SO_2 from the two main stacks at the Cholla coal-burning power plant located near Joseph City, AZ, USA (see Figure 2.2). The plant is the second largest emitter in the state of Arizona, although its emissions are one to two orders of magnitude below the largest plants in the US. Its location makes for ideal observing conditions all year long, with clear skies nearly 280 days per year and a very dry atmosphere. According to the EPA data, the four stacks at the Cholla plant released a total of 5,065 tons of SO_2 in the year 2013, at an average daily emission rate of ~ 14 $t\ d^{-1}$. The emissions from the power plant are monitored using Continuous Emission Monitoring
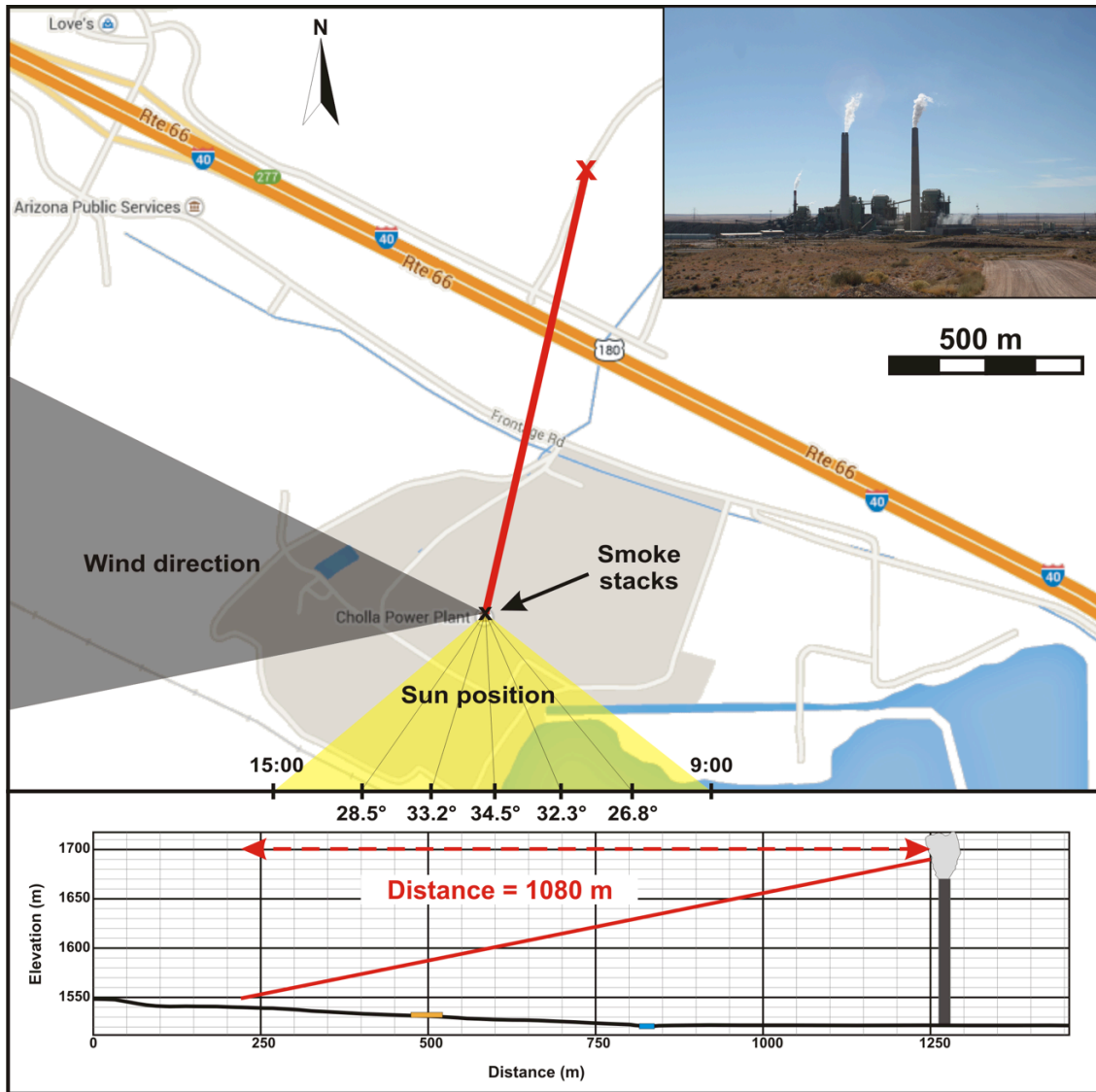
Figure 2.2: Location map and viewing geometry at the Cholla power plant on October 23rd, 2013. Measurements were taken from a position North of Interstate 40, at a distance of 1,080m from the exhaust stacks. The yellow cone represents the sun position relative to the stacks during the measurements. Tick marks are separated by 1h. The number reported below each tick mark is the elevation of the Sun at that time, or Solar Zenith Angle (SZA). The grey cone encloses the wind direction during that same period.

Sensors (CEMS) within the stacks. CEMS consist of an analyzer to measure concentration – typically a short-path UV absorption method – coupled with a volumetric flow meter. Measurements are taken every minute from gas sampled within the stack, and integrated to produce the hourly mass emission values reported by the EPA. Accounting for errors associated with both concentration and flow rate, the typical combined error for this type of measurement does not exceed 10%.

2.2 Methods

2.2.1 *Hardware*

The data was acquired with a custom system designed at the Istituto Nazionale di Geofisca e Vulcanologia in Pisa, and implemented at Arizona State University. Table 2.1 lists the components and their specifications and Figure 2.3 presents an annotated picture of the system. It consists of 2 Quantum Scientific Imaging (QSI) 620s high sensitivity cameras, with a 1600x1200 Kodak KAI-2020 charge-coupled device (CCD), and an Ocean Optics USB2000+ spectrometer. The KAI-2020 has a quantum efficiency of 6-9% between 300 and 400 nm; and a special UV coating was applied to the CCD, limiting the reflectance to less than 0.5% in the same spectral range. Each camera is equipped with a UV2528B quartz lens, from Universe Optics with an effective full angle field of view of ~30°, fitted with a set of UV bandpass filters centered at 310 and 330 nm, and with a ~10nm full width at half maximum. The 310 nm filter (A) is designed to capture the absorption features produced by the SO_2 molecules (Fig. 2.4). However the 310 nm band

is also susceptible to broadband absorptions due to the presence of aerosols or particulate matter. The second filter (B: 330 nm) captures these broadband absorptions, to produce an image that is used as a reference to isolate the signal produced by the SO_2.

I use an Ocean Optics 84-UV collimating lens with a focal length of ~100 mm to focus light onto a 400 μm fiber optic cable, which carries the light to the USB2000+ spectrometer. This UV telescope has an effective field of view of approximately 1°. The USB2000+ spectrometer is fitted with a #7 grating (groove density 2400 mm^{-1}) which diffracts light between 280-420nm onto a 2048 linear CCD, and offers a spectral resolution of 0.5 nm with an entrance slit of 50 μm. A custom frame was designed and built at the School of Earth and Space Exploration at ASU, to hold the cameras and ensure optimal alignment between the fields of view. The cameras are placed on top of one another so that the lenses are as close to one another as possible, and the alignment can be adjusted by pivoting each camera about its axis independently. The UV telescope is mounted on a ball mount, either above or beside the cameras, so that its relative field of view can be adjusted to point at a chosen portion of the camera image. In the processing stage, discussed below, any misalignment between the cameras is corrected and the exact location of the USB2000+ field of view in the resulting frames is determined.
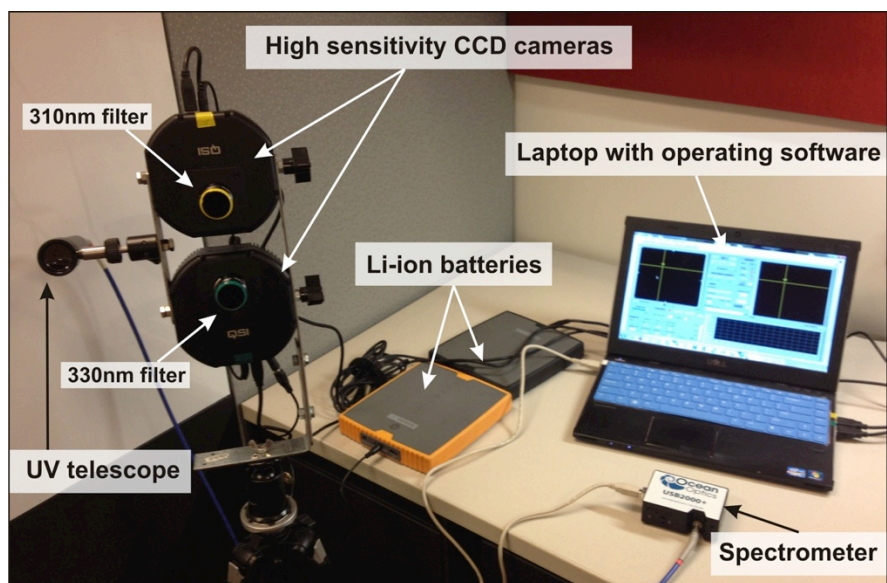
Figure 2.3: Photograph of the SO$_2$ camera system.

Manufacturer	Part	Specifications
Quantum Scientific Imaging	QSI 620s (x2)	1600x1200 CCD 6-9% quantum efficiency Anti reflection UV coating Mechanical + Electronic shutter USB interface
Ocean Optics	USB2000+ spectrometer	50 μm entrance slit Grating #7 (2400 grooves/mm) Spectral range: 280-420 nm Spectral resolution ~0.5nm
	84-UV collimating lens	100mm focal length Effective FOV: ~1°
	Fiber optic cable	400 μm diameter
Universe Optics	UV2528 B quartz lens (x2)	24.8mm effective focal length Effective FOV: 29.3° 25mm diameter C-mount thread
Asahi Spectra	XBPA310 band-pass filter	Center: 310nm FWHM: 10nm
	XBPA330 band-pass filter	Center: 330nm FWHM: 10nm
ASU	Custom steel frame	10.1"H x 4.7"W x 2.0"D

Table 2.1: List of system components and specifications.
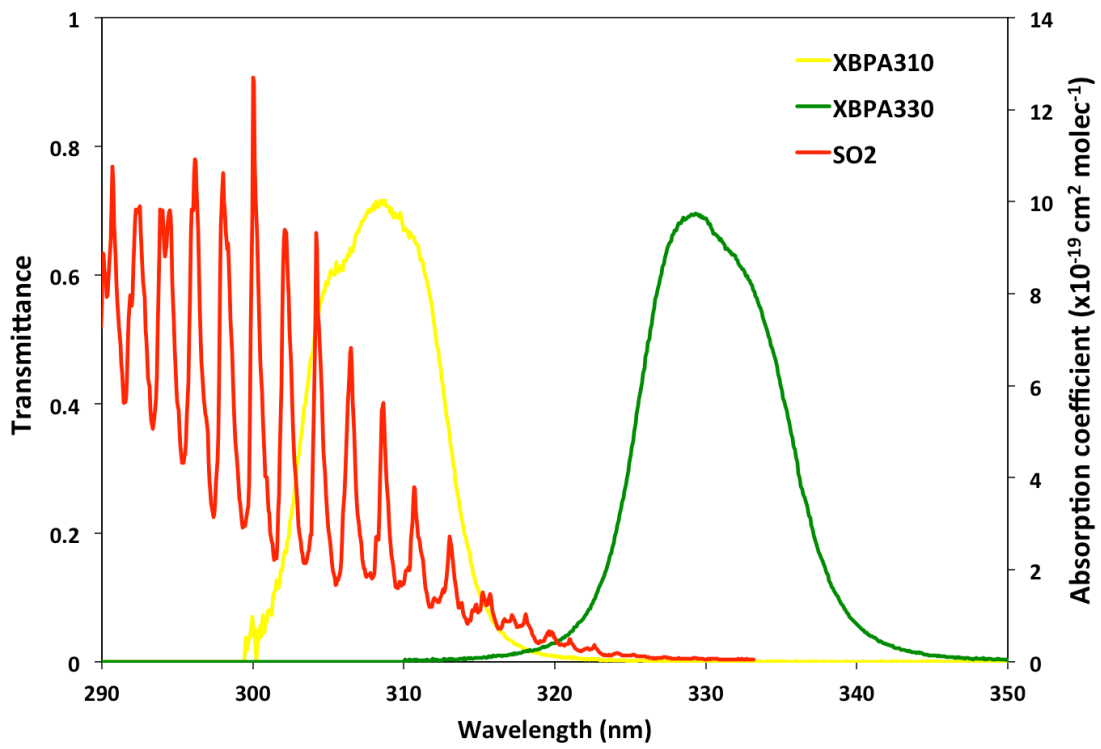
Figure 2.4: Measured transmittance response of the band-pass filters [scale on left]. An absorption spectrum of SO_2 (Vandaele et al., 1994) is superimposed for reference [scale on right].

2.2.2 Data Acquisition

The custom acquisition software was developed in Labview at Arizona State University, following on the work of Tamburello et al. (2011). The software is designed for synchronous acquisition by both cameras and the USB2000+ spectrometer. It includes control over acquisition parameters (exposure/integration time, instrument temperature for the CCDs, delay between frames, binning of the images), as well as real-time data displays for both cameras and the spectrometer. Dark and clear sky images and spectra are acquired at the beginning of each sequence, along with images of gas cells of known concentrations for calibration purposes.

2.2.3 Optical Depth Images

Data analysis is conducted using routines written in IDL (Interactive Data Language) and is summarized in Figure 2.5. First, I determine the misalignment on the images by performing a cross-correlation on a pair of synchronous images along 2 axis of translation and one axis of rotation. The resulting shift is then applied to the rest of the data set. Dark current images, acquired at the beginning of every sequence, are subtracted from every image. Because I use a temperature-controlled instrument, I assume dark current to remain constant throughout the sequence. The clear sky images show reduced intensity toward the edges (Fig 2.6), an effect that is the result of a change
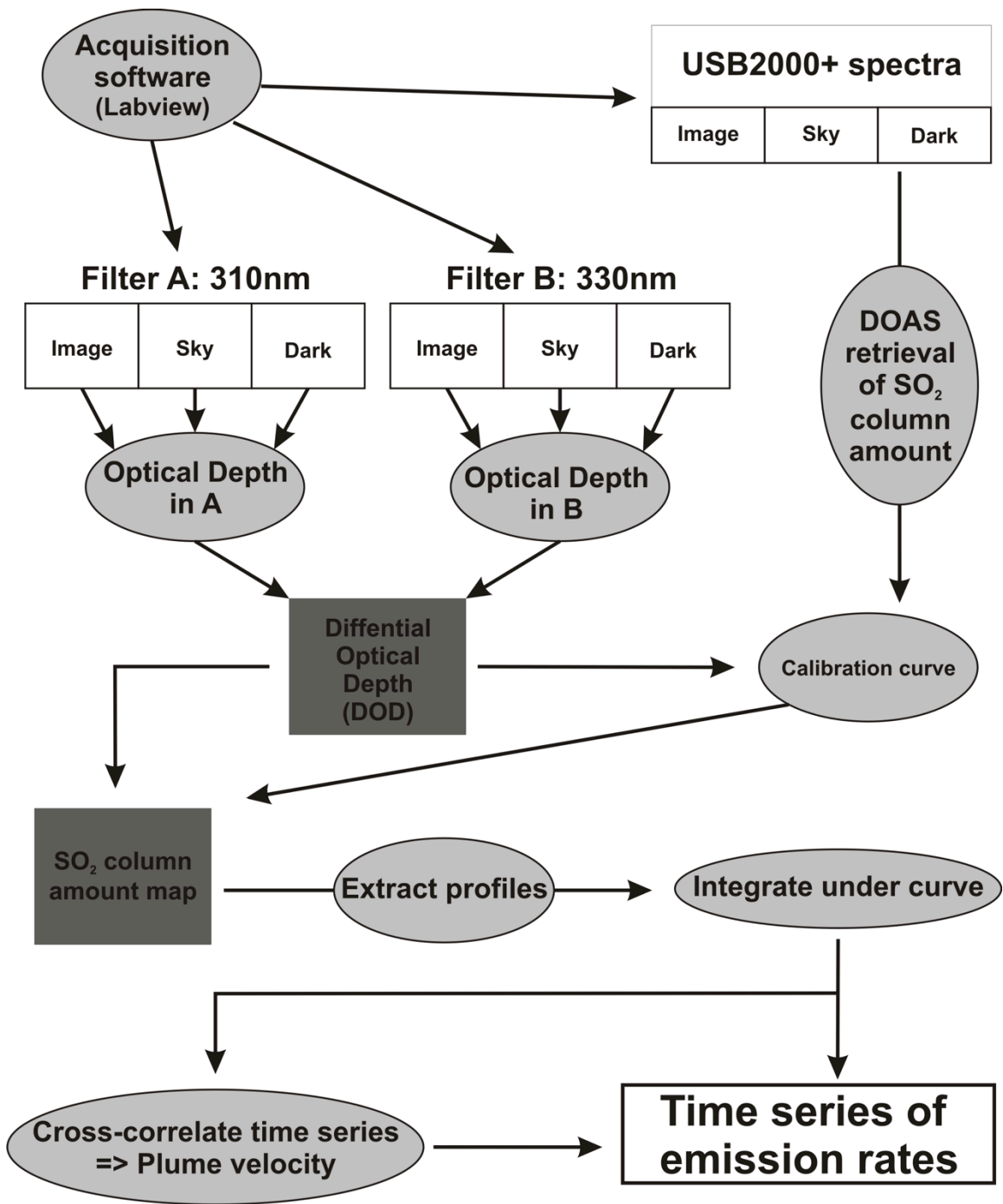
Figure 2.5 (previous page): Flow chart of data acquisition and analysis. The custom acquisition software is written in Labview and is compatible with various QSI camera models, and USB series spectrometers from Ocean Optics. It ensures synchronous acquisition of data on all three devices, and stores reference images and spectra (clear sky and dark) for use in the analysis. All processing scripts are written in IDL (Interactive Data Language).

in filter transmittance for off-axis incidence angles. The filter response at these higher incidence angles exhibits not only a decrease in overall transmittance, which explains the pattern of reduced brightness, but also a shift in frequency response towards shorter wavelengths (Kern et al., 2013). The frequency shift has very little effect on filter B, where SO_2 presents no absorption features and only broadband absorptions from aerosols and particulates are measured. For filter A, however, the shift effectively moves the transmittance window into an area of the spectrum where SO_2 presents deeper absorption features, and results in an increase in the resulting optical depth. This phenomenon translates to an increased sensitivity of the instrument towards the edges of the image, where a given path concentration of SO_2 will produce a higher differential optical depth (DOD) than in the center, and is characteristic of the particular configuration of lens and filter. I use the gas cell images in conjunction with the clear sky images to describe the response of the system to changing concentrations of SO_2. Placing gas cells of uniform concentrations across the entire field of view allows us to derive a calibration curve at the center of the image, as well as to characterize how the slope of this curve changes across the image, for each pixel on the CCD.

In order to calculate optical depths, I generate an approximation of the clear sky behind the scene, using a fitted second order polynomial. The intensity of the clear sky in the scene is determined by the relative position of the sun at the time of measurement, and by the pattern of reduced brightness introduced by each of the filters. For each image, a series of masks are created in order to isolate the clear sky pixels. They are shown in
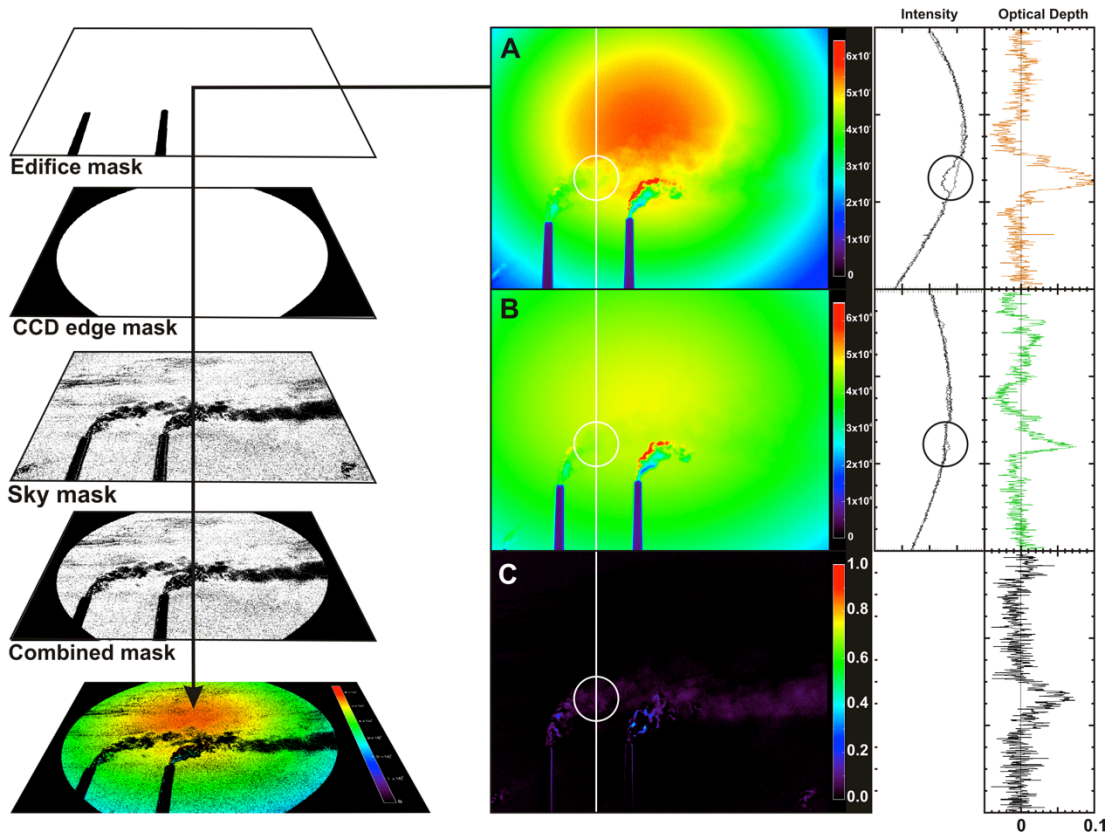
Figure 2.6: Illustration of the fitting technique for the clear sky. A combination of masks is used to isolate the pixels making up the clear sky: 1) an intensity mask on the B image to identify the features of the local relief; and 2) a clear sky mask based on a threshold on the approximation of the transmittance image, to reject the area occupied by the plume. A) The original intensity image in the 310nm filter. The profile on the right shows the extracted cross-section at pixel column 240, and the fitted clear sky function at the corresponding location, as well as the calculated optical depth for the 310nm filter. B) Same illustration for 330nm filter. C) The resulting differential optical depth image.

Figure 2.6. The first two masks are common to all images in a sequence: 1) an edifice mask that identifies the local relief in the scene (volcanic edifice or in my case, smoke stacks), rejecting all pixels below a predefined threshold value in image B; and 2) a CCD edge mask that excludes the areas at the edges of the image, where the sensitivity of the instrument may be lowered. The threshold on the edifice mask is adjusted until all objects in the foreground are included, and if need be, an outline can be drawn manually. The third mask (sky mask) is specific to each individual image. A polynomial is fitted to the pixels not included in the edifice mask, which at this point also include the SO_2 plume. A transmittance image is then calculated by taking the ratio between the original image and the polynomial approximation. Pixels with a value outside of a window around 1 (0.97-1.03) are rejected in order to keep only the pixels constituting the clear sky, and to exclude the plume. Once the plume has been excluded, a polynomial is fitted through the remaining pixels and extrapolated to the entire image to generate a second transmittance image. The process is repeated until all pixels defined as clear sky essentially have a transmittance value of 1, and the last polynomial function is taken to represent the clear sky behind the scene. This technique allows us to account for gradual changes in overall intensity throughout the course of a sequence due to changes in the relative position of the sun.

Optical depth (DOD or τ in the following equation) images are calculated for each set of images using the Beer-Lambert-Bouger law of absorption:

$$\tau_A = - \ln (I_A / I_{skyA}) \tag{2.1A}$$

$$\tau_B = - \ln (I_B / I_{skyB}) \tag{2.1B}$$

where I is the intensity of each pixel in the image, and I_{sky} is the intensity of the corresponding pixels in the polynomial approximation of the clear sky. Differential Optical Depth (τ') images are calculated as follows:

$$\tau' = \tau_A - \tau_B \tag{2.2}$$

where the indices indicate the images from camera A (with a filter at 310 nm), and camera B (with a filter at 330 nm).

2.2.4 *Image Calibration*

The Beer-Lambert-Bouger law of absorption implies that the reduction of light intensity is proportional to the concentration of the gas along the light path, such that the optical depth scales linearly with the path concentration. I have implemented two options to calibrate the data and convert DOD values to path concentrations (Figure 2.7); the first uses gas cells of known concentrations, while the second uses a cross-correlation between time-series from the images and the USB2000+ spectrometer data. During the calibration

stage, at the beginning or end of each data sequence, two gas cells of known concentrations (25mm in diameter, 350 and 1150 ppm•m path concentrations, respectively) are placed directly in front of each lens, so that the cell fills the field of view of the lens. I produce DOD images for each calibration cell using equations (2.1A), (2.1B) and (2.2). In order to account for the absorption created by the cell walls, I remove a constant value τ'_w such that:

$$\frac{\sigma_1 \cdot \tau'_1 + \tau'_W}{\sigma_1} = \frac{\sigma_2 \cdot \tau'_2 + \tau'_W}{\sigma_2} \qquad (2.3)$$

where σ_1 and σ_2 are the path concentration of the two gas cells, and τ'_1 and τ'_2 are the average values of DOD obtained from the images. A linear calibration curve is computed for each pixel in the image, in order to quantify the change in sensitivity produced by the shift in wavelength with incidence angle.

The data from the spectrometer are analyzed using a Differential Optical Absorption Spectroscopy (DOAS) method, as described in Platt and Stutz (2008). High-resolution spectra were collected at the same frequency as the imagery and data acquisition was synchronized on all three instruments. For each pair of images, 5 consecutive spectra were collected and co-added, each with an integration time of 100-150 ms (depending on the time of day). The spectra are processed using an iterative forward model, which reproduces the measured spectrum using an SO_2 absorption cross-section (Vandaele et al., 1994) and the background spectrum acquired during calibration.

26

SO$_2$ slant column amount (molec cm^{-2}) are evaluated over the spectral range 307-320 nm, and are subsequently converted to path concentrations (ppm•m) assuming standard temperature and pressure. The resulting time series is used to produce a second calibration curve by correlating the measured concentrations from the USB2000+ with the matching optical depths measured by the camera. The field of view of the 84-UV telescope is approximately 1º, which given the field of view of the camera lenses, corresponds to a spot size of about 4x4 pixels. The relative location of the field of view of the telescope in the images is determined by correlating the time series of path concentrations measured with the USB2000+ spectrometer with the time series of values from each group of pixels in the DOD image. The resulting image is an array of correlation factors (R^2) quantifying the similarity between the two time series. A calibration curve is then created using a linear regression of the data from the DOAS retrieval and the time series of DODs from the group of pixels with the highest correlation factor. Each separate measurement sequence requires a new calibration because the main acquisition parameters (exposure time on the cameras and integration time on the spectrometer) are altered for each period. Depending on the location of the overlapping fields of view, the slope of the resulting calibration line needs to be adjusted across the image, using the CCD response image calculated from the gas cells.

The results of the calibration are presented in Figure 2.7 for two data sets collected on October 23rd, 2013. The slope of the calibration line produced by the gas cells varies among the data sequences by approximately 10%. This variation is expected

27
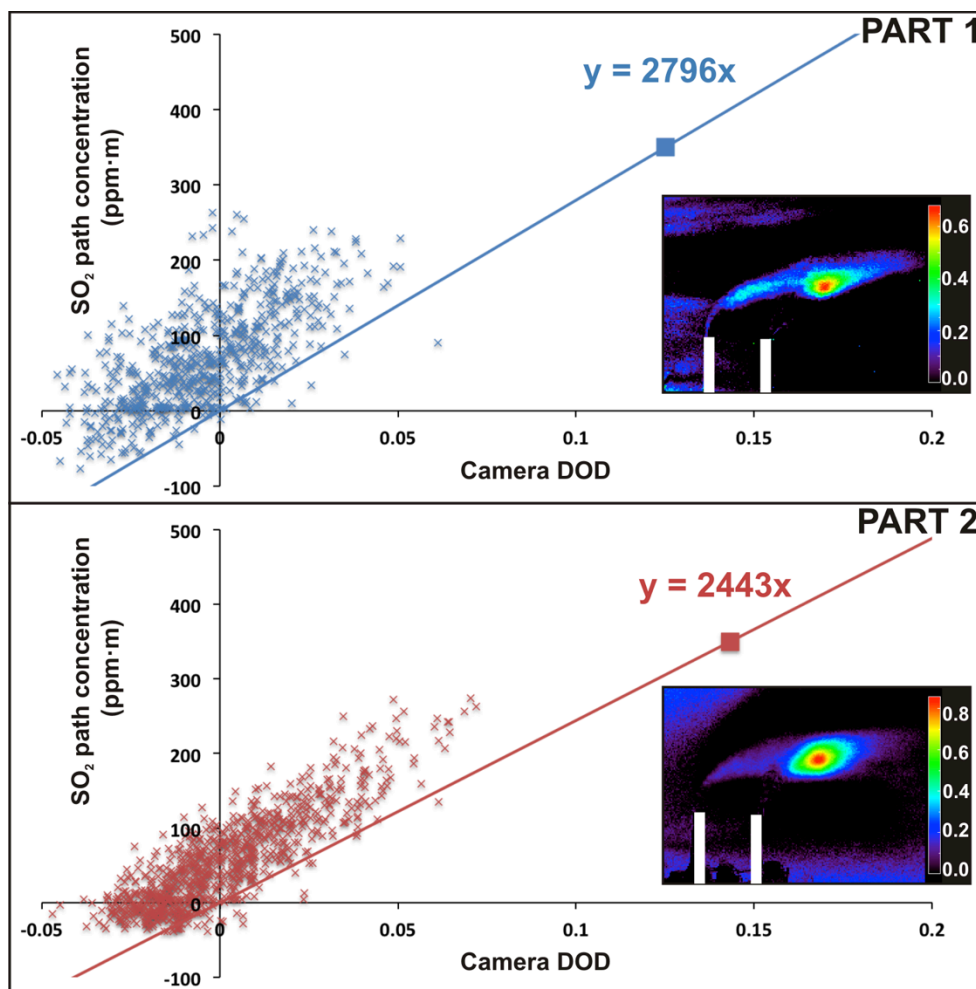
Figure 2.7: Calibration data for both parts of the data set on October 23rd, 2014. The lines are the linear fits produced with the measured DOD of two gas cells of known concentrations that have been placed directly in front of the camera lenses during calibration (only the 350 ppm•m cell is shown on this plot, the second one is at ~1150 ppm•m). The insets show the value of the correlation factor (R^2) between the time series of SO$_2$ path concentration from the USB2000+ data and the time series of differential optical depth (DOD) calculated for each pixel in the data set. The values extracted at the location of the highest correlation factor are plotted next to the calibration curve.

due to changes in the relative amounts of light passing through each of the filters with changing solar zenith angle (SZA). As the day progresses, not only must the acquisition parameters be adjusted to accommodate the change in overall intensity at all wavelengths, but so must a new calibration curve be produced. To fully understand the impact of changing SZA, I have conducted a short experiment and produced calibration lines using the gas cells over the course of a clear day, keeping the camera at a constant azimuth. The results of this experiment indicate that the slope of the resulting line can deviate from a value computed at solar noon by up to 30% for SZAs lower than 60 degrees. The calibration plots derived from the USB2000+ data show significant scatter, and the linear regressions generated using those data have low R^2 values, and therefore should not be extrapolated to the entire image set. The overall gradients, however, are consistent with the curves produced by the gas cells, albeit with offsets from zero (which may be due to different Mie scattering effects between the two filters). Because of the scatter and low R^2 values for the USB2000+ calibration in this particular campaign, I have chosen to use the calibration line produced by the gas cells to calibrate my data. I discuss the cause for low R^2 values later in this document. The resulting path concentration maps (example in Fig. 2.8) are the basis for the retrieval of the emission rates.

29
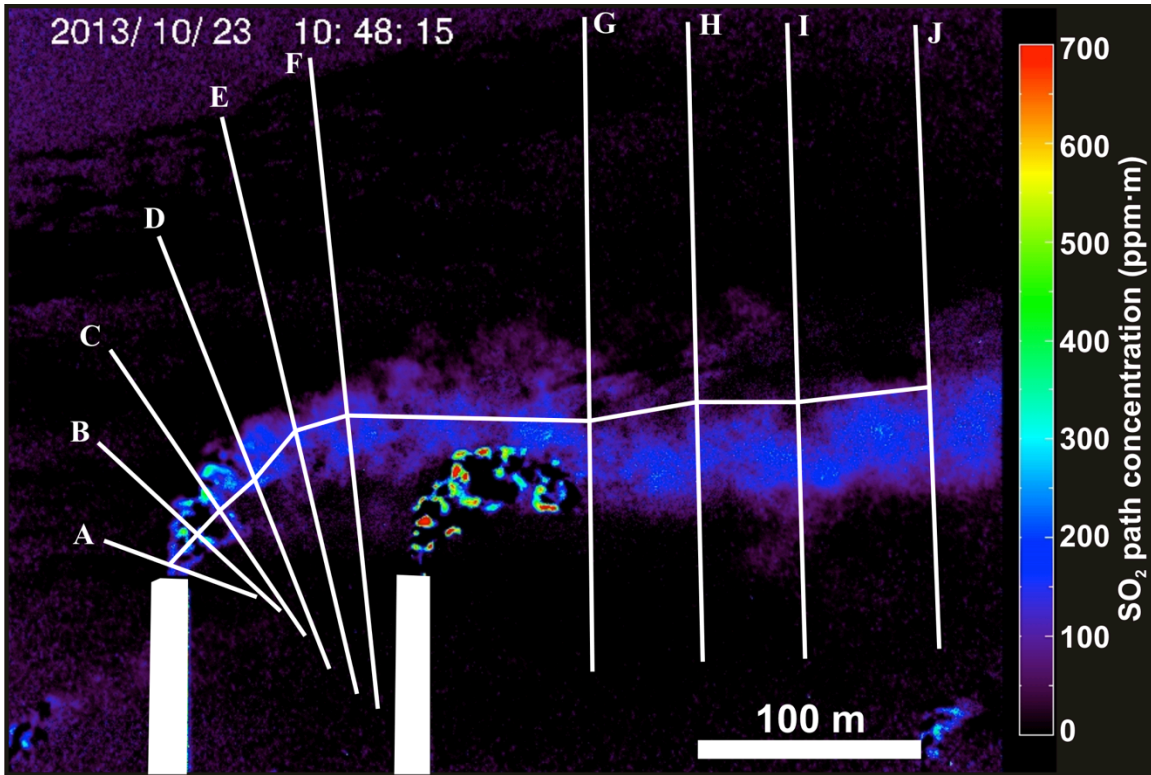
Figure 2.8: Example of an SO_2 path concentration map. Cross-sections are drawn across the drifting plume to calculate emission rates (see Fig. 2.12).
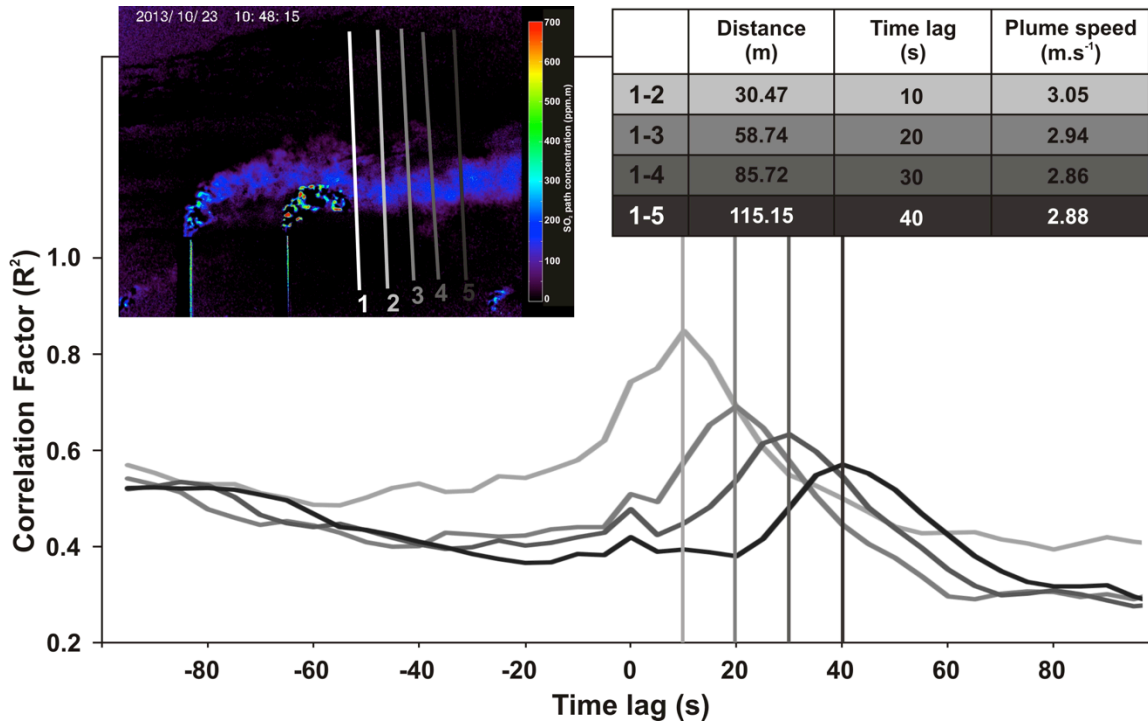
Figure 2.9: Determination of the plume speed. The figure shows an example of a cross-correlation between five time series of integrated masses taken at the locations labeled 1-5 in the image insert. The best fit for each pair of cross-sections indicates the time it takes for specific features to travel from one cross-section to the other. Cross-sections are drawn downwind to the west of unit 3. The technique is applied to various subsets of the data set. Plume velocity over the measurement period remained constant and average velocity derived with this method is 3.0 ± 0.8 (1σ) m s^{-1}.

2.2.5 Calculation of Emission Rates

Emission rates are calculated by defining a cross-section perpendicular to the direction of the drifting plume. Path concentrations are integrated along that cross-section, and multiplied by the plume velocity. Figure 2.8 shows an example of a path concentration image and the locations of several cross-sections over which the path concentrations were integrated. Following Mori and Burton (2006), I use a cross-correlation method to calculate the plume velocity. Each cross-section in Figure 2.9 produces a time series of integrated mass (kg m^{-1}). The time series are then cross- correlated to obtain the number of images required for a given peak to move from one cross-section to the next (image lag). This image lag is converted into a time lag and the plume speed is calculated by dividing the distance between the cross-sections, as measured along the plume axis, by the time lag yielding the best correlation factor. Figure 8 shows an example of the cross-correlation results. The overall plume speed is calculated using the average of the measured plume velocities.

2.3. Results

I present the results of two consecutive data sequences acquired on October 23rd, 2013, at the Cholla plant. The plant emits SO_2 from four main stacks, two of which were captured in the field of view of my instruments: units 2 and 3. A smaller plume from a third stack occasionally drifts in the field of view in some of the images, but it never

overlaps with the plumes that are the subject of these results. At a height of > 120 m, the stacks tower above the plant facility and the overall landscape, offering unrestricted views of the drifting plume. Acquisition was started around 10am (local time) and I acquired two sequences of 1 and 1.5h, respectively, imaging at a frequency of 0.2 Hz. The gap between the two acquisition sequences is a calibration period, where clear sky, dark, and gas cell images and spectra were taken, pointing at a clear portion of the sky approximately 30° to the East of the target area. During this gap, data acquisition had to be halted to accommodate the overall lighting changes through the course of a day, which required adjustment of the acquisition parameters on the system in order to keep the signal within an acceptable range. Once calibration data was obtained, I redirected the instrument toward the power plant. I then ran a real time DOAS retrieval algorithm on the USB2000+ data alone, in order to find an optimal position for the telescope such that the observed gas amounts span a range of values (actual pointing positions are shown in the correlation maps of Figure 2.7).

Figure 2.10 shows the time series of emission rates for both stacks: unit 2, located on the left (East) in Figure 2.8, and unit 3, located on the right (West) in the same image. I used the cross-correlation method above to estimate the plume velocity to be 3 m s^{-1}, which remained nearly constant through both measurement periods. Emission rates for unit 2 were calculated by integrating path concentrations over the cross-section labeled D in Figure 2.8. Because the plumes from unit 2 and unit 3 stacks merge very near the unit 3 vent, emission rates for unit 3 were calculated by subtracting the emission rates
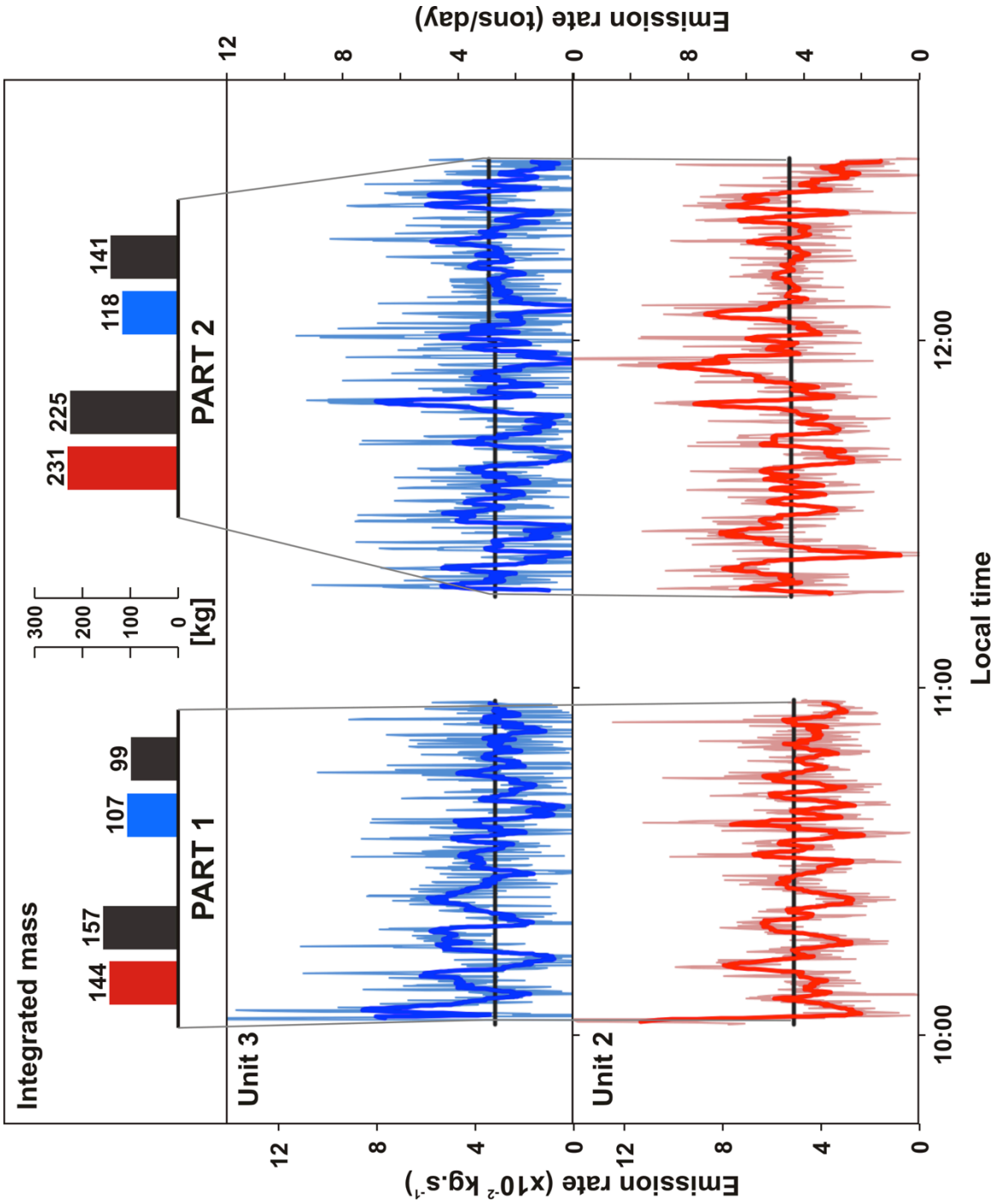
Figure 2.10 (previous page): Time series of SO_2 emission rates from the Cholla power plant on October 23rd, 2013. Light shades are the original 0.2Hz data. Darker lines are smoothed using a 1-minute moving average filter. Emission rates for unit 2 are derived from the cross-section labeled D in Fig. 6. Emission rates for unit 3 are calculated by subtracting the emission rate measured at cross-section F from the one measured at cross-section G, offsetting the time series for travel time between the two cross-sections. Black lines are average emission rates calculated from the emissions reported by the EPA. Bar charts on top are the cumulative emissions calculated by integrating the time series of emission rates over each measurement period for unit 2 (in blue) and unit 3 (in red). This allows a direct comparison with the hourly emissions reported by the EPA (in black).

obtained using cross-section F from those calculated using cross-section G. The time series at F was offset to account for the travel time between the two cross-sections, and corrected to account for the apparent dilution/depletion that occurs during travel (see discussion below). The distance between F and G is approximately 140 m, which corresponds to a travel time of 45 s (9 frames at 0.2 Hz). The emission rates measured by the SO_2 camera fluctuate greatly around the reported hourly values, with considerable variability on very short time scales (10s of seconds and lower). These first-order fluctuations are due to the highly turbulent behavior of the plume and are not indicative of changes in the source output. I have produced a minute-averaged time series with a moving window of 12 frames in order to remove this effect and emphasize the second-order fluctuations, which I believe to represent variations at the source. My measurements for unit 2 average 4.7 ± 1.3 x10^{-2} kg s^{-1} for the first sequence, and 5.5 ± 1.5 x10^{-2} kg s^{-1} for the second sequence. Average emission rates extracted for unit 3 are 2.8 ± 1.5 x10^{-2} kg s^{-1} for the first sequence, and 3.5 ± 1.4 x10^{-2} kg s^{-1} for the second sequence. The EPA reports (http://ampd.epa.gov/ampd/), the emitted mass of SO_2 every hour for each of the smoke stacks which I converted to average emission rates, assuming a constant release rate over the course of an hour. Those averages values for unit 2 are 5.1x10^{-2} kg s^{-1} over the first sequence and 5.3x10^{-2} kg s^{-1} over the second sequence. Unit 3 is reported at 3.3x10^{-2} kg s^{-1} for both sequences. In order to compare the hourly values more directly, I have integrated the emission rates over the duration of each data sequence, and compare the cumulative masses directly to the emissions reported by the EPA. The results are presented as bar plots in the upper part of Figure 2.10.

36

2.4 Discussion

My measurements are in good agreement with the numbers reported by the EPA, all four values falling within 20% of the reported values or better. The measured emission rates vary significantly from frame to frame, with changes of up to an order of magnitude. I interpret the high frequency variations to be the result of turbulent structures in the drifting plume, which cause spatial variations in SO_2 concentration. Individual structures are roughly a tenth to a quarter the size of the plume itself (10-50 m in diameter) and move through individual cross sections quickly, producing the observed variations. The time series smoothed with a moving average of 12 frames (1 minute) shows second-order variations with a frequency of 2-5 minutes, likely representing changes in the source output.

Linear regressions through the USB2000+ data (Fig. 6) yield very low R^2 values (typically < 0.5). Better regressions can be obtained when the range of observed concentrations is larger, but the values measured in the plume from Cholla only cover a very small range of optical depths (< 0.1). The amount of scatter in those calibration data is an indication that the instrument was operating close to the detection limit of the SO_2 camera. Indeed, the standard deviation of a cross-section taken through a region of clear sky is 0.015 in DOD, corresponding to ~30 ppm•m, which can be taken to represent the noise associated with this method. The peak DODs in the cross-sections through the plumes rise to only 2-5 times that value, depending on the location of the profile. In those

37

conditions, dilution of the plume signal into this ambient noise can become a problem, and any process that contributes to gas dilution, such as turbulence, may result in an apparent reduction in gas flux.

I found the measured emission rate to be dependent on the location of the cross-section used for the calculations. Figure 2.11 presents a series of 10 cross-sections averaged pixel by pixel over the first data sequence (50 minutes: 607 frames), at increasing distances from the source along the drifting plume. A curve made of one or more Gaussian distributions is fitted to each cross-section. Emission rates are calculated by integrating over the averaged cross-sections, and over the Gaussian curve, subtracting a baseline value to account for the possibility of non-zero background. Cross-sections A through F are drawn across the unit 2 plume at tightly spaced intervals (20-30 m apart). Cross-sections G through J are drawn across the combined plumes from units 2 and 3, and at more broadly spaced intervals (100-150 m). The emission rates derived from these averaged cross-sections increase with increasing distance from the source from cross-section A to D, and then decrease with distance from source along the drift axis (G through J). As expected, the distributions widen and the peak path concentration decreases with distance from the source, reflecting the expansion of the plume due to turbulent entrainment of air, and the subsequent dilution of SO_2.

Interestingly, starting with cross-section A, I also observe an increase in the average emission rate with increasing distance from the source, until the values stabilize

38

(D-F). Bluth et al. (2007) had already observed this effect in their original work. One might think that measurements should be made at section A in order to capture the source emissions as accurately as possible, however, this study shows that emission rates measured at section A represent an underestimation of the actual emission rate. One possible explanation for this phenomenon is the presence of aerosols and/or water droplets in the plume very near the source. Cross-sections A-C were drawn in a part of the plume where condensation was high based on visual observations. Optically thick plumes can be challenging because a majority of the photons coming from behind the plume are scattered away before they can cross the plume, and only photons that are scattered towards the instrument from the outer part of the plume reach the sensor. In these conditions, light dilution is an important factor, and can lead to severe underestimation of the path concentrations. Kern et al. (2013) demonstrated this effect using a radiative transfer model and simulating an optically thick plume at Kilauea volcano. Though the effect is most significant for high concentrations (> 1000 ppm•m), it is not null at lower concentrations, as suggested by the low emission rates measured using cross-sections A through C. Although not present in any of the averaged cross-sections, cross-sections in individual frames at locations A through C sometimes show negative values of DOD at the edges of the plume. This may be the result of reflections off of water droplets.

Cross-sections D through F are drawn outside of the condensing part of the plume and the emission rates derived from them are higher than those derived from cross-

sections A through C and closer to the EPA reported values. Cross-sections G through J are drawn to the West of unit 3. At that point the plumes from both unit join and I should be measuring the combined emissions of both units. The first cross-section (G) is drawn outside of the condensing region in the plume from unit 3, and sections H through J are spanning the distance to the edge of the image. I observe a decrease in apparent emission rate with increasing distance. I consider two explanations for this phenomenon. The first is SO_2 loss through oxidation reactions with the atmosphere. This effect has been documented at industrial sites (e.g., Eatough et al., 1994) as well as for volcanic centers (e.g., Rodriguez et al., 2008), and has been found to lead to significant underestimation of SO_2 emission rate at distances greater than 2 km from the vent. However, the distances in this case are much lower and the distance from section G to section J is <500 m, leaving little time for significant oxidation. Furthermore, the atmosphere at my location is extremely dry, which should decrease the potential for oxidation as well. Even the highest depletion rate of 10^{-3} m^{-1} reported by Rodriguez et al. (2008) would only account for a reduction of 5% in the measured emission rate between sections G and J. I observe a reduction of up to 50% over the same distance. A second explanation comes from simple plume dilution caused by turbulent entrainment of air. Because I am dealing with extremely low concentrations, mixing of the plume with the surrounding atmosphere will dilute SO_2 and reduce path concentrations at any given pixel, possibly to the point where it falls below the detection limit of the instrument (~30 ppm•m in this case). The concentration at the edges of the plume then may blend into the surrounding background and thus the measured emission rate is reduced. The same process causes the plume to

expand with distance from source possibly causing it to extend beyond the field of view of the instrument. A combination of these effects will result in underestimation of the SO_2 emission rate.

The variations in the measured emission rate along the drifting axis of the plume illustrate the importance of selecting an optimal location for the cross-section. Cross-sections too close to the vent are affected by reflection and light dilution effects, while cross-sections too far from the vent are affected by the dilution of the plume edges into the background noise. The ability to draw multiple cross-sections allows us to recognize these effects and to choose the appropriate location. While the distribution of concentrations in the plume is expected to vary significantly during transport, the mass of SO_2 passing through each cross-section should remain constant, and the average emission rate calculated from each cross-section should be the same. No physical or chemical process can account for the addition of SO_2 in the plume. Therefore it is fair to assume that the emission rates measured at cross-sections A through C are underestimates of the true emission rate. The physical dilution of the plume starts at the vent, but it will only lead to an underestimation of the emission rate if the concentrations fall below the detection limit of the instrument. That effect is clearly seen in cross-sections G through J. However, cross-sections D through E all produce very similar emission rates, leading us to believe that dilution at the plume edges does not play a significant role at that distance. The fact that my measurements at those locations are corroborated by the values from the EPA represents further validation of my selection.
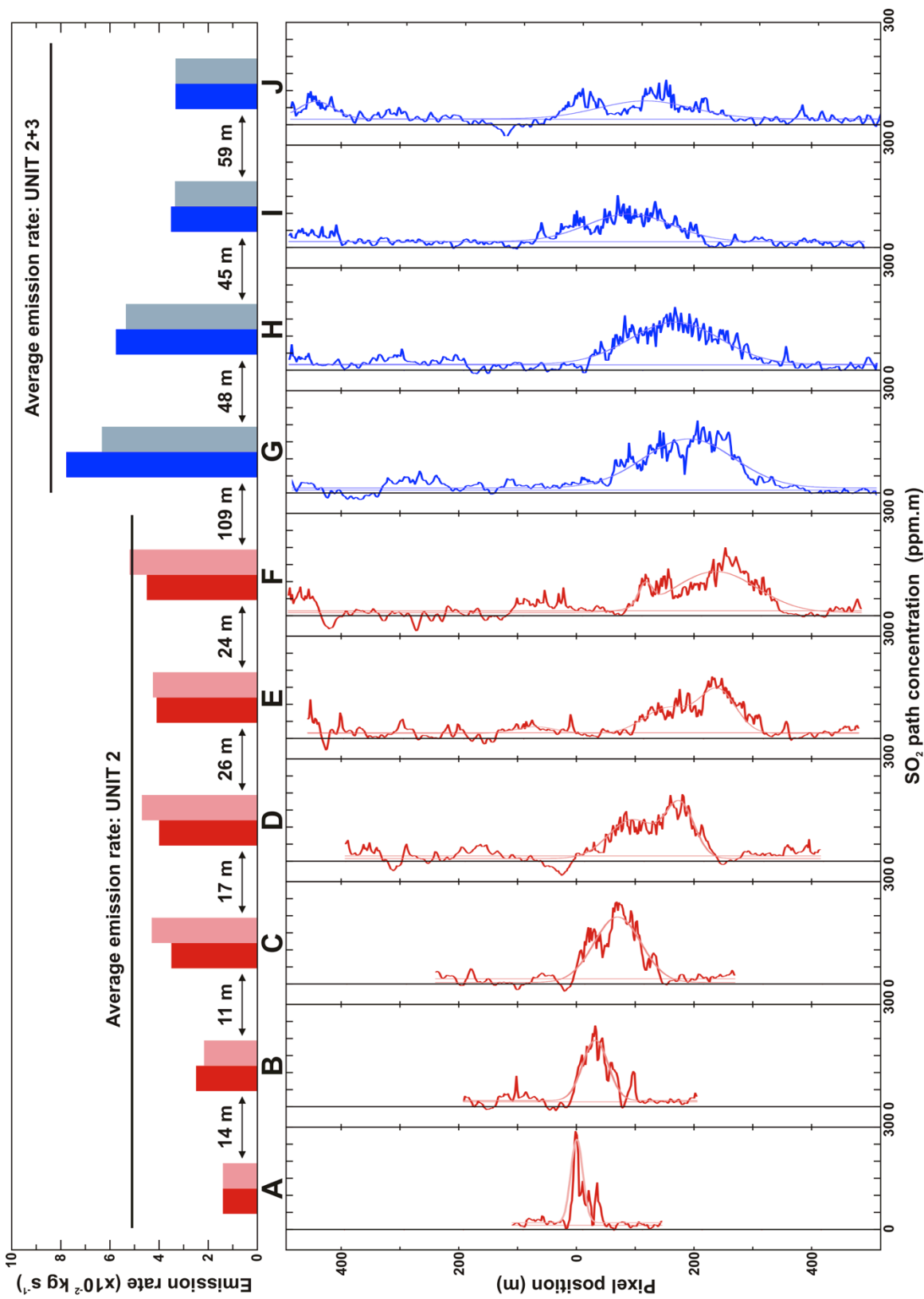
Figure 2.11 (previous page): [bottom] Cross-sections averaged over a subset of the measurement period between 10-11am on October 23rd, 2013 (PART 1: n=607). Red cross-sections are drawn on the plume emitted by unit 2 only, blue cross-sections are drawn on the combined plumes from unit 2 and unit 3. Gaussian distributions fitted to the cross-sections are shown in lighter shades. [top] Average emission rates, calculated from the plotted cross-sections, using a calculated plume speed of 3 m.s^{-1}, for both the average cross-sections (dark shades) and fitted Gaussian distributions (light shades). The distance between each cross-section along the plume axis is indicated for reference. The average emission rates computed from the values reported by the EPA are shown as black lines.

The aforementioned effects are likely to occur in many environments and for any geometry with a point-source emitter of SO_2, be it an industrial facility or a volcanic center. I therefore suggest that the optimal method for determining realistic emission rates using an SO_2 camera is to define a series of cross-sections along the plume axis, average the extracted path concentration profiles over a period of time, and calculate the average emission rate for each section. Since all three potential effects (i.e., light dilution from an optically thick plume, physical dilution of the plume leading to blurring of the edges, and oxidation of SO_2 during transport) result in underestimation of the measured concentrations, it stands to reason that the cross-section that yields the highest emission rate is the closest approximation to the actual emission rate at the source. Special care should be taken when considering the appropriate plume velocity for each cross-section, as it may vary along the plume axis, especially when considering the transition from a buoyant plume to a plume drifting with the local wind.

2.5 Conclusions and Outlook

The SO_2 camera proved to be a suitable tool for the measurement of passive emissions of SO_2, even at very low concentrations (<50 ppm•m) and fluxes (0.02 kg s^{-1} and below), with a measurement accuracy of approximately 20% demonstrated in this study. The instrument was designed with volcanic emissions in mind, which are usually considerably larger than the emissions observed at the Cholla power plant. Passive volcanogenic emissions typically range between 2-3 kg s^{-1} for the lowest emitters (e.g.,

Stromboli, Burton et al., 2009) to over 100 kg s^{-1} (e.g., Hawaii, Kern et al., 2013). Such emissions produce concentrations well above the detection limit I observe in this study, providing a higher signal-to-noise ratio and likely increasing the accuracy of the retrievals. In order to accurately measure the emission rates at the Cholla plant, it was crucial to find the ideal location for the cross-section, to avoid underestimation caused by either an optically thick plume in the condensing region near the vent, or an apparent loss of signal due to plume diffusion further away from the source. Most volcanic plumes will have higher concentrations than the ones observed at Cholla, making the potential effects of aerosol conversion more significant. I also expect plume diffusion to remain an important factor at volcanic centers. I was also able to isolate the SO_2 emissions of each smoke stack, another exercise that would prove much more logistically challenging with conventional scanning spectroscopic methods. The SO_2 camera provides contextual information to help not only locate the optimal location for the retrievals, but also investigate physicochemical processes occurring in the plume. Validation of the instrument should continue at power plants with higher emissions and at various locations in order to fully characterize the response of the instrument in different emission, lighting, and weather conditions.

CHAPTER 3

SO$_2$ EMISSIONS AT SEMERU VOLCANO, INDONESIA

The results from this chapter have been published in a peer-reviewed journal and can be found under the reference below. My co-authors have given me permission to reproduce the work in my dissertation.

SMEKENS, J-F., CLARKE, A. B., BURTON, M. R., HARIJOKO, A. and WIBOWO, H. W. (2015): SO$_2$ emissions at Semeru volcano, Indonesia: characterization and quantification of persistent and periodic explosive activity. *J. Volcanol. Geotherm. Res.* doi:http://dx.doi.org/10.1016/j.jvolgeores.2015.01.006.

I present the first measurements of SO$_2$ emissions at Semeru volcano, Indonesia, using an SO$_2$ camera. Activity at Semeru is characterized by quiescent degassing interspersed with short-lived explosive events with low ash burden. The interval between explosions was measured at 32.1±15.7 minutes in a webcam survey of the volcano between the months of June and December 2013. I distinguish between two types of events: shorter events (type I: ~5 mins duration) with emissions returning quickly to baseline levels, and longer events (type II: ~15 mins duration) often showing multiple pulses and a longer period of increased emissions before a return to quiescent levels. Type I events represent > 90 % of the activity and release an average of 200-500 kg of SO$_2$ per event. The single type II event I documented with the SO$_2$ camera released a total of 1460 kg of SO$_2$. I estimate the daily average emissions of Semeru to be 21-71 t d$^-$

[1] of SO$_2$, amounting to a yearly output of 8-26 Gg (8,000 – 26,000 metric tons), with 35-65% released during explosive events. The time series patterns of degassing are consistent with the existence of a viscous plug at the top of the conduit, which seals the conduit immediately prior to explosive events, causing pressurization of the underlying magma followed by a sudden release of gas and fragmented magma.

3.1 Introduction

Part of the Semeru-Tengger massif, Semeru volcano (8.108° S, 112.92° E) is a stratovolcano that sits on the southern edge of a complex comprising the 3 nested calderas of Bromo-Tengger (Figure 3.1), Jambangan and Ajek-Ajek. The steep-sided Mahameru cone rises 3,676m above sea level. Holocene eruptive products are mostly medium-K andesites (Carn and Pyle, 2001; Fischer et al., 1994; Sutawidjaja et al., 1996). The active crater, Jonggring-Seloko (~400m wide and 200m deep) opens to the southeast and hosts an active lava dome (Fig 2). Activity at Semeru has been dominated by frequent small explosions since the start of the current eruptive phase in 1967, with ash clouds rising from a few hundreds to a few thousands of meters, and with a frequency of minutes to hours. Explosive activity is often accompanied by lava dome growth and collapse, with sporadic larger Vulcanian events and frequent lahars (Thouret et al., 2007). The active dome started to grow in the crater in August 2009, after a 5-month repose period.
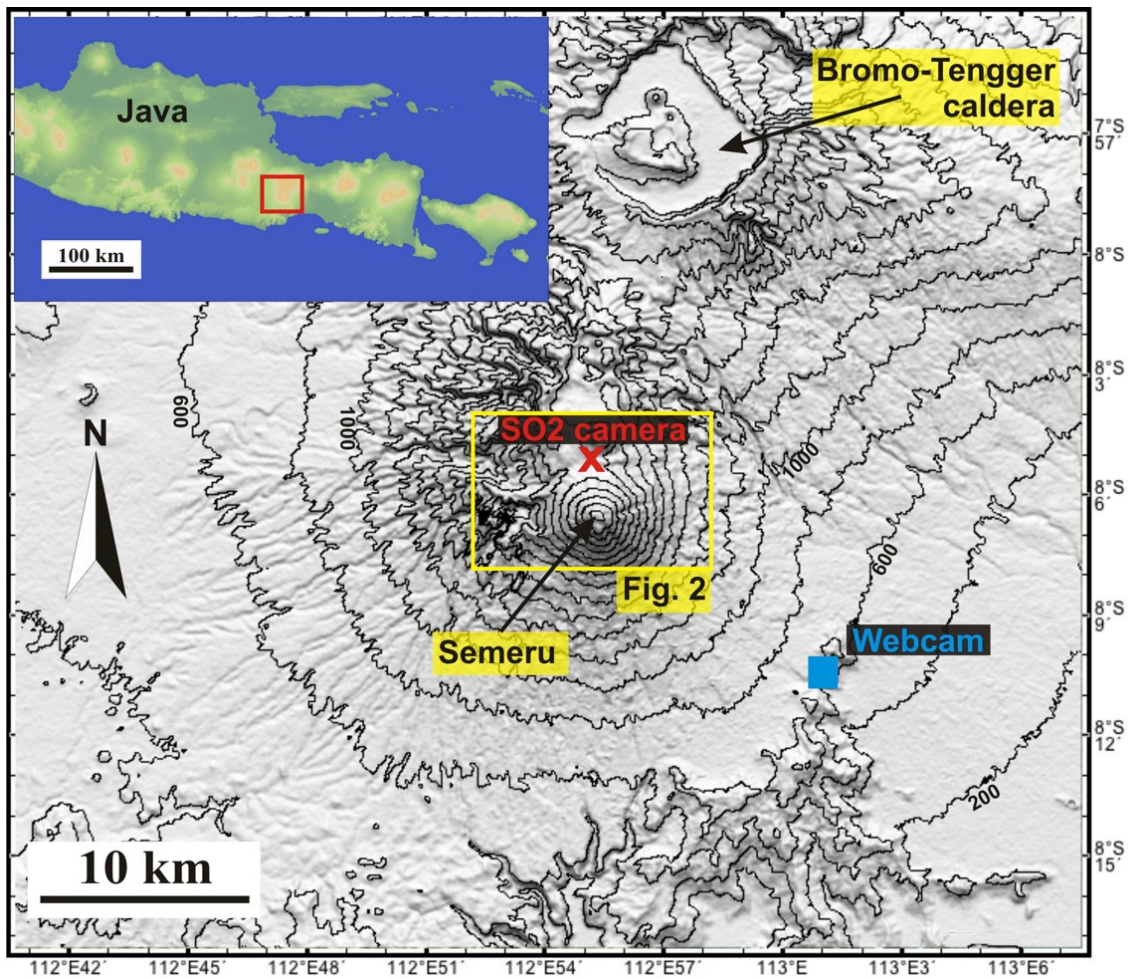
Figure 3.1: General context map. Contour interval on the base map is 200m. Blue square marks the location of the webcam at the Gunung Sawur Volcano Observatory (GSVO), ~11 km to the southeast of the active crater. Yellow rectangle outlines the area detailed in Figure 3.2. Red X marks the location of the SO$_2$ camera during data acquisition, at the Kalimati plain.

N

A

Kalimati

3000

Mahameru
3676m
x

Optimal wind direction

1km

Active
crater

A'

9am
43.2°

8am
31.2°

7am
18.2°

Sun position

2000

Optimal wind direction

A

A'

3180m

Elevation (m)

3500

Kalimati

Active
crater

2500

0   2   4   6

Distance (km)
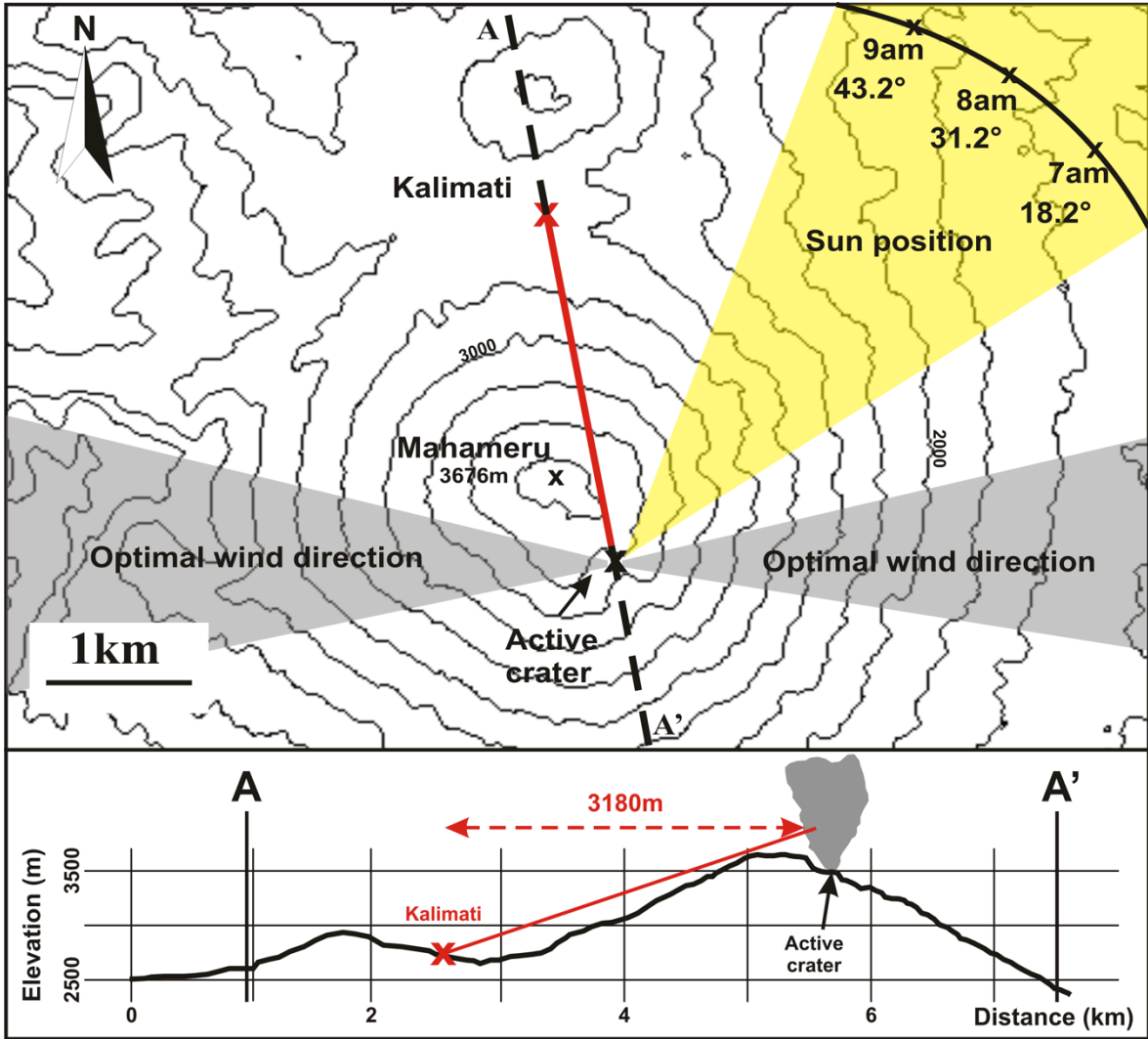
Figure 3.2 (previous page): The map shows the area within the yellow box in Figure 1. Lower panel illustrates the viewing geometry for the SO_2 camera campaign. Contour interval on the base map is 200m. The red X marks the location of the SO_2 camera during data acquisition. The red line represents the line of sight. Declination was ~21°. All data were acquired between 6 and 10am local time. The grey cones represent the variation in wind direction during data acquisition. All data was acquired when plumes were drifting East, West or rising vertically in the absence of wind. These optimal wind directions also represent the most common wind direction in the region at that time of year. The yellow cone represents the approximate sun azimuth for the period of data acquisition (May 16 – June 3, 2013), as well as the sun elevation.

Semeru is one of many volcanic centers whose activity can be described as persistently active explosive activity. Other examples include Stromboli (Italy), Karymsky (Russia), Santiaguito (Guatemala) Arenal (Costa Rica), Yasur (Vanuatu), and Sakurajima (Japan). This type of volcano represents an optimal target for studying mechanisms associated with explosive eruptions, and the transitions between effusive and explosive activity. Often qualified as "open-system", the degassing patterns during such activity are key to understanding the driving mechanisms for the explosions. Several studies have provided temporary monitoring of the deformation around the active crater at Semeru using tilt-meters and the existing network of broadband seismometers (e.g. Iguchi et al., 2008; Nishi et al., 2007; Nishimura et al., 2012). There is however no permanent or temporary monitoring of the volcanic gas emissions. This study reports the first measurements of sulfur dioxide (SO_2) emission rates at Semeru. I acquired data using an SO_2 camera to measure fluctuations in the gas emissions at high frequency (1 measurement every 5 s), and I extracted images from an automated webcam located at the Gunung Sawur Volcano Observatory (GSVO) to estimate the frequency of eruption. The location of both instruments is reflected in the general context map in Figure 3.1. The specific viewing geometry during the field campaign is described in Figure 3.2.

3.2 Methods

The SO_2 camera constitutes a relatively recent development in UV spectroscopic methods for gas monitoring (Bluth et al., 2007; Mori and Burton, 2006). The instrument

and methods used in this study are described in detail in Smekens et al. (2014). The system consists of 2 Quantum Scientific Imaging (QSI) 620s high sensitivity cameras, with a 1600x1200 Kodak KAI-2020 charge-coupled device (CCD) and a special UV coating, and an Ocean Optics USB2000+ spectrometer. Each camera is equipped with a UV2528B quartz lens, from Universe Optics with an effective full angle field of view of ~30°. One camera is fitted with a UV bandpass filter centered at 310 nm, the other is fitted with a bandpass filter centered at 330 nm. Both filters have a ~10 nm full width at half maximum. The 310nm filter (A) is designed to capture the absorption features produced by the SO_2 molecules. However filter A is also sensitive to broadband absorptions due to the presence of aerosols or particulate matter. The role of the second filter (B: 330nm) is to capture only these broadband absorptions, to produce an image that can be used as a reference to isolate the signal produced by the SO_2. To carry light to the spectrometer, I use an Ocean Optics 84-UV collimating lens with a focal length of ~100 mm to focus light onto a 40 μm fiber optic cable. This USB2000+ spectrometer is fitted with a #7 grating diffracting light between 280-420 nm onto a 2048 linear CCD, and offers a spectral resolution of ~0.5 nm.

Differential Optical Depth (τ') images are produced by subtracting the optical depth measured in the 330 nm filter (B) from that measured in the 310 nm filter (A):

$$\tau' = - ln \left(I_A / I_{skyA} \right) + ln \left(I_B / I_{skyB} \right) \tag{1}$$

where I is the intensity of each pixel in the image, and I_{sky} is the intensity of the corresponding pixels in the clear sky image. The indices indicate the images from camera A (with a filter at 310 nm), and camera B (with a filter at 330 nm). These DOD images are then calibrated to path concentration amounts of SO_2 (ppm·m) using either a set of gas cells of known concentrations, or the data collected with the UV spectrometer. Gas cells are placed directly in front of each of the cameras and imaged against a clear background during the gaps in data acquisition. The spectrometer, on the other hand, is pointed directly at the drifting plume during data acquisition, and provides a point of reference in the image. The data from the spectrometer are analyzed using a Differential Optical Absorption Spectroscopy (DOAS) method, as described in Platt and Stutz (2008), to produce a time series of path concentrations within the field of view of the telescope. The relative location of the field of view of the telescope in the images is determined by correlating the time series of column amounts measured with the USB2000+ spectrometer with the time series of values from each pixel in the DOD image. The resulting image is an array of correlation factors (R^2) quantifying the similarity between the two time series. Both methods (gas cells and USB2000+) produce a set of points relating the measured DOD to a path concentration of SO_2.

Figure 3.3 shows an example of the calibration data, acquired on June 1st, 2013. In general I observed good agreement between the calibration generated from the gas cells and those obtained using the USB2000+ data. I used the spectrometer data to calibrate the images whenever possible. However, some data sets did not lend themselves to the use of

this method because the spectrometer's field of view did not overlap with the drifting plume. This complication was frequent during days of low emissions, when the quiescent plume was practically invisible to the naked eye. In an ideal case, the correlation method to determine the location of the spectrometer's field of view yields a Gaussian distribution of R^2 values, with the highest correlation factors at the peak of the 2-D Gaussian curve. If the dynamic range of path concentrations measured by the spectrometer is low – a clear sign that the field of view of the spectrometer is pointing outside the drifting plume – the correlation results will show low correlation factors across the image. For that reason, I restricted the use of the spectrometer-based calibration to data sets where the maximum R^2 value was greater than 0.85 and located at the center of a 2-D Gaussian distribution (as is the case on the data set represented in Figure 3). For all other cases, I used the calibration cells. The advantage, however, of using the USB2000+ for calibration is that there is no need to pause data collection to re-calibrate the instrument every 20-30 minutes, as is the case when using the gas-cell calibration method.

The slope of the calibration line produced by either method is dependent on the relative amounts of light passing through each of the filters, which in turn depends on the solar zenith angle (SZA). This dependence is especially important at low SZAs, such as the ones observed at low latitudes during the early hours of the day. Figure 3.2 depicts the viewing geometry at the time of my measurements. During periods of relatively clear skies (6-9am), the solar zenith angle changes rapidly from values of 10° to 60°. As the

day progresses, the acquisition parameters must be adjusted to accommodate the change in overall intensity at all wavelengths, and a new calibration curve must be produced. As a result, data acquisition was limited to blocks of 20-30 minutes before a new calibration was performed.

The SO_2 camera allows us to calculate emission rates across a cross-section of my choice, perpendicular to the drifting plume direction. Path concentrations are integrated along that cross-section, and multiplied by the plume velocity. Figure 3.4 shows three examples of the path concentration images produced by the instrument, representing the various types of activity at Semeru, as described in the next section. Plume velocity is determined using a cross-correlation method (Mori and Burton, 2006; Smekens et al., 2014) between the time series of integrated masses calculated at several consecutive cross-sections along the plume axis. The overall plume speed is calculated using the average of the plume velocities measured by cross-correlating multiple possible combinations of cross-sections.
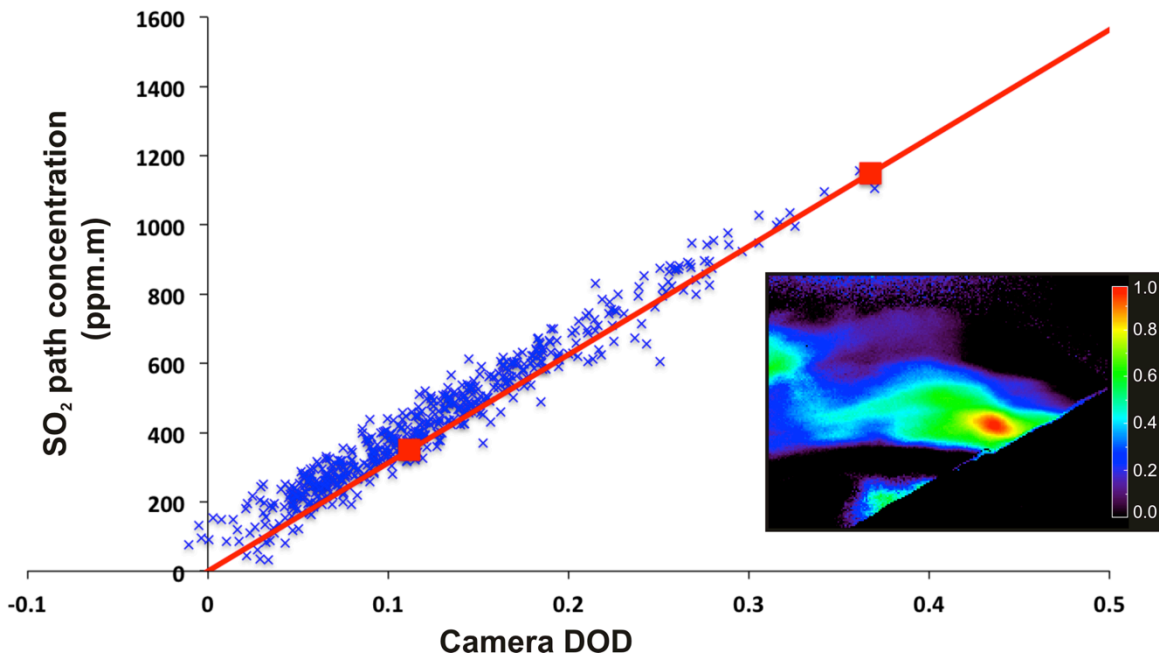
Figure 3.3: Example of calibration for data acquired on June 1st, 2013. The large red squares are the measured DOD of two gas cells of known concentrations placed directly in front of the camera lenses during calibration (350 and 1150 ppm·m, respectively). The solid red line is a linear fit through the cell values (see discussion of this on pages 54-55). The insert shows the values of the correlation factor (R^2) between the time series of SO$_2$ path concentrations from the USB2000+ data and the time series of DOD calculated for each pixel in the data set. The values extracted at the location of the highest correlation factor are plotted with small blue Xs.
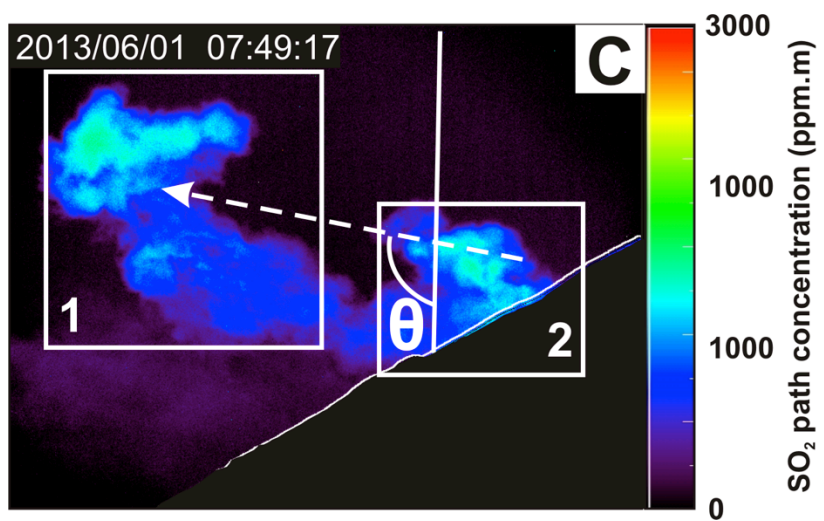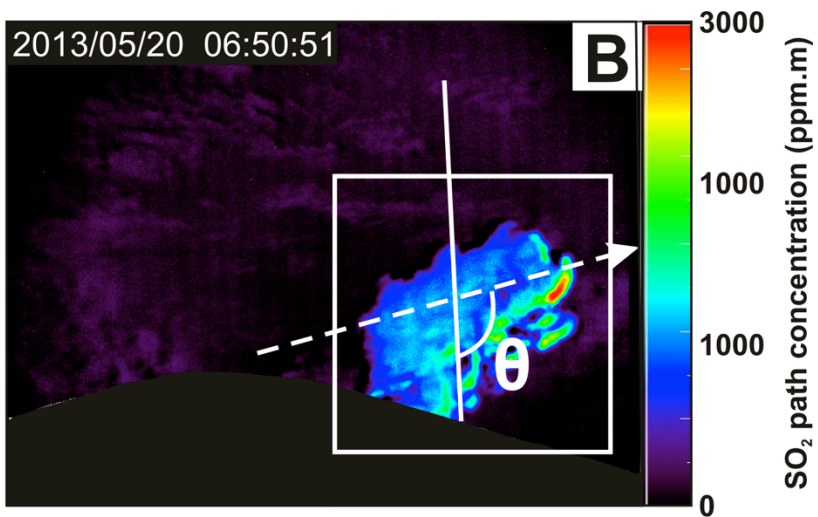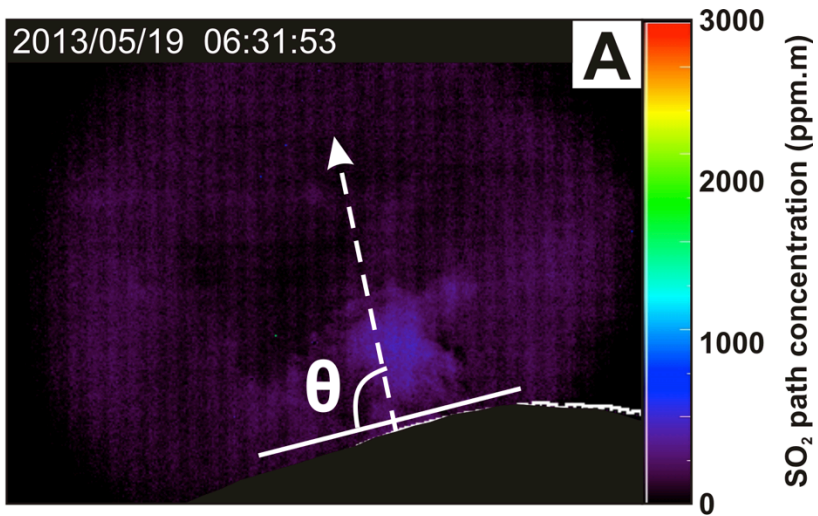
Figure 3.4 (previous page): Three examples of path concentration maps produced by the SO$_2$ camera. A) Quiescent degassing on May 19th. B) Type I event on May 20th. C) Type II event on June 1st. Emission rates on Figure 6 are calculated using the cross sections described in these images. Plume speed is calculated over the entire data sequence by cross-correlating the time series of emission rates retrieved at those cross-sections, with time series retrieved at cross-sections farther downwind. Theta (θ) is the angle between the cross-section and the drifting axis of the plume. It is used to correct the apparent wind velocity for obliquity. Individual puffs are outlined with boxes corresponding to the boxes in Figure 3.5.

3.3 SO₂ Emissions at Semeru

I took the SO$_2$ camera to Semeru for two consecutive campaigns: May 16-22 and May 31-June 3, 2013. I observed activity every day, for as long as the weather allowed, which was usually between 6am and 9am. I chose a vantage point on the Kalimati plain, north of the summit, at the end of a well-traveled hiking route. My vantage point was located 3.18 km away from the active crater and ~1000m below the summit (see Figure 3.2). Unfortunately I did not have a direct line of sight to the active vent, which is located several hundreds of meters below the summit on the opposite side of the edifice. Potential vantage points on the south side of the volcano (such as the volcano observatory where the webcam is installed) are located over 10km away from the vent, making camera measurements impossible. Explosive events sent gas bursts with low ash burden several hundreds of meters to a kilometer above the vent. Plumes from quiescent degassing on the other hand did not rise as high and I was not able to observe quiescent degassing every day. Wind direction was variable during my observation period, and I observed a drifting plume only when the wind was pushing it into my field of view, blowing either east or west. When the wind was blowing north (toward us) or south (away from us), SO$_2$ measurements were impossible.

Figure 3.5 summarizes the results of my observations. I measured degassing on 7 separate days, during periods ranging from 20 mins to several hours. I observed 6 individual explosive events, as well as quiescent degassing prior to and after the events.

Most explosions could be described as single pulses drifting quickly across my field of view. I will refer to this type of event as type I. Integrated total masses of SO_2 measured for type I events range from 200 to 500 kg, emitted over an average duration of 5 minutes. The explosion observed on June 1st was of a different sort. It consisted of 3 individual pulses, each of them with masses of 150-300 kg of SO_2, followed by a period of increased emissions (coda), which declined back to the average passive emissions over several minutes. I refer to these events as type II. The duration of the type II event, including the coda, was ~15 minutes, for a total emitted mass of 1460 kg of SO_2. Average quiescent SO_2 flux observed between these explosive events ranged from 0.11 to 0.62 kg s^{-1}.

In order to understand how representative my measurements are of the overall activity at Semeru, I conducted a simple survey, using images produced by the webcam installed at the Gunung Sawur Volcano Observatory (GSVO in Figure 3.1). The images are updated every minute and available through the website of the Indonesian Volcanological Survey (VSI: http://www.vsi.esdm.go.id). I visually inspected the images over a period of 5 months during the dry season (June-October 2013), and catalogued the observed explosive events. Observation was limited to early morning hours, after which clouds would block the view of the summit. Figure 3.6 summarizes my results. I observed

Explosion: 437 kg

Average quiescent emission: 0.19 kg s^{-1}

May 16, 2014

Average quiescent emission: 0.12 kg s^{-1}

Explosion: 412 kg

May 18, 2014

Average quiescent emission: 0.47 kg s^{-1}

Fig. 4A

May 19, 2014

Explosion: 252 kg

Fig. 4B

Average quiescent emission: 0.46 kg s^{-1}

May 20, 2014

Average quiescent emission: 0.17 kg s^{-1}

Explosion: 195 kg

May 31, 2014

Explosion in 3 pulses:
1: 297 kg
2: 243 kg
3: 159 kg

Fig. 4C

Increased emission: 663 kg

Average quiescent emission: 0.62 kg s^{-1}

June 1, 2014

Explosion: 258 kg

Average quiescent emission: 0.42 kg s^{-1}

June 3, 2014

Emission rate (kg s^{-1})

Emission rate (t d^{-1})

Local time (UTC+7)

61

Figure 3.5 (previous page): Emission rates measured at Semeru. X-axis represents 90 mins of local time (note that start times are different for each day). Sampling rate for all data sets is 5 seconds (0.2 Hz). Y-axis is the emission rate in kg s^{-1} (left) and t d^{-1} (right). I calculated the total emitted mass of SO_2 for each explosive event. The average emission rate during quiescent phases is denoted by a black horizontal line. The specific events illustrated in Figure 4 are outlined on this figure with dashed boxes.
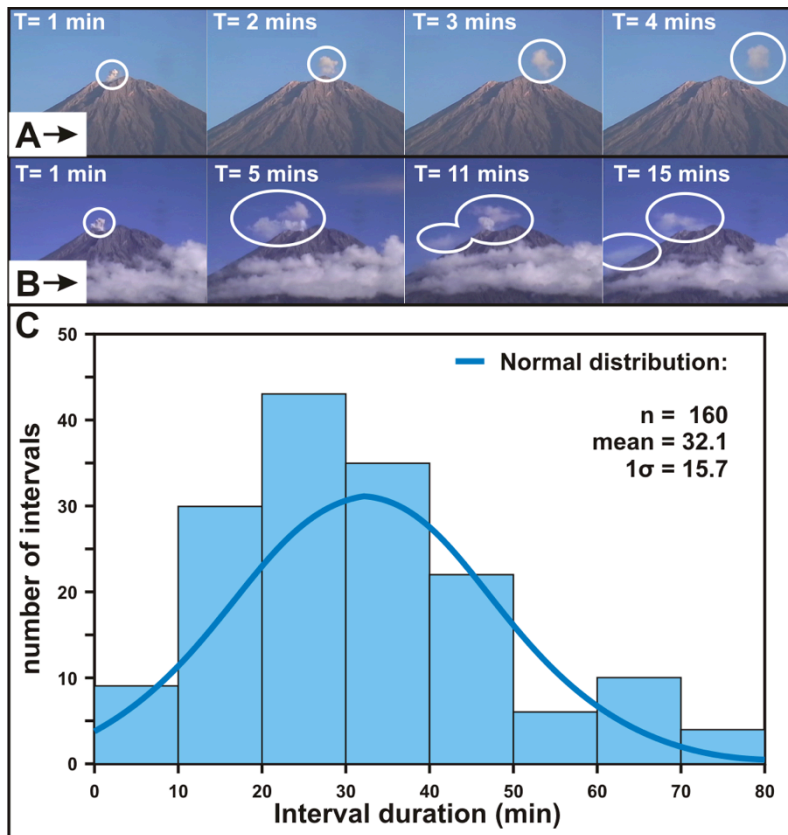
Figure 3.6: Results of the webcam survey. A) A short explosion with a single pulse (type I). This type of event represents the majority of the observed activity. Images are shown at 1-minute intervals from June 26th, 2013. B) A longer explosion with several distinct pulses (type II). Images are shown at 3-minutes intervals from June 29th, 2013. Note the persistence of high emissions up to 15 mins after the start of the event. C) Histogram showing the distribution of the measured intervals between explosions. The data consist of 160 observed intervals with a mean duration of 32.1 ± 15.7 mins. The curve represents the equivalent normal distribution.

a total of 160 intervals between consecutive explosive events, with durations ranging from 5 to 80 minutes. The mean interval is 32.1 ± 15.6 (1σ) minutes, though the distribution of the measured intervals is not strictly normal, and is slightly shifted towards lower values. The majority of the observed events occurred at intervals of 20 to 40 minutes. Most events (> 90 %) were similar to the explosions I qualified as type I above, consisting of a single pulse of short duration (Figure 3.6A). I identified 12 events similar to the type II event described above, with several distinct pulses followed by a longer period of increased emission (Figure 3.6B).

Based on these webcam observations, I estimate that a typical day of emissions at Semeru consists of 48 explosions: 44 short single-pulse events (type I: 5 mins duration; 200-500 kg SO_2) and 4 longer multi-pulse events (type II: 15 mins duration; 1460 kg SO_2 per event), amounting to a total of 280 minutes (~4.7 h) of explosive activity per day. Corresponding daily emissions are 8,800-22,000 kg of SO_2 from type I events and ~5800 kg of SO_2 from type II events, totaling ~14,600-27,800 kg of explosively-released SO_2. Explosive events are separated by periods of quiescent degassing, with rates of 0.11-0.62 kg s^{-1} over a total period of 1160 minutes (~19.3 h), representing a total of 7,600-43,200 kg of SO_2 released quiescently per day. Therefore I calculate the total daily average SO_2 emissions of Semeru to be between 22,000 and 71,000 kg (22-71 t d^{-1}). This corresponds to a yearly output of 8,000-26,000 metric tons of SO_2. Approximately 35-65% of that mass is released during explosive bursts, with the remainder released during quiescence.

Note that my measurements likely represent a minimum value, as the drifting plumes were often partially masked by the volcanic edifice in my field of view.

SO$_2$ emissions at Semeru are of the same order of magnitude as that of other volcanoes with similar periodic activity. I consider three volcanic centers: Stromboli (Italy), Santiaguito (Guatemala) and Karymsky (Kamchatka, Russia) for comparison. These other centers exhibit a wide range of compositions in terms of their eruptive products, from basaltic (Stromboli) to dacitic (Santiaguito). They have also been relatively well studied over the past 20 years, and their SO$_2$ emissions have been reported in the literature. Frequencies of explosions vary from center to center, and over time at each center, but the typical activity at all three volcanoes consists of short-lived discrete explosions at rates of several to several hundred events per day. Table 3.1 summarizes a number of average values for SO$_2$ released at the three comparison volcanoes, as well as the findings of my study. The highest emission rates are found at Stromboli volcano, where emissions range between 100 and 1400 t d^{-1}, with mean values of ~300 t d^{-1} (Allard et al., 2008; Allard et al., 1994; Burton et al., 2009). Emissions at centers with more evolved compositions tend to emit slightly lower amounts of SO$_2$. Fischer et al. (2002) measured emission rates of 0-140 t d^{-1} at Karymsky volcano in 1999. Santiaguito's emissions were measured at an average rate of 120 t d^{-1} over the period 1999-2002 (Rodriguez et al., 2004), and 50-100 t d^{-1} in 2008 and 2009 (Holland et al., 2011).

	Average daily emissions [t d^{-1}]	Average quiescent degassing rate [kg s^{-1}]	Average mass in explosive event [kg]	% of emissions released during explosive events
Semeru	21-60	0.1-0.5	200-1300	35-60
Karymsky	0-140	<0.1	100-1500	93-97
Santiaguito	50-100	0.4-1.0	200-700	10-30
Stromboli	100-1400	1.0-2.0	15-40	3-8

Table 3.1: SO$_2$ emissions at Semeru, Karymsky, Santiaguito and Stromboli.

It should be noted that the studies cited for the documentation of emission rates at these three volcanic centers used different methods, and that those methods have varying degrees of precision and accuracy. In particular, the presence of ash in a gas plume can lead to the overestimation of the retrieved SO$_2$ burden and is treated differently in the various studies. DOAS methods (e.g., Allard et al., 2008; Allard et al., 1994; Rodriguez et al., 2004) are less sensitive to the presence of ash in the plume because they use high-resolution spectra to fit the detailed absorption features of SO$_2$. Holland et al. (2011) used an SO$_2$ camera method with a single filter, and corrected for the effect of ash by using simultaneous scans with a DOAS spectrometer. Burton et al. (2009) at Stromboli also used a single filter and did not correct for the effect of ash. However, measurement of SO$_2$ emissions are generally performed on plumes with very low ash burdens in order to avoid such potential interferences, and the aforementioned references all report plumes with minimal ash content, as is the case for the plumes in my study. I am convinced that all measurements in Table 1 were either performed on plumes with negligible ash

contents, or accounted for the effect of ash absorption in a reasonable fashion. In my study, all the explosive plumes had a very low ash burden, and the images from filter B allowed us to account for the absorption of light by the ash when it was present.

3.4 Implications for Eruption Mechanisms

I found that at Semeru volcano 35-65% of the emissions are released during explosive events. In comparison, explosive events at Stromboli account only for 3-8% of the total emissions (Mori and Burton, 2009), with a greater frequency of explosions (13 events per hour) and a much smaller mass of SO_2 per event (15-40 kg). Explosive events at Stromboli are believed to be the result of gas coalescence in the upper part of the conduit (Jaupart and Vergniolle, 1988) in a generally open system where gas flow is not impeded, and therefore the gas phase is largely decoupled from the magma itself. In contrast, explosions at Karymsky in 1999 accounted for > 90 % of the total emissions (Fischer et al., 2002), with larger masses of SO_2 per event released (1000-1500 kg). In the Karymsky case, the authors suggest a mechanism of accumulation and pressurization of gas beneath a viscous plug at the top of the conduit, leading to the sudden release of volatiles, and an otherwise low level of degassing between the explosive events. A similar mechanism has been suggested at Santiaguito (Holland et al., 2011), where gas release is thought to occur through the opening and closing of a network of shear fractures along the edges of the conduit. At both Karymsky and Santiaguito, the explosive events are characterized by a sharp onset and sudden increase in gas emission

rate of at least one order of magnitude, interpreted to be associated with viscous plug destruction or the opening the gas pathways through or around the plug. Many of the events I documented at Semeru exhibit the same characteristic trends in the SO_2 time series as those observed at Karymsky and Santiaguito. Fischer et al. (2002) also distinguish between two types of events at Karymsky, with type I events showing a rapid return to base levels, and type II events showing a longer waning period of increased emissions. My measurements at Semeru show many of the same characteristics and I interpret the degassing patterns to be the manifestation of a mechanism in which a viscous cap plugs the conduit and is then breached when sufficient magma pressure builds beneath it. I also suggest that the quiescent degassing represents open system degassing accompanied by bubble or crack collapse, leading to the creation of a new plug or reinforcement of an existing plug between events. This mechanism is consistent with the patterns of ground-deformation observed by Iguchi et al. (2008) and Nishimura et al. (2012), and may be interpretable in the SO_2 time series in Figure 3.5.

I have observed no significant difference (increase or decrease) in the length of the intervals directly preceding or following type II events. This pattern suggests that they are not the result of a longer build-up of pressure beneath the cap, nor do they lead to longer repose intervals. However, type II events tend to occur on days with visibly (and measurably) stronger quiescent degassing between explosions. The degassing prior to the type II event on June 1st shows the highest average emission rates of all the periods of quiescent degassing measured with the SO_2 camera (0.62 kg s^{-1}), with peaks of up to 2 kg

s^{-1}. An increased level of quiescent emissions may be the result of a higher magma supply rate. The observation of multiple rock falls, which sometimes turn into small pyroclastic flows, on days with type II events and high quiescent degassing further supports this hypothesis. According to this concept, during phases of higher magma supply rate, the same interval of time allows for pressurization of larger masses of bubbly magma beneath the plug, leading to larger and longer bursts. Moreover, this same scenario may prevent fast resealing of the vent after destruction of the plug, leading to the observed multiple pulses as well as longer burst duration.

3.5 Conclusions

Activity at Semeru is characterized by short-lived discrete explosive events with low ash burden. The average interval between explosions was measured at 32.1±15.7 minutes using daily observations with a webcam over a period of 5 months between June and October 2013. I have measured the SO_2 emissions during and between some of these events using an SO_2 camera. The average emission rate during periods of quiescent degassing is 0.11-0.62 kg s^{-1}. Masses of SO_2 emitted during single explosive events range between 200 and 1460 kg. In general, 35-65% of all SO_2 emissions occur during explosive events. I distinguish between two types of explosive events based on my observations with both the SO_2 camera and the webcam. Type I events are short (~5 mins) and consist of a single pulse of gas and ash; the emissions quickly return to base levels. Type II events are longer (~15 mins) and often comprise several distinct pulses

followed by a longer waning period before emissions return to base levels. Type I events represent > 90 % of the explosive activity, and release an average of 200-500 kg of SO_2 per event, while the single type II event I observed with the SO_2 camera released a total of 1460 kg of SO_2. In both types of events the explosions are characterized by a very sharp onset of high SO_2 emissions. I suggest that the degassing and periodicity at Semeru is controlled by the existence of a viscous plug at the top of the conduit, which promotes an increase in pressure in the underlying bubbly magma and gas that ultimately leads to explosive eruptions when the pressure exceeds the strength of the plug. This mechanism is consistent with other geophysical observations at Semeru, and with observations of degassing patterns at other volcanic centers that are persistently active, and exhibit continuous degassing and repeated short explosions at regular intervals.

CHAPTER 4

OBSERVATION OF PERSISTENTLY ACTIVE EXPLOSIVE ACTIVITY WITH

SATELLITE DATA

Regular and sustained observations are essential to the understanding of a volcanic system, and are especially important when it comes to persistent periodic systems. However, relatively few volcanoes are monitored continuously, either due to a lack of resources or because of their location in remote environments. Satellite imagery offers a potentially valuable alternative source of information. A number of instruments are currently in orbit that can capture volcanic activity around the world and in the most remote areas. Geostationary satellites offer continuous temporal coverage over vast areas, but the high altitude of their orbits limits their spatial resolution and typically precludes the observation of local or even regional activity. The type of activity that is the focus of this work is typified by discrete explosions of low to moderate magnitude, separated by periods of relative quiescence that can range from minutes to days. The associated plumes are very commonly confined to the lower layers of the atmosphere, where the emitted gases and particulates have a relatively shorter residence time than those that reach the stratosphere; a fact which combined with their relatively small size, limits the time window over which they are observable and/or detectable to periods of minutes to hours. Moreover, degassing may not be happening at all during the quiescent phases. In this chapter, I examine the ability of satellite-based instruments to detect and quantify

volcanic emissions from persistently active explosive centers. In keeping with the previous chapters, I will focus on SO_2 emissions, as it is the easiest gas species to detect and is used widely for monitoring.

4.1 Choosing the Appropriate Sensor

Several instruments currently in orbit around Earth have the capacity to measure SO_2 abundances using the absorption features of the molecule either in the ultraviolet spectrum, or in the thermal infrared. A number of hyperspectral instruments operating in the UV offer the most accurate methods for the retrieval of SO_2 column amounts. These sensors were originally designed for routine monitoring of the ozone layer in the upper atmosphere, which presents absorption features in the same region of the UV spectrum as SO_2. Unfortunately, these hyperspectral instruments typically have relatively low spatial resolution (pixel sizes of several tens of kilometers) and the amount of light needed to produce an acceptable signal-to-noise ratio (SNR) is larger than that required for multispectral instruments because the photons collected within a given region of the EM spectrum are divided into many small intervals. To compensate for this loss of photons, instruments can be designed with an increased integration time or a decreased number of pixels in a given field of view, both of which allow more radiation to reach the sensor. Increasing the integration time, however, can be problematic for instruments aboard a fast moving satellite. On the other hand, hyperspectral instruments are often designed to offer frequent (up to multiple times per day) complete coverage of the Earth's surface. Such

sensors have been used to monitor large volcanic plumes from explosive eruptions (e.g., Bluth et al., 1992; Carn et al., 2009b; Lopez et al., 2013) and, with recent technological improvements, passive emissions from persistent large emitters (e.g., Bani et al., 2009; Campion, 2014; Carn et al., 2006).

OMI (Ozone Monitoring Instrument)   The latest in the generation of such instruments, OMI measures reflected sunlight in the visible (350-500 nm) and UV (270-380 nm). The algorithm used to retrieve SO_2 abundances is an extension of the band residual difference (BRD) algorithm developed by Krotkov et al. (2006), which uses the measured radiances at four wavelengths at the edges of the SO_2 absorption cross-section in the range 310–314 nm to estimate total vertical column SO_2. The instrument's large field of view (114°), combined with its 14 daily orbits, offers global daily coverage. And with a relatively high resolution of 13x24 km^2/pixel it can detect passive degassing as well as explosive activity. Retrievals for several regions of interest for volcanic activity and atmospheric pollution are published daily on a NASA website (http://so2.gsfc.nasa.gov/). But even with the low detection limit of the instrument in terms of column amount, a significant mass of SO_2 is required in order to produce a measurable signal in one or more pixels.

The characteristic absorption features of SO_2 in the UV are the result of electronic transitions in the outer orbitals of the molecule. But SO_2 also has absorption features in the infrared corresponding to various vibrational modes of the molecule, most notably in

73

the thermal infrared (TIR). The absorption features of water vapor - a ubiquitous component of the atmosphere on Earth - limit the possibility of observation in the TIR to a small window between 8 and 12 μm. Two prominent absorption features of SO_2 are present in that window (see Figure 4.2) and multispectral instruments, such as MODIS and ASTER described below, operate in that region of the spectrum and have been used to observe volcanic activity around the world in a variety of specific cases (e.g., Campion et al., 2010; Pugnaghi et al., 2006; Urai, 2004). A number of geostationary weather satellites operate in that region of the spectrum (e.g., GOES operated by the National Oceanic and Atmospheric Administration; SEVIRI operated by the European Spatial Agency). However, orbiting at an altitude of ~36,000 km, they offer a very limited spatial resolution and are very unlikely to be suitable for the type of activity considered here. For this work, I will focus on analysis of data from two multispectral NASA instruments in near polar orbits, described below, that are used frequently for volcanic observation.

MODIS (Moderate Resolution Infrared Spectroradiometer)   The MODIS system actually comprises two identical instruments onboard two different satellites: Terra and Aqua. It offers 36 bands spanning the visible and thermal infrared wavelengths. It was intended for use in climate monitoring and weather forecasting. With a return period of up to 4 times a day in polar regions, it allows for frequent acquisition and offers a spatial resolution of 250 m per pixel in the visible and 1000 m per pixel in the TIR, over a wide swath of 2330 km. Figure 4.1A shows the response functions of the TIR filters on MODIS.

74

ASTER - Advanced Spaceborne Thermal Emission Radiometer   The ASTER instrument consists of three sensors with separate optics: a visible/near-infrared (VNIR) sensor offering 3 bands with a resolution of 15 m/pixel; a short-wave infrared sensor (SWIR) offering 6 bands with a resolution of 30 m/pixel, and a thermal infrared sensor (TIR) with a resolution of 90 m/pixel in 5 bands. Figure 4.1B shows the filter responses for the 5 thermal bands of ASTER.
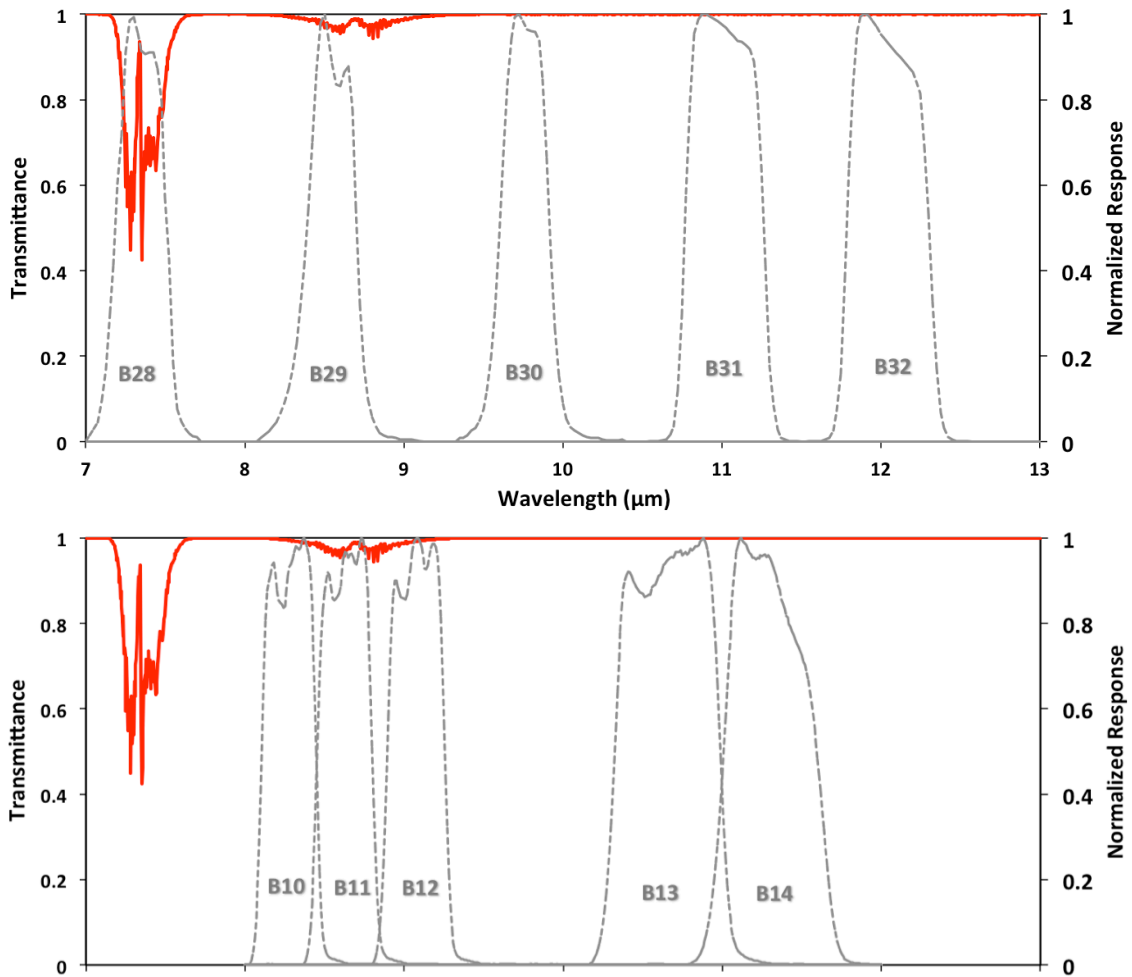
Figure 4.1: Absorption spectrum of SO_2 in the thermal infrared [red] with A) Response functions of the 5 TIR channels of MODIS; and B) Response function of the 5 TIR channels of ASTER
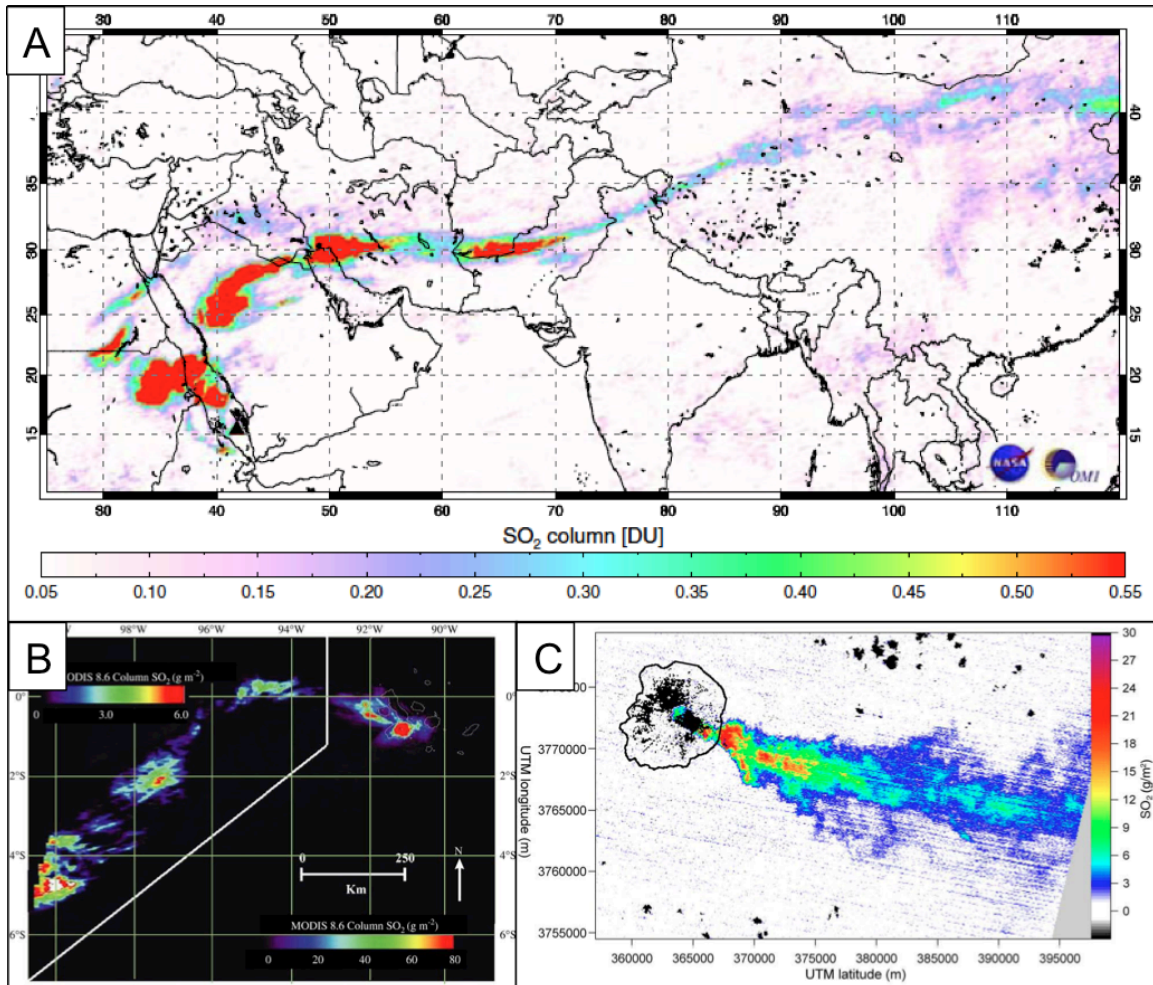
Figure 4.2: Examples of satellite retrievals of SO_2 column amounts with 3 different sensors: **A)** OMI map of the eruption cloud from Jebel at Tair in Yemen, compiled over October 1-13, 2007 (Carn et al., 2009a); **B)** MODIS map of the eruption cloud from Sierra Negra volcano, Galapagos, on October 26, 2005 (Thomas et al., 2009); **C)** ASTER map of the plume from Myake-Jima volcano, Japan, on April 1, 2001 (Campion et al., 2010).

In general there exists a tradeoff between spectral, spatial and temporal resolution. Spectral resolution is the ability to discretize a given region of the spectrum into individual intervals (bands). Hyperspectral instruments typically use diffraction grids to disperse the incoming radiation onto an array of sensor elements. This means that the total amount of photons ultimately reaching an individual sensing element is a function of the number of bands on the instrument. In order to compensate for the loss of signal incurred when splitting the incoming light into many channels, one of two strategies can be employed to increase the amount of light reaching the sensor: a longer integration time or a larger field of view. Because satellites move with respect to the object they are imaging, there are limits on the integration time that can be applied before incurring geometrical distortions that will compromise the interpretation of the data. And so, at a given wavelength, hyperspectral instruments usually have pixels of larger size than multispectral instruments. Multispectral instruments on the other hand, utilize band-pass filters to collect light from only a limited number of bands of relatively large width. As a result, they can achieve sufficient signal-to-noise ratio at a much higher spatial resolution.

Table 4.1 summarizes the resolution specifications of the three instruments considered above. The type of activity I am trying to characterize here has never been studied with satellite data despite the frequency of individual eruptions (10s of times per day at several locations worldwide), perhaps because their contribution to the global volcanic input to the atmosphere is thought to be very small. I explored the databases of all three sensors for the last decade and did a systematic qualitative search for data in the

78

last decade. I started my search with ASTER, which has the longest return period (16 days) and the highest spatial resolution. Moreover, ASTER data is only collected upon request, whether by users or by a number of automated surveillance programs. For example, the MODVOLC program (Wright et al., 2004) uses the continuously acquired MODIS data to detect thermal anomalies at a number of volcanic targets and trigger ASTER acquisition in times of unrest. Once individual events were qualitatively recognized in ASTER data, I searched the other two databases for simultaneous data. I focused on 4 volcanic targets (see section 4.3 for details) in order to limit the scope of the search. The sensor with the highest temporal resolution (OMI – twice daily coverage of the globe) has a spatial resolution much too low for the detection of the small events of interest here. MODIS also has a return period of 1 day or less, but even with a pixel size of 1km, none of the events I found in the ASTER images were even qualitatively recognizable in the MODIS images. It quickly became apparent that a very high spatial resolution was required in order to detect persistently active explosive activity. In the following sections, I will describe my efforts to quantify SO_2 emissions from 4 different targets using selected ASTER images.

4.2 <u>SO_2 Retrieval in the TIR</u>

Two methods exist for the retrieval of SO_2. The first one (Prata et al., 2003) uses the strong absorption feature at 7.3 μm (see Figure 4.1). However, its use is limited to application in the upper atmosphere because of interference from water vapor absorption at that wavelength. The second method uses the weaker absorption feature centered at

79

8.3 μm following a method originally developed by Realmuto et al. (1994). While UV instruments measure reflected sunlight, sensors operating in the TIR measure radiation emitted from the ground and the atmosphere. The retrieval techniques in the TIR are based on an iterative forward modeling approach, where the radiance at the sensor (or the equivalent brightness temperature) is simulated using a radiative transfer model of the atmosphere, and is then compared to the measured values in the original scene. The process is repeated until the original scene is simulated to within some specified tolerance.

	Spatial Resolution	Spectral Resolution	Return Time	Detection limit	
				Column amount $(g\ m^{-2})$	Mass of SO_2 (tons)
OMI	13 x 24 km^2	~0.5 nm [307-383 nm]	1 day	0.02	6.6
MODIS	1 x 1 km^2	6 band s in the TIR [3-15 μm]	1 day		
ASTER	90 x 90 m^2	6 bands in the TIR [8-12 μm]	16 days	1-2	8.1

Table 4.1: Specifications of the three sensors considered for the retrieval of SO_2.

4.2.1 Radiative Transfer Modeling

The radiation reaching the sensor (L_s) can be described by the following radiative transfer equation, where wavelength dependence has been omitted for clarity:

$$L_s = \varepsilon \cdot B(T_0) \cdot t_0 + L_u + L_d \cdot (1 - \varepsilon) \cdot t_0 \quad (4.1)$$

The terms on the right-hand-side of the equation are arranged in order of increasing magnitude. The first term represents the radiation emitted by the surface and corrected for the transmission through the atmosphere. *B(T)* is the blackbody Planck function for temperature *T*, ε is the surface emissivity, t_0 is the transmittance of the entire atmosphere. The second term is the upwelling radiance (L_u): light emitted upward by the atmosphere to the sensor. The third term is the downwelling radiance (L_d): light emitted towards the surface by the atmosphere and reflected by the ground, also corrected for transmission through the atmosphere. In an atmosphere vertically divided in infinitesimal plane parallel segments, the upwelling radiance can be described as the cumulative emission of each layer, as a function of its temperature (T_z) and emissivity (ε_z), and the attenuation due to the column of atmosphere directly above it (t_z):

$$L_u = \int_0^H \varepsilon_z \cdot B(T_z) \cdot \frac{\partial t_z}{\partial z} dz \quad (4.2)$$

Intuitively one could make the assumption that the downwelling radiance should be equal to the upwelling radiance; and if the atmosphere were limited to the vertical slice directly below the sensor - an assumption that is acceptable when considering the upwelling radiance – that statement would be true. However, and in addition to the vertical downwelling radiance, one must also consider the light emitted by the atmosphere outside of the field of view of the instrument, such that the actual downwelling radiance can ultimately be represented as a fraction d (> 1) of the upwelling radiance in a uniform atmosphere. Because the emissivity of most surface materials is close to 1, the downwelling radiance term is often very small in comparison with the other two.

In order to simplify the problem, radiative transfer models consider a vertically stratified atmosphere, where layers are assumed to be laterally uniform and extend infinitely in the horizontal direction. This assumption is acceptable when working with relatively small images, where the atmosphere can indeed be considered to be uniform over the entire scene, and where the curvature of the Earth can be ignored. Each layer is assigned a value for temperature, pressure and relative humidity (see Figure 4.3). Transmittance for each layer is calculated as a function of the volumetric concentration of water vapor and other absorbers present in the layer. Simple models usually assume universal values for the concentrations of the other common absorbers (mainly O_3 and CO_2). The transmittance in a layer A (t) is then calculated using a database of measured cross-sections of the various gases:

$$t = \prod_i c_i \cdot \sigma_i \qquad (4.3)$$

where c is the path concentration of a given gas i and σ is the absorption cross-section of that gas. The path concentration is a measure of the density of the absorbing molecules along the light path considered, and is easily calculated from a volumetric concentration. Its units are molecules per unit area (usually molec m^{-2}). The absorption cross-section of a substance can be measured in a controlled environment and is given in the inverse units of m^2 molec^{-1} such that transmittance values are always between 0 and 1. Layers are considered to be homogeneous between their boundary altitudes, such that they can be described by a single value of transmittance. The following relationship describes the relationship between a material's properties with regard to electromagnetic radiation:

$$t + r + \varepsilon = 1 \qquad (4.4)$$

In this equation, t is transmittance, r is reflectance and ε is emissivity. The reflectance of atmospheric gases in the infrared can be considered negligible, so that the emissivity is simply the complementary value to the transmittance.
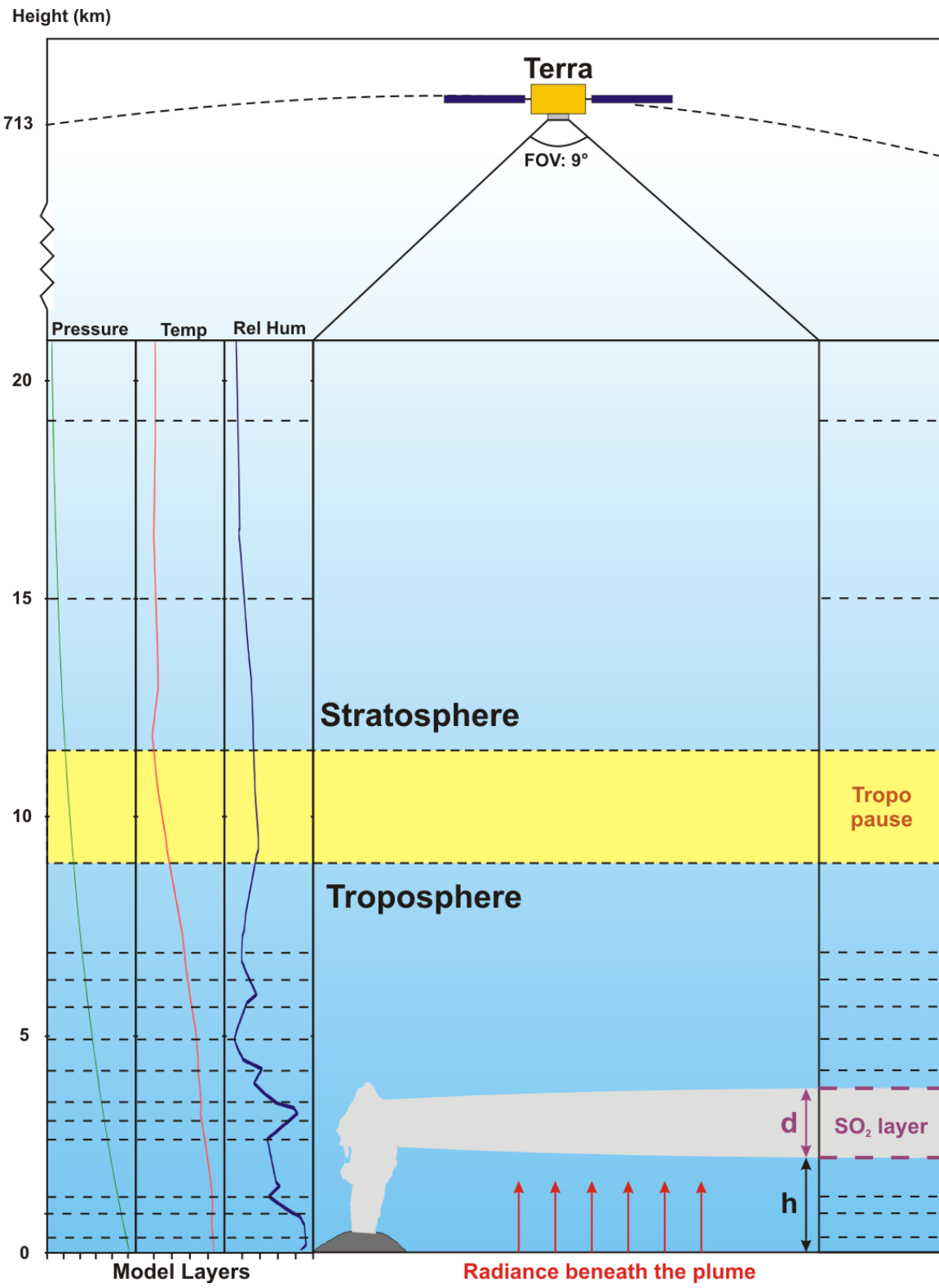
Height (km)

713

Terra

FOV: 9°

Pressure   Temp   Rel Hum

20

15

Stratosphere

10   Tropo
            pause

Troposphere

5

d   SO₂ layer

h

Model Layers

Radiance beneath the plume

84

Figure 4.3 (previous page): Illustration of the forward radiative transfer modeling used to determine SO_2 column abundances in ASTER images. Required inputs are: 1) an estimate of the temperature and emissivity spectrum of the surface for each pixel beneath the plume; 2) Vertical profiles for Pressure (green), Temperature (red) and Relative Humidity (blue) in a layered atmosphere; 3) Height and thickness of the SO_2 layer. Concentration of SO2 in the plume is assumed to be uniform and increased until the computed radiance at the top of the atmospheric column matches the measured radiance at the sensor.

In the retrieval method, a plume layer is added to that vertical profile with a prescribed height and thickness. SO_2 is added to the list of considered gases and its concentration is changed incrementally until the radiance at the sensor predicted by the radiative transfer model matches the measured radiance in the original image. The modeled radiance is calculated over the desired range of wavelengths at a resolution that far exceeds that of the ASTER instrument. The instrument response for each band is therefore needed to calculate the simulated radiances in each band. Best fit is determined using least square algorithm at multiple wavelengths.

I used the AST_L1B product (registered radiance at sensor) as the basis for the retrievals. Surface emissivity was computed from the AST_09T data product (surface leaving radiance). This product uses MODIS data acquired at the same time to produce a modeled atmosphere above the scene and compute an atmospheric correction. The result is a measure of the ground-leaving radiance as well as the atmospheric contribution to the overall radiance for each pixel. From this data, I calculated the ground temperature and emissivity values in all five thermal bands. In order to determine emissivity values as well as the temperature – 6 unknown values - from a 5-band dataset, the number of unknowns must be reduced. One way to do this is to assume a reference channel where the emissivity is assumed to be close to one (usually 0.97). This method assumes all the pixels have the same emissivity in one of the channels, regardless of the nature of the surface. Instead I have chosen to use an emissivity normalization method, which computes the temperature for every channel using a constant emissivity (again, usually

0.97). The highest temperature is assumed to be the actual temperature, and the emissivity in the other channels is computed using that same temperature. The atmospheric profiles used for the radiative transfer modeling in the retrieval process are the same MODIS-derived data used to correct the original ASTER data. These three pieces of data are the required inputs for the retrieval software.

I retrieved SO_2 column amounts using Plume Tracker, a software developed at the Jet Propulsion Laboratory following work by Realmuto et al. (1994). The software is written as a Graphic User Interface in IDL (Interactive Data Language) and uses the MODTRAN (MODerate resolution atmospheric TRANsmission) radiative transfer model for the iterative forward modeling approach. The input images were prepared using ENVI as well as custom routines in IDL.

4.2.2 *Limitations*

In this approach, a number of assumptions have to be made about the initial and boundary conditions of the system. The precision and accuracy of the modeled SO_2 column amounts depends on the validity of these assumptions. The software was not originally designed for use on tropospheric plumes of low column amounts. Here I describe the major assumptions associated with the software implementation and discuss the potential effects of their violation.

Surface emissivity

The first crucial parameter in the retrieval process is the determination of the temperature and emissivity of the surface beneath the plume. Unfortunately, because the plume is obscuring the ground, it is impossible to determine these parameters directly from either the original or the atmospherically corrected data. One solution could be to use images taken of the same area at a time when no plume was present. This approach however creates some issues because both temperature and emissivity can vary quickly over time, and the return time for ASTER is long. Two consecutive images in the ASTER database with sufficiently low cloud cover can be separated by a time of several months in the most optimistic cases, to several years. In that time, not only do ground temperatures change, but emissivity can also vary, for example due to vegetation changes, the appearance of a snow cover, or event changes in the sediment load in bodies of water. A second approach - the one I have opted to use – consists of choosing an area immediately outside of the plume to represent the ground underneath the plume. In so doing I am assuming a homogeneous ground surface in the region under the plume. In cases where the plume is travelling above a body of water, that assumption is relatively strong. But when the plume travels over land, there can be great variations along the travel path. When that was the case, I separated the retrieval process into several segments, using a different value of emissivity for different backgrounds. That approach produces discrepancies between the various retrieval runs, which can be difficult to merge. In all my data sets however, the discrepancies produced were within the margin of error of the method.

Atmospheric Profiles

In the absence of SO_2, the most important absorbing species defining the transmissivity of the atmosphere is water vapor. Therefore, it is crucial for any retrieval technique to have accurate estimates of atmospheric profiles (variations of pressure, temperature and water vapor content with height). One way of acquiring such profiles is to use atmospheric soundings. A balloon is released through the atmosphere and measures the parameters as it travels through the atmosphere. When it reaches a critical altitude, the balloon explodes and the sensors fall back to Earth. Such measurements are performed at many locations around the world, but they are usually concentrated around populated areas and are not uniformly distributed. Depending on the observation target, data may or may not be available for a station nearby. An alternative is to use atmospheric profiles derived from concurrent satellite data. The ASTER instrument flies aboard Terra, the same satellite that houses one of the two MODIS instruments. For each ASTER image, there is a simultaneous MODIS image. MODIS data are routinely used to produce atmospheric profiles for weather observations. Using the SWIR and TIR bands of the instrument and using a similar approach of radiative transfer forward modeling described above (but without the presence of SO_2), an atmospheric profile can be created for each MODIS pixel or group of pixels. The atmospheric product MOD07 offers atmospheric profiles at a resolution of 5x5 km^2. I can choose an atmospheric profile from a MODIS pixel (or group of pixels) above the region of interest, preferably not directly at the location of the plume, so as to avoid interference from the SO_2. The principal advantage of this method is its internal consistency. The MODIS atmospheric profiles are

89

the same profiles that are used to correct the ASTER L1B data and produce the AST09T products separating the ground radiance from the sky radiance. And since Plume Tracker uses the same radiative transfer model (MODTRAN), the predicted radiance is an exact match to the measured radiance when considering areas outside of the volcanic plume. That fact has been verified on all of my images prior to the retrieval of SO_2 in order to ensure that I had chosen an appropriate atmospheric profile.

Elevation

The third major parameter that needs to be constrained for the retrieval is the elevation of the plume. The atmosphere is thicker and more humid at low elevations. Therefore, most of the absorption of TIR radiation occurs in the first few kilometers above the ground. The amount of radiation entering the plume layer is a function of the slice of atmosphere present directly below it. If the plume is at low altitudes, the radiation reaching the sensor will also be strongly affected by the column of air on top of it. For those reasons, the elevation and thickness of the plume are key parameters that strongly affect the results of the retrieval. The plumes (or at least part of them, see below) were often optically thick and cast dark shadows in the visible bands. I was able to use those shadows to determine the height of the plume using simple geometric relationships. Figure 4.4 illustrates this principle. Knowing the sun zenith angle (SZA – α), the height of an object (h) is given by the following equation:

$$h = d \cdot tan^{-1}(\alpha) \tag{4.4}$$

where d is the measured distance between the vertical projection of the object edge and the equivalent point on the object shadow. Using the ASTER VNIR bands, this distance can be measured with an accuracy of 30 m. All four volcanic centers produce similar plumes and have been documented from the ground using photographs. Typically, plumes vary in thickness between 0.5 and 1.0 km near the source. They can spread as they move away from the source but they tend to spread laterally rather than vertically. Therefore, I assume that the height and thickness of the plumes remain constant over the entire area. This assumption is common when considering larger volcanic plumes. But because of the transient nature of the observed plumes, it stands to reason that it may not be accurate in the case of my target volcanoes. There is no practical way to detect changes in the plume thickness during travel without an additional source of information (such as ground-based observations), but it is worth keeping in mind when interpreting the results.

In a similar manner, ground elevation can cause significant variations in the measured radiance at the sensor by modifying the effective slice of atmosphere directly below the plume. These variations are especially strong in rugged terrain, as is the case close to many volcanic vents. For that reason, I limited my attempts to parts of the plume away from the vent, where the plume was drifting over terrain that could be considered to be at a relatively constant elevation. The effect of an erroneous ground elevation estimate is much more important when considering plumes that are close to the ground, where the

relative error to the thickness of the atmospheric slice below it is larger. Topographic

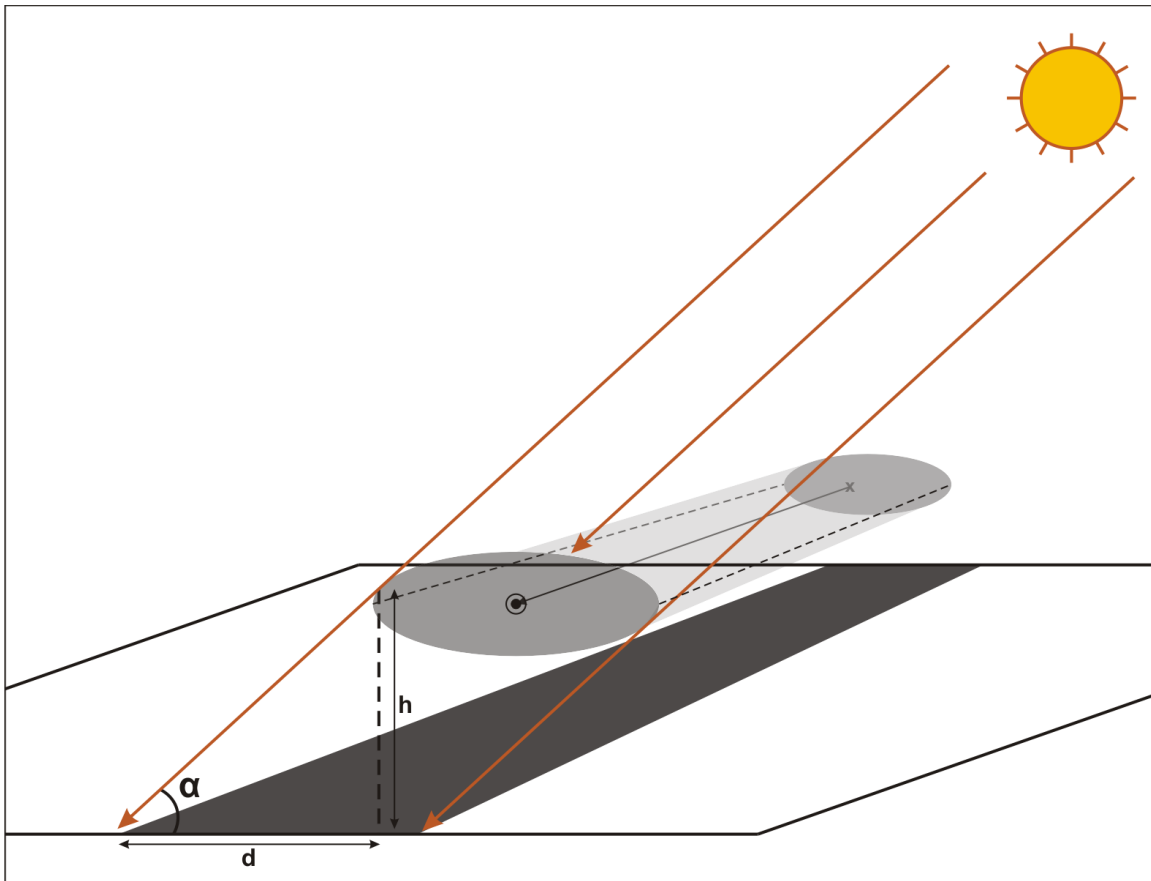variations in elevation therefore created noise in my data.

Figure 4.4: Illustration of the method for the determination of a the height of a volcanic

plume using its projected shadow in a daytime image.

Optical Thickness

Assumptions associated with optical thickness may have the most significant impact on the reliability and interpretability of results. The model assumes a plume (and surrounding atmosphere) that is transparent, aside from the effects of SO_2 and water vapor. The presence of particulates and aerosols (e.g., ash, water droplets, sulfate aerosols) will also result in absorption of radiation. This absorption is a relatively well-known potential problem and several recent studies have offered ways to detect the presence of those species, and possibly account for their effects (e.g., Corradini et al., 2009; Prata et al., 2008). However, the assumption of those methods is still that the plume is indeed transparent. With heavy aerosol or particulate load, there may come a point when the optical thickness approaches infinity effectively meaning that the plume is opaque. In such a case, the radiation measured by the sensor is only affected by the atmospheric column on top of the plume, and the corresponding brightness temperature is that of the top of the plume, unaffected by the presence of absorbing species within it. In such cases, the radiative transfer model is unable to reproduce the low values measured by the sensor, no matter how much gas is added to the plume, and SO_2 concentrations cannot be retrieved. This problem occurred for portions of the plume close to the source in many of my images, as the plumes are the results of small explosions and therefore may contain large proportions of water vapor and particulates. Further downwind, when the plumes had dissipated, their opacity was reduced and retrievals became possible again. However, I was unable to account for the presence of ash or aerosols in my images. The corrective methods described above rely on a the fact that small ash particles

absorb more strongly at 12 μm than at 11 μm (Prata, 1989). That difference in absorption can be exploited to differentiate ash clouds (which have negative brightness temperature difference - BTD) from water ice clouds (with a positive BTD), and even quantify the mass load of ash needed to produce the observed BTD. This correction was developed for the MODIS instrument. ASTER however, does not offer the appropriate channels capable of measuring this effect.

4.3 SO$_2$ Detection and Retrieval using ASTER

4.3.1 Target Volcanoes

Many volcanoes exhibit what can be described as persistently active explosive activity. Some exhibit intermittent activity with phases of high intensity separated by periods of reduced activity, possibly without emissions. I have decided to focus on 4 volcanoes with persistent activity and daily or weekly explosions, in order to maximize the chances of capturing the small events of interest. All four volcanoes can be described as open or semi-open systems, where degassing occurs on a continuous basis, even if it is in the form of periodic bursts with repeat intervals on the order of minutes to hours. I have searched the ASTER database for images over the target areas with low cloud cover (< 20 %) and checked for the presence of an eruptive cloud in the visible bands. Each of the target volcanoes yielded a small number of suitable scenes (typically 5 or less) over the operation time of the instrument (1998-present). Below I offer a brief description of each volcano and of its recent activity.

94

Semeru

Semeru is part of a large volcanic complex (Semeru-Tengger massif). It is a typical stratocone, rising to 3,676m above sea level on the South side of the massif. Since 1967 and the start of the most recent eruptive phase, the activity has been dominated by frequent small explosions with eruptive clouds rising from a few hundreds to a few thousands of meters above the vent (e.g., Iguchi et al., 2008; Nishi et al., 2007; Nishimura et al., 2012). As described in Chapter 3, these small explosions currently occur at a frequency of ~1/2 h, but that number has varied in the last decades between 5 mins and one hour. During my own period of observation with the SO_2 camera, I requested the acquisition of an ASTER image. The image was taken on May 10, 2013 but unfortunately, excessive cloud cover prevents the direct observation of the target area at the time of acquisition (around 10am, local time).

Karymsky

Karymsky is the most active volcano in the Kamchatka peninsula. It has known numerous periods of moderate explosive activity (VEI 1-3) in the last 100 years. The last eruption started in 2001 and is still ongoing. Ash plumes are observed every week, rising to altitudes of a few kilometers.

Santiaguito

Santiaguito is one of four actively degassing volcanoes in Guatemala (Rodriguez et al., 2004). The name Santiaguito actually refers to the most recent vent on a complex

of domes that has been growing in the crater left behind by the plinian eruption of Santa Maria in 1902 (Williams and Self, 1983). After a hiatus in activity, lava was extruded in the crater starting in 1922, considered to be the start of the current eruptive phase (Rose, 1972). Though the intensity has varied over that period (e.g., Harris et al., 2003; Rose, 1987), the typical activity is characterized by dome growth and small explosions. The interval between explosions in the last decade has varied from 30 minutes to several hours (e.g., Holland et al., 2011; Sahetapy-Engel and Harris, 2009).

Sakurajima

Sakurajima is an island in the bay of Kagoshima, on the island of Kyushu, Japan. This stratovolcano has been persistently active since 1955, and though activity occasionally moves between several vents at the summit, small explosions have been common during most of the recent eruptive phases (Bulletin of the Global Volcanism Network). Contrary to the other volcanoes above, Sakurajima often exhibits relatively high levels of degassing. Recent measurements using an SO_2 camera have revealed fluxes of 100-2000 t d^{-1} (1-23 kg s^{-1}), measured during the period 2007-2010 (Kazahaya et al., 2013). This study reported continuous passive degassing from Minamidake crater on the order of 1-6 kg s^{-1}, as well as variable explosive degassing (up to 23 kg s^{-1}) from the Showa crater where periodic explosions occur.

4.3.2 Qualitative Analysis

Figures 4.5-4.8 show subsets of selected ASTER images over the target volcanoes. In all cases, Panel A shows a false-color composite image created using the visible and near infrared (VNIR) bands, at a resolution of 15 km per pixel. Vegetation appears in shades of red, exposed volcanic products in grey and water clouds in bright white. Panel B shows a decorrelation stretch (DCS) of thermal bands 14 (red), 12(green) and 11(blue), draped over a gray scale image of the brightness temperature in band 10 (see Figure 4.1 for a description of the bands). The temperature image is used to show the differences in temperature between the surface, which should appear in lighter shades, and that of the weather and eruptive clouds, which should appear in darker shades because they are travelling at an altitude of several kilometers and have much lower temperatures. Decorrelation stretches are used to emphasize subtle differences in multispectral data. In this case, it allows for the discrimination between various types of clouds and atmospheric gases. In the selected DCS, the absorption produced by SO_2 in a transparent plume should appear in yellow shades. Typical atmospheric clouds appear in very dark shades of green, while ash-laden volcanic clouds will appear in shades of purple. Note that variations in the composition of the surface can also be seen on the DCS. For example volcanic edifices, typically made of silicate materials and often covered in ash, also appear in shades of light pink. Finally panel C is a sketch map of the area. In those sketches, I isolated the volcanic edifice and isolated the volcanic plume areas using a simple vectorization algorithm based on the color values of the DCS. A

97

range of RGB values can be defined to represent the dark purple shades typical of ash clouds (or the yellow shades of an SO_2-bearing cloud) and polygons of that specific color can then be extracted from the image. This type of image allows us to identify regions of the drifting plumes with a spectral signature typical of volcanic products.
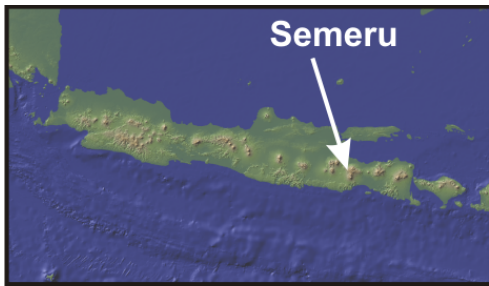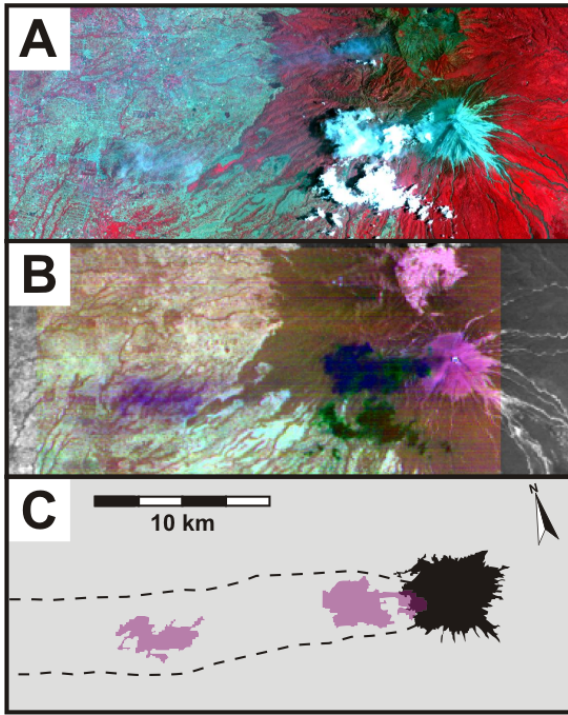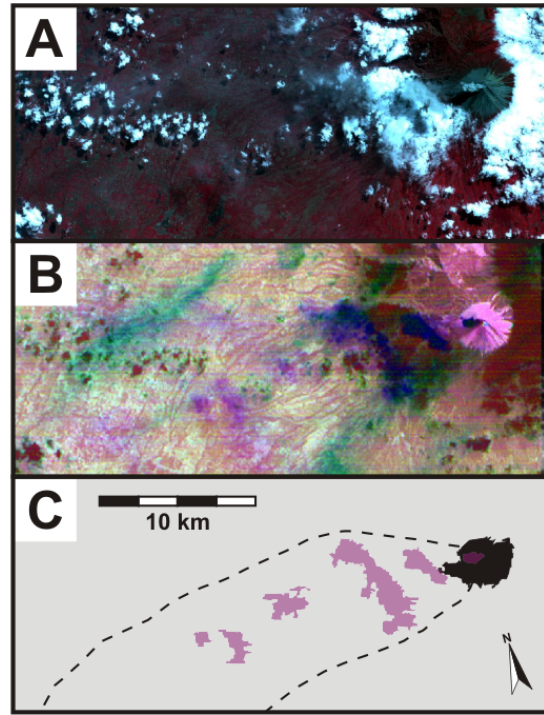
Figure 4.5: Subsets of two ASTER scenes taken over Semeru volcano on October 26, 2002 and August 12, 2004, respectively. A) Composite color image using the VNIR bands. B) Decorrelation stretch of thermal bands 14(R), 12(G) and 11(B) overlain on a gray scale image of brightness temperature in band 10. C) Sketch map of the target area. The purple outlines are extracted from image B using a color separation algorithm in order to emphasize detectable plumes.

Karimsky

Land

Volcanic center

Body of water

Volcanic plume
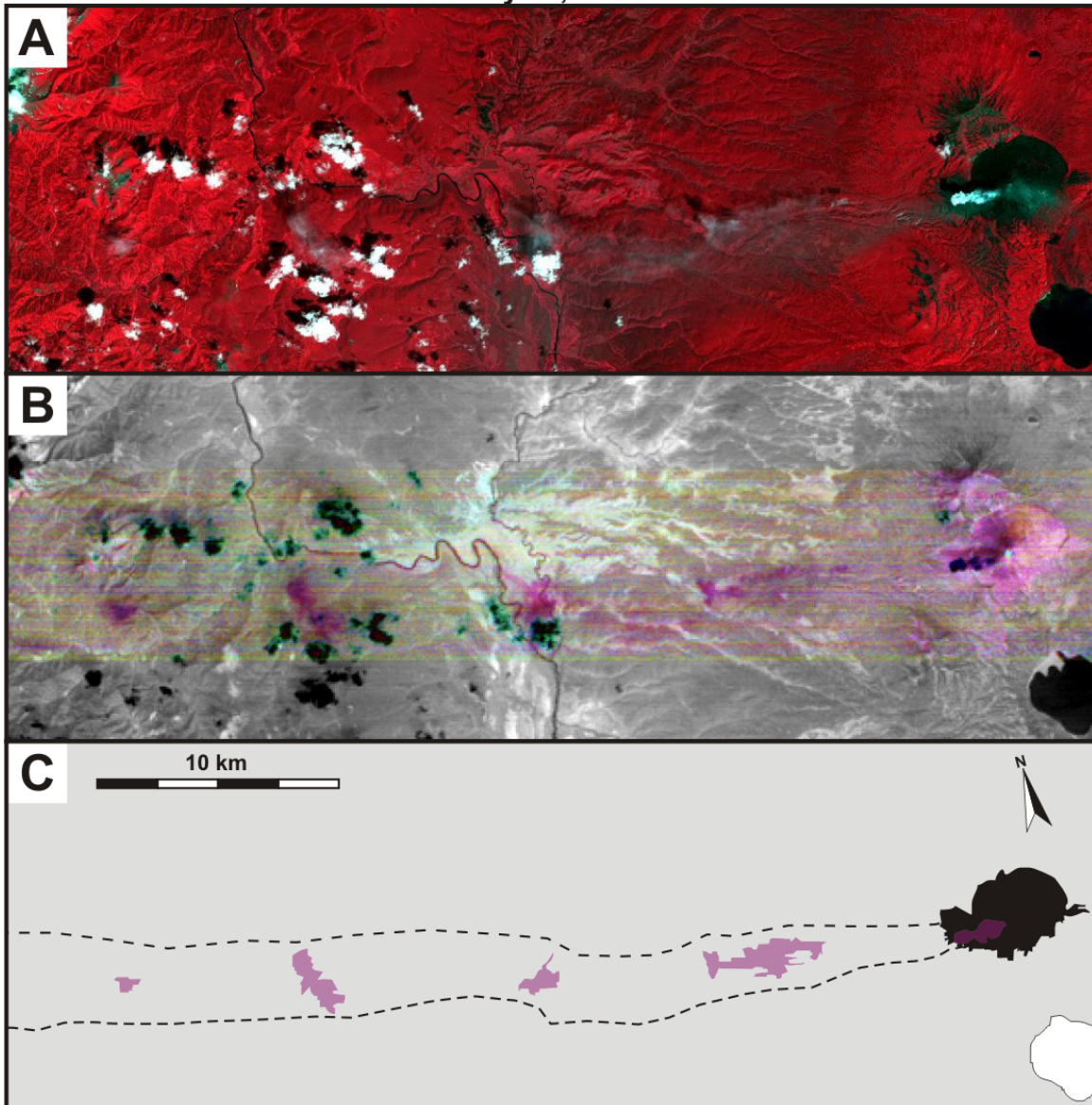
July 07, 2010

A

B

C

10 km

N

Figure 4.6A (previous page): Subset of an ASTER scene taken over Karymsky volcano on July 7, 2010. A) Composite color image using the VNIR bands. B) Decorrelation stretch of thermal bands 14(R), 12(G) and 11(B) draped over a gray scale image of brightness temperature in band 10. C) Sketch map of the target area. The purple outlines are extracted from image B using a color separation algorithm in order to emphasize detectable plumes.

Figure 4.6B: Subset of an ASTER scene taken over Karymsky volcano on October 12, 2010. A) Composite color image using the VNIR bands. B) Decorrelation stretch of thermal bands 14(R), 12(G) and 11(B) draped over a gray scale image of brightness temperature in band 10. C) Sketch map of the target area. The purple outlines are extracted from image B using a color separation algorithm in order to emphasize detectable plumes.

Land

Volcanic center

Body of water

Volcanic plume

February 15, 2006
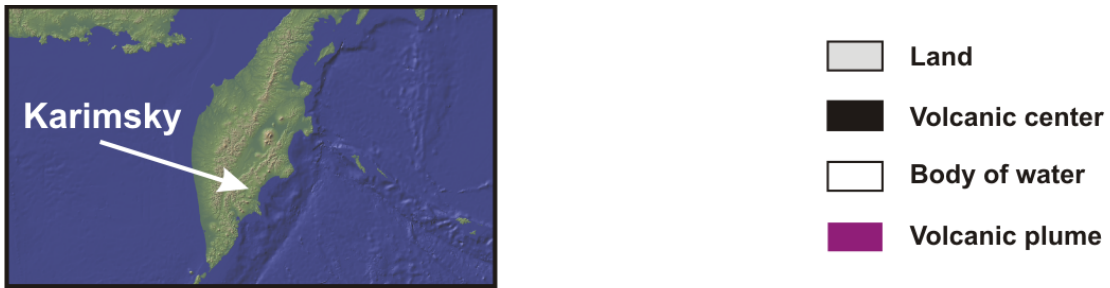

5 km

May 10, 2010

2 km
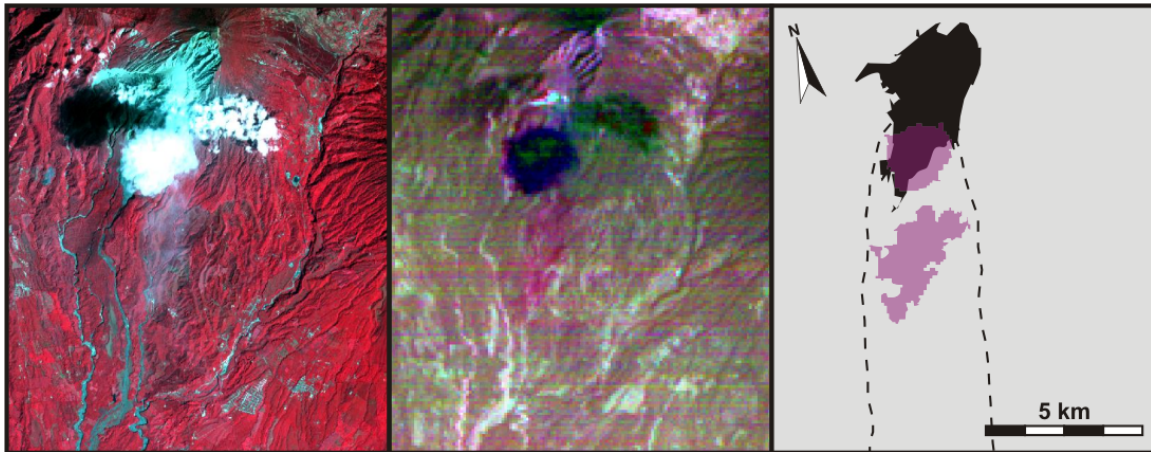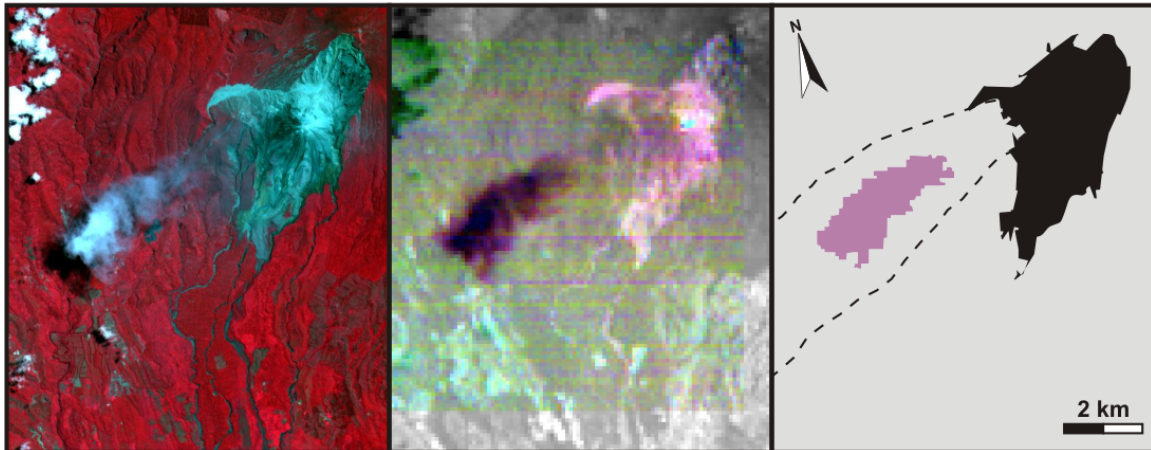
Figure 4.7 (previous page): Subset of two ASTER scenes taken over Santiaguito volcano on February 15, 2006 and May 10, 2010, respectively. A) Composite color image using the VNIR bands. B) Decorrelation stretch of thermal bands 14(R), 12(G) and 11(B) draped over a gray scale image of brightness temperature in band 10. C) Sketch map of the target area. The purple outlines are extracted from image B using a color separation algorithm in order to emphasize detectable plumes.

Land

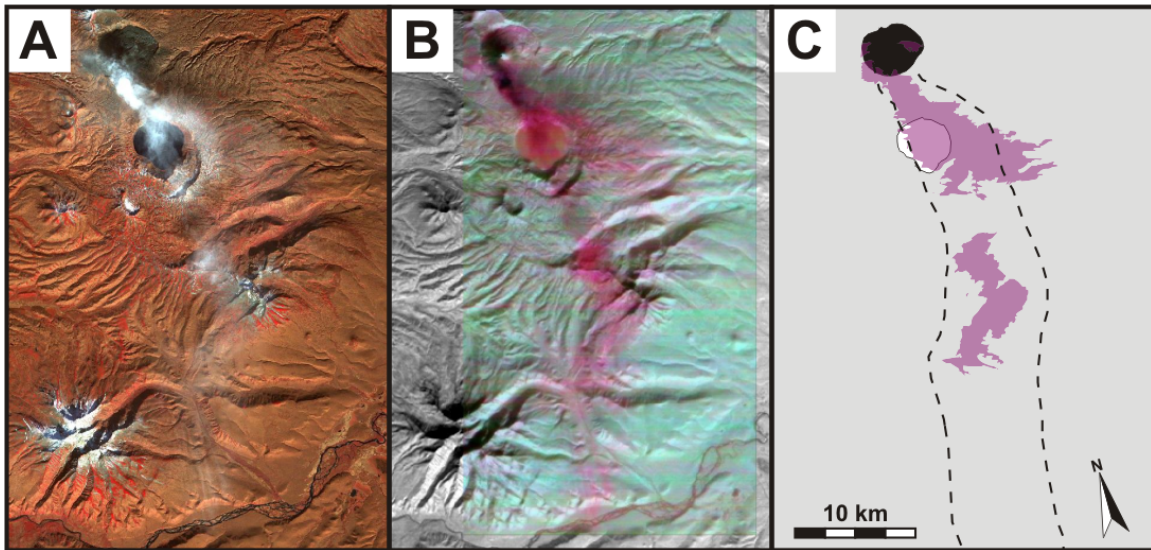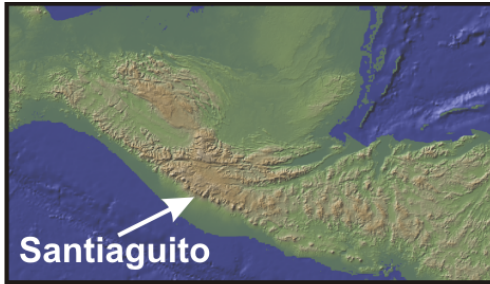**Volcanic center**

Body of water

Volcanic plume

Sakurajima

December 12, 2011

A B C 10 km

January 29, 2012

A B C 10 km
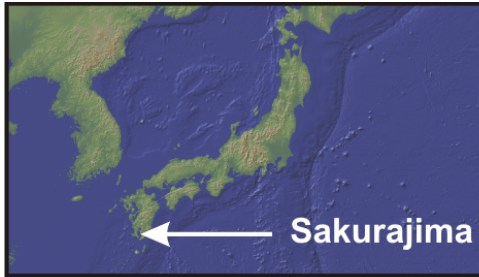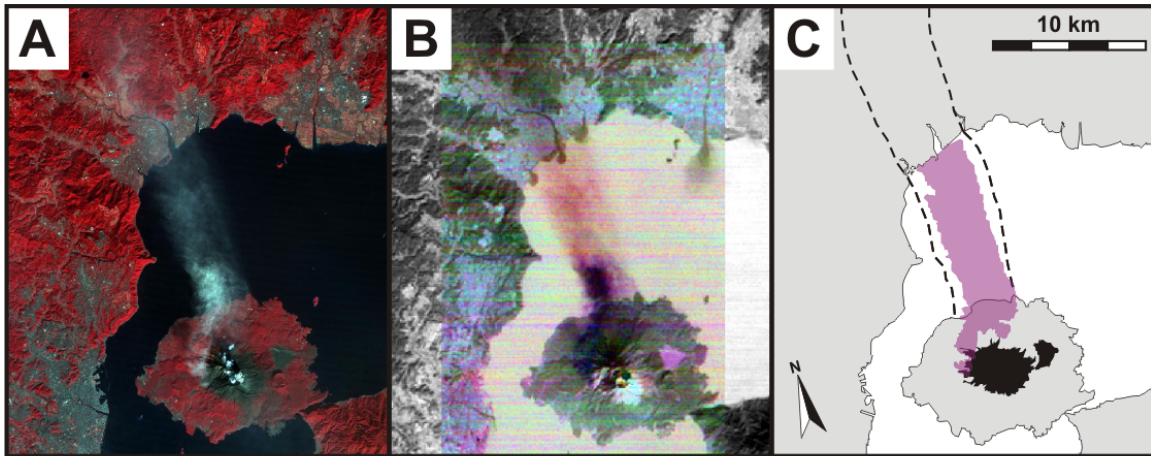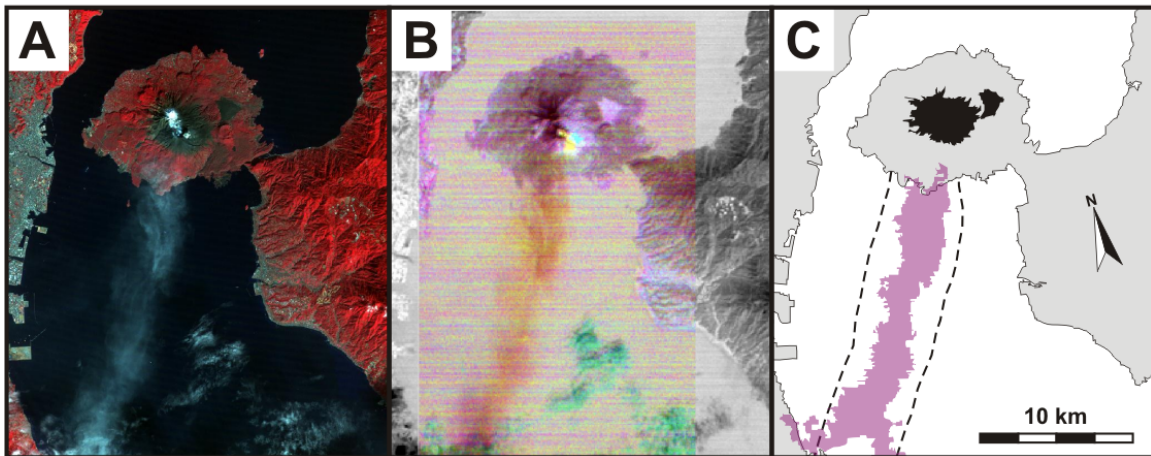
Figure 4.8 (previous page): Subset of two ASTER scenes taken over Sakurajima volcano on December 12, 2011 and January 29, 2012, respectively. A) Composite color image using the VNIR bands. B) Decorrelation stretch of thermal bands 14(R), 12(G) and 11(B) draped over a gray scale image of brightness temperature in band 10. C) Sketch map of the target area. The purple outlines are extracted from image B using a color separation algorithm in order to emphasize detectable plumes.

All images (Figures 4.5-4.8) clearly show the presence of volcanic ash plumes in the thermal bands. Semeru and Karymsky illustrate an activity style consisting of isolated pulses separated by several kilometers within a single image, suggesting repeated individual explosions separated by periods of little to no passive degassing. This eruption style is documented in Chapter 3 and Smekens et al. (2015) for the Semeru case, and has been interpreted to represent repeated plugging of the volcanic conduit by dense, degassed magma, which then allows pressure to build beneath it, ultimately leading to an explosion. Santiaguito is located at the edge of both scenes in figure 4.7, which could explain why only one pulse is visible in the images, indicating that plumes associated with previous pulses have already been carried downwind and out of the field of view. For Semeru, Karymsky, and Santiaguito, pulses generally become increasingly more difficult to identify in the DCS as the distance from the vent increases. This change is likely the result of the dilution of the plume as it entrains ambient air and is transported downwind. The areas of the plume between individual pulses show little to no distinctive signal in the thermal bands. The images of Sakurajima, on the other hand, seem to suggest more continuous degassing, though a concentrated area is visible in the image from 2011 that could be an explosion plume.

4.3.3 *Quantitative Retrieval of SO_2 Column Amounts and Emission Rates*

Though the plumes are clearly identifiable in the thermal images presented above, quantitative retrieval may not always be possible, depending on the amount of SO_2

present in the plumes (likely to be small in all cases) and the validity of the assumptions described in section 4.2.2 in each specific case. Decorrelation stretches are designed to enhance small variations between pixels in a prescribed area. The intensity and color of a pixel will vary depending on the nature of the other pixels considered and can never be used as a proxy for the amount of absorbing material present in the plume. The only way to retrieve quantitative information from the thermal images is to use the atmospheric modeling approach described in section 4.2.

Figure 4.9 shows the results of two retrievals a Semeru and Karymsky volcanoes using Plume Tracker. In each case, the height of the plume above local topography was determined from the visble images using the parts of the plume that are dense enough to produce shadows (2.9 km for Semeru, 1.9 km for Karymsky). The height is assumed to remain constant during plume transport and the shadow-derived values are used for retrievals on distal locations, where the plume is transparent and does not cast a shadow. A plume dense enough to cast a shadow likely has a very high optical thickness, potentially too high to allow for the retrieval of the gases contained within them. Indeed, in both cases represented in Figure 4.9, the proximal pulses were too dense to measure the SO_2 burden. No amount of SO_2 in the model, no matter how large, could account for the measured radiances, which were extremely low, suggesting that the sensor received only light emitted from the top of the plume (colder because it is at a higher altitude). Retrieval was impossible on the denser proximal clouds (denoted in the quantitative images by dark gray color). Similarly, the retrieval process yields no result for water

clouds when they are present in a scene. No water clouds are present in the image from Semeru, but some small clouds are visible in the distal area of the Karymsky scene. The opacity of volcanic plumes can be explained by the presence of absorbing materials such as ash, water droplets and aerosols, whereas the opacity of weather clouds is due solely to the presence of water ice or water droplets, depending on their altitude.

In order to account for changes in terrain underneath the plume, the retrieval was split into a number of juxtaposed zones. For each zone, a different emissivity profile was defined, taken from an area outside the plume. Further downwind, no clear signal is present at the expected locations for the more distant pulses (white outlines). In fact, the only variations detectable above the background seem to correspond to topographic changes or variations in the nature of the surface (creek beds, changes from forest to exposed rock outcrops, etc.). These two examples are representative of all retrievals attempted on the ASTER scenes for Semeru, Karymsky and Santiaguito.
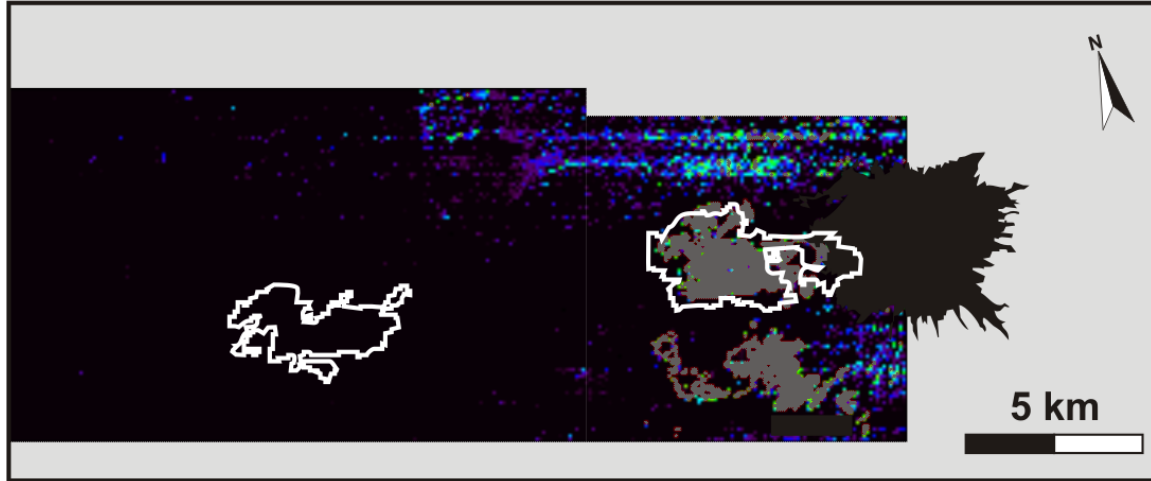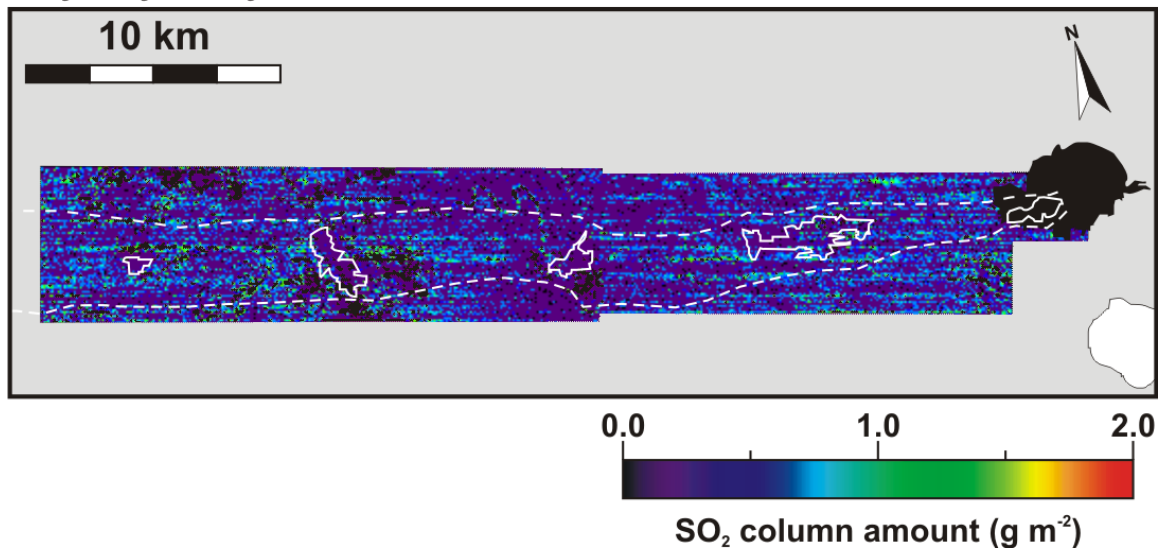
Figure 4.9: Results of two retrievals at Semeru and Karymsky volcanoes. Plumes were divided into separate portions when the nature or elevation of the surface behind them changed. For each section, a different emissivity profile was defined using an area adjacent to the plume. White outlines define the individual pulse identified with the DCS images. Dark grey shades in the quantitative image indicate areas where the plume is optically opaque and the software could not determine SO_2 load.

Figure 4.10 presents the results of a retrieval for Sakurajima volcano. Similarly to the examples above, plume height was calculated to be 1.9 km using the shadows of the more opaque part of the plume in the visble image. Once again dense parts of the eruptive clouds presented some difficulty and no SO_2 could be retrieved in the areas proximal to the vent. In the images, the plume is traveling over water, which facilitates the interpretation because variations in the emissivity are not expected to be significant in a body of water. Note, however, that the areas at the mouths of several rivers in the North of the bay show seemingly higher SO_2 burden. Those zones of apparently higher SO_2 burden can be attributed to the presence of high sediment load in the water and are not meaningful in this case. Outside of those small areas close to the coast, the plume is clearly distinguishable over the bay. The right panel of the figure presents five transects taken from the quantitative image (A-E). Note that the backgound value outside of the presumed plume is non-zero, and that the SO_2 amounts within the plume are only slightly higher than that background value. From those transects emission rates can be calculated using an estimate of the wind speed. Meteoroligical records at the Kagoshima airport report a wind speed of 2.2 m s^{-1} at the time of measurement (http://www.wunderground.com/history/). They also show that this value remains constant for a period of 6-8h, which gives us confidence in assuming that this value represents the plume transport speed. With that value, I calculated emission rates for each transect. They range from 2 to 3 kg s-^{1}. These values are on the same order of magnitude as the emission rates measured for the Minemidake crater (1-6 kg s^{-1}) by Kazahaya et al. (2013) in 2010.
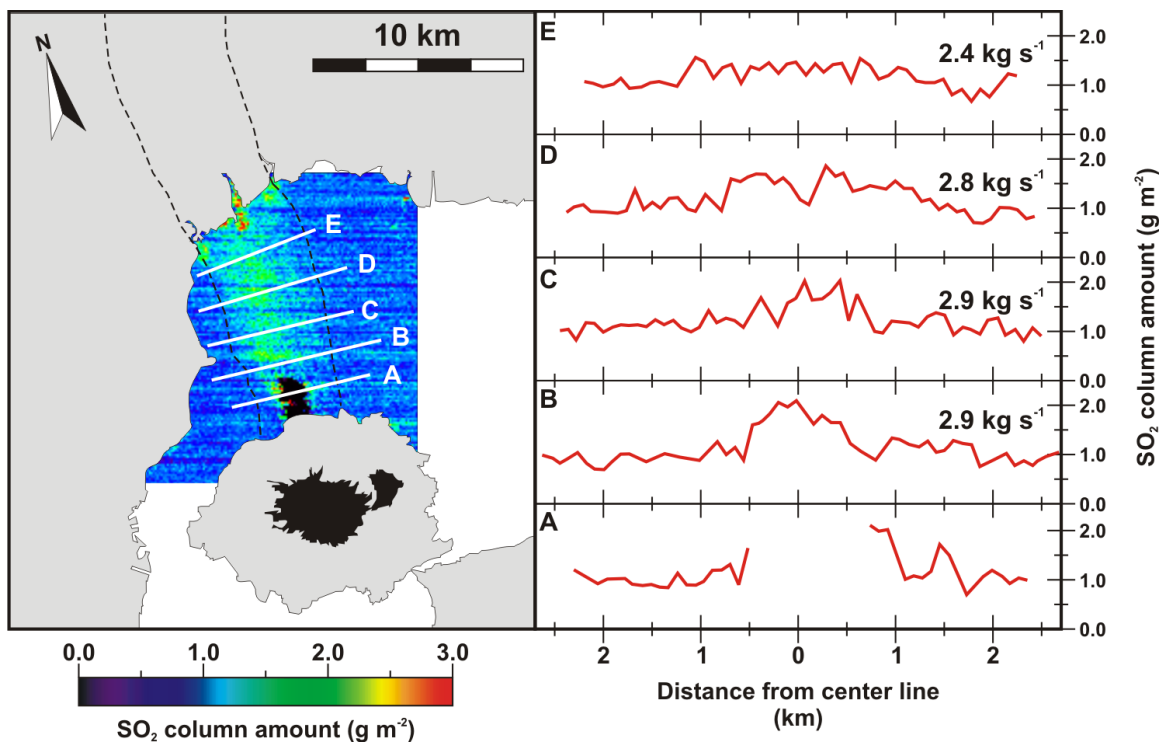
Figure 4.10: Results of the SO$_2$ retrieval on the drifting plume from Sakurajima on December 12, 2011, using Plume Tracker (methodology described in section 4.2.1). Ground emissivity profile was taken from an area of the bay immediately outside of the plume zone. Measured plume height: 1.9 km, assumed plume thickness 0.5 km. The black shaded zones on the colored image delimit an area where the plume is optically opaque and the software could not determine SO$_2$ load. On the right panel 5 profiles (A-E) are extracted from the SO$_2$ image. The equivalent emission rates are presented for each profile assuming a wind velocity of 2.2 m s^{-1}. Note how the plume starts to blend into the surrounding atmosphere as distance from the vent increases.

112

4.4 Discussion

Qualitative analysis of the images suggests that the eruptive plumes are detectable using ASTER, and that their spectral characteristics are consistent with the presence of SO_2; namely, a decreased radiance in band 11 relative to the other bands. The activity I am considering here often produces plumes with a significant amount of ash. This fact poses a problem when attempting to retrieve SO_2 emission rates. Images often show more than one isolated pulse in the eruptive plumes. The proximal pulses are laden with enough ash to render the plume completely opaque in the TIR, thereby making quantification impossible, even if I were able to account for the effect of ash. Unfortunately the available bands in ASTER do not allow for a correction for the presence of ash in the plume in a quantitative manner. The effect of ash must, however, be considered when interpreting the emission rates calculated for Sakurajima on the part of the plume that was not opaque (Figure 4.10). Because there is no method for accounting for ash or other particulates (sulfate aerosols for example) in ASTER images, the calculated emission rates presented here must be taken as upper limits.

The captured pulses become more and more transparent as distance from the vent increases. A fraction of the ash is removed very rapidly through ashfall; the remaining fine fraction is then distributed over increasingly larger volumes as the plume expands and entrains ambient air. This dilution should allow for an easier quantification of SO_2.

113

However, I was unable to detect any measurable SO_2 in the more distal pulses, suggesting that the concentrations were below the detection limit of the method.

In transect B at Sakurajma (Figure 4.10), column amounts within the plume are almost twice the background value. With downwind distance (along the plume axis), the plume becomes wider and more difficult to discern from the background as distance from the vent increases. These observations are consistent with the dilution of the plume as it expands into the atmosphere. Moreover, entrainment of ambient atmosphere into the drifting plume should also lead to a similar effect: reducing the concentration of SO_2 at any given point in the plume. Similarly I observe a decrease of the emission rate as distance from the vent increases. This phenomenon has been recognized and studied extensively in anthropogenic plumes. In a review of the processes that lead to this conversion, Eatough et al. (1994) found that the conversion rate could vary from < 1 % of available SO_2 converted per hour to over 10% per hour at high temperatures and relative humidity. The rate of conversion in a volcanic plume depends on other factors, as the plumes can be dynamic, and entrainment can affect the edges and the center of the plume differently, accelerating the conversion rate in some parts of the plume. Moreover, the chemistry of a volcanic plume presents a different chemical environment that could affect the kinetics of the oxidation reactions at play. Depletion effects have been recognized and quantified with much lower accuracy in volcanic plumes (e.g., Oppenheimer et al., 1998; Rodriguez et al., 2008), with values ranging from 10^{-3} to 10^{-7} s^{-1}. The process was coined as "SO_2 depletion" or "SO_2 loss". All indications suggest that it is likely to be faster in

114

the lower troposphere and in particular if the plume remains within the boundary layer (altitude < 2 km, depending on specific conditions). My own observations in the UV (Chapter 2) suggest that this effect could be affecting small plumes significantly over very short distances (< 1 km). The observed decrease between profiles B and E corresponds to a depletion rate of 4×10^{-4} s^{-1}.

Whether the process is physical dilution or chemical transformation, the concentration of SO_2 per pixel decreases with time spent in the atmosphere or in the case of the snapshot images above (Figure 4.5-4.8), with distance from the source. In my images, this effect leads to the effective blending of the plume edges into the background, and eventually to its complete disappearance. The detection limit on the Sakurajima image is ~0.9 g m^{-2}, corresponding to the average value measured in an area of the bay not affected by the plume (not shown on the figure). This value differs from one scene to the next and depends on the height of the plume considered and the temperature contrast between the plume and the background. In general, the detection limit for lower plumes will be larger. Since initial concentrations are expected to be lower in the case of the other three volcanoes, and the detection limit is likely to be larger given the variable nature of the ground underneath, dilution and/or SO_2 loss could explain why I was unable to measure SO_2 at Semeru or Karymsky in the more distal pulses.

Let us consider the amount of SO_2 released by the largest burst measured during my field campaign (~1460 kg, see Chapter 3) and distribute it over a relatively small area

115

of 20x10 ASTER pixels (note that the sizes of most pulses identified in my images aside from the most proximal ones are at least as big as this area). Assuming a homogeneous distribution, the resulting column amounts are ~0.5 g m^{-2}, a value that is below the detection limit for ASTER measured at Sakurajima. Even with a much smaller area of 10x10 pixels, the column amount on an individual pixel would be of ~1.6 g m^{-2}. Assuming a depletion rate similar to the one measured at Sakurajima, that value would decrease below the detection threshold in just over 45 mins. Depending on the wind speed, this could represent a distance of 4-17 km (computed from the range of velocities measured during our SO$_2$ camera campaign: 1.6-6.0 m s^{-1}).

4.5 Concluding Remarks and Recommendations

While satellite instruments provide synoptic views of entire volcanic plumes and offer access to remote areas of the world, their temporal resolution means that regular space-borne monitoring at a frequency comparable to ground-based measurements is impossible. I have shown here that, although detection and qualitative characterization is possible, limited spatial or spectral resolution prevents the quantification of SO$_2$ in eruptions of lower magnitude. A more regular schedule for acquisition of ASTER data would greatly increase the possibility of quantifying emissions from persistently active explosive volcanoes. In order to lower the detection limit of the method, additional data products are also needed, such as high-resolution DEMs (at least 90 m/pixel) and emissivity maps of the target areas, extracted from images with no plumes. The DEMs

116

could easily be produced using a pair of nadir and off-nadir images (bands 3 and 3N) of ASTER. But the emissivity maps would be much more challenging. They would have to be produced at regular time intervals in order to account for changes in vegetation, and using images with minimal cloud cover. The validity of such maps from one year to the next would also be called into question. And even with these additional datasets, there is no guarantee that the retrieval of the SO_2 mass would be possible. With the current technology and available data, quantification of SO_2 emissions at the majority of persistently active explosive volcanoes will remain challenging at best.

New instruments are in development that could provide alternative solutions. HyspIRI (http://hyspiri.jpl.gov/) is a project for a satellite with two instruments intended to replace ASTER after its decommission. The TIR imager will offer 7 bands in the TIR with a spatial resolution of 60 m/pixel. The distribution of the spectral channels is very similar to that of ASTER but the instrument will offer a band centered around the 7.3 μm feature of SO_2 and one centered at 12 μm. These new bands would offer the possibility of quantifying ash emissions as well as SO_2 emissions. Combined with the increased spatial resolution, these specifications may be enough to lower the detection limit on the method used in this chapter and allow for the quantification of emissions of both ash and SO_2 from the target volcanoes. In addition the instrument will offer a return period of 5 days.

However, the specifications of HyspIRI are not extremely dissimilar to those of ASTER, and it offers no guarantee that the new instrument will be successful at detecting

small plumes in the troposphere. Instead I would suggest a custom instrument that would utilize the same principles as the SO_2 camera described earlier, with two channels in the UV spectrum. Such an instrument would not offer the accuracy of a hyperspectral retrieval such as that offered by OMI. But a multispectral instrument in the UV would allow for increased spatial resolution with the use of narrow field of view optics. The sensitivity of SO_2 cameras decreases with distance from the source (Kern et al., 2013). This phenomenon is related to the fact that light diffracted by the atmosphere between the plume and the instrument dilutes the absorption signal. This dilution is a function of the distance to the target, but more importantly, of the density of the atmosphere. For example, the effect is not as strong at high altitudes, where the atmosphere is less dense. For that reason, orbiting instruments may not be affected as strongly, even though they are imaging the plume from a much greater distance, because the density of the atmosphere on top of the plume rapidly decreases. The technology is readily available to create a simple and compact dual imager, which could fit on a small satellite. Constellations of small satellites are becoming ubiquitous, lowering the cost of launching imaging instruments into orbits (e.g. CUBESATS). Having multiple SO_2 cameras with high spatial resolution in orbit at the same time, even for a limited amount of time, would increase the likelihood of detecting and quantifying emissions from a number of persistently active explosive volcanoes, and with it our ability to quantify their emissions in a more comprehensive manner.

CHAPTER 5

ERUPTION CYCLES IN A BASALTIC ANDESITE SYSTEM: INSIGHTS FROM

NUMERCAL MODELING

Characteristic repose intervals associated with eruption cycles at persistently

active explosive volcanoes vary from minutes to years. Numerical models of magma

ascent can provide great insight into the parameters that control dome-building eruptions

and their cyclicity (e.g., Melnik and Sparks, 1999). Such models have been used to study

eruption cycles with frequencies of months to decades (e.g., Barmin et al., 2002; Costa et

al., 2007b), and more recently, those with shorter cycles of minutes to days (e.g., Costa et

al., 2013; de' Michieli Vitturi et al., 2013). These studies have typically focused on the

reproduction of cycles observed for well-documented eruptions, such as the ongoing

eruption of the Soufrière Hills volcano (SHV), on the island of Montserrat. In the SHV

case, the eruptive products are andesitic with ~45 vol. % phenocrysts and the

composition of the glass phase, which represents the melt phase during magma ascent, is

a rhyolite (Barclay et al., 1998). Simple relationships exist to describe the rheology of

rhyolitic melts as a function of dissolved volatile content and temperature (e.g., Hess and

Dingwell, 1996). However, many periodic systems with sub-daily cycles, such as Semeru

(Indonesia), Karymsky (Russia), and Sakurajima (Japan) volcanoes, for example, are

more mafic (Carn and Pyle, 2001) and all indications suggest that the melt phase is not a

rhyolite. Contrary to rhyolite melts, the viscosities of andesite or basaltic andesite

magmas are strongly dependent upon the specific composition of the melt. In response to this strong dependence, Giordano et al. (2008) have developed a relationship that can be used to calculate the viscosity of a melt as a function of its chemical composition (expressed as mass fractions of major oxides), its temperature and its dissolved water content. Differences of several orders of magnitude are observed for relatively small changes in oxide composition, especially in the intermediate range of compositions from basaltic andesite to andesite.

In this chapter, I use solutions from a numerical model, constrained by petrologic data and field observations, to explore the conditions that lead to the existence of and control the characteristic timescales of repose associated with cyclic eruptive activity in basaltic andesite systems. In order to conduct this study, I modified an existing model, originally developed by de' Michieli Vitturi et al. (2013), to include the Giordano et al. (2008) relationship for compositionally dependent melt viscosity. The existence of a viscous plug at the top of a volcanic conduit, whose strength is periodically overcome by the pressure created by the degassing of the ascending magma, is often invoked to explain the existence of cycles in systems of intermediate to silicic composition (e.g, Holland et al., 2011; Iguchi et al., 2008; Johnson et al., 1998; Morrissey et al., 2008; Ruiz et al., 2006). Here, I explore the conditions that lead to the formation of such a plug, and examine the details of plug formation and destruction, and their role in controlling the magnitude and frequency of eruptive cycles.

120

5.1 The Magma Ascent Model

DOMEFLOW is a 1-D axisymmetric transient conduit model described in detail in de' Michieli Vitturi et al. (2010), and originally developed to study the transient effects of magma ascent in the SHV system. The model considers the vertical flow of two separate phases each with their own velocity: a magma phase (accounting for the presence of melt and crystals) and a gas phase consisting of water vapor. The mixture is treated as a bubbly flow, in which the melt is a liquid continuum with dispersed bubbles and crystals in thermodynamic and mechanical equilibrium (Jaupart and Allègre, 1991; Melnik and Sparks, 1999), and the effects of bubbles and crystals on mixture viscosity are included (Llewellin and Manga 2005; Costa 2005). A single pressure (P) is attributed to the mixture, following the assumption that the ascent is slow enough to allow for the equilibration of pressure between the two phases (Sparks, 1978), and the system is isothermal. During all runs presented here the pressure at the bottom of the conduit (P_{bot}) and at the top of the conduit (P_{top}) remain fixed in time, although these pressure boundary conditions may vary from run to run. As the magma ascends and the pressure drops, water exsolves from the melt and additional crystals form. Crystal and dissolved volatile contents are described as functions of P only.

Conservation of mass is defined separately for each phase. Conservation of mass for the gas phase is

$$\frac{\partial}{\partial t}\left[\pi R^2\left(\tilde{\rho}_g\right)\right] + \frac{\partial}{\partial z}\left[\pi R^2\left(\widetilde{\rho V}_g\right)\right] = -2\pi R Q_{lat} \tag{5.1}$$
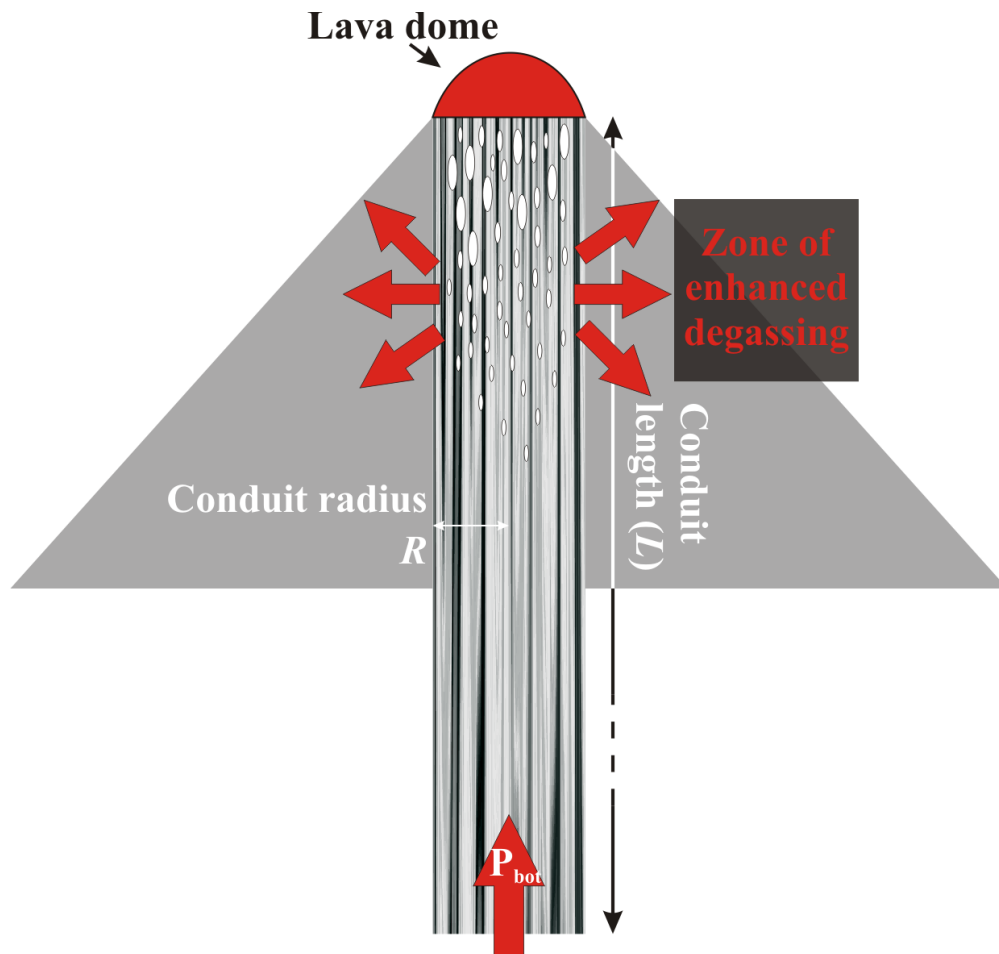
Figure 5.1: Schematic representation of the conduit geometry. L is the length of the conduit from the base of the dome to the magma chamber. R is the conduit radius. The existence of a lava dome at the outlet of the conduit can be considered by adjusting the top boundary condition. In the runs presented here, boundary conditions are set so that the pressure at both end of the conduit (P_{top} and P_{bot}) remain constant in time. A zone of enhanced or lateral degassing at the top of the conduit creates a viscous plug that inhibits the flow of magma.

Description	Symbol	Value
Boundary conditions		
Pressure at the bottom of the conduit	P_{bot}	115-125 MPa
Pressure of the dome (weight of the dome)	P_{dome}	1 MPa
Atmospheric pressure	P_{atm}	101300 Pa
Initial dissolved gas mass fraction	x_{d_tot}	2.5-5.0 %
Initial crystal volume fraction	β_{min}	30-60 %
Constants		
Temperature	T	1200-1250 K
Conduit length	L	5000 m
Conduit radius	R	5-25 m
Density of the melt	ρ_m	2300 kg m^{-3}
Density of the crystals	ρ_c	2700 kg m^{-3}
Density of the country rock	ρ_{cr}	2600 kg m^{-3}
Density of the dome	ρ_{dome}	2250 kg m^{-3}
Viscosity of the gas	μ_g	1.5x10^{-5} Pa s
Gravitational acceleration	g	9.81 m s^{-1}
Water solubility	s	4.11x10^{-6}
Calculated variables (for all control volumes along the z-axis)		
Pressure	P	
Exsolved gas volume fraction	α	
Crystal volume faction	β	
Density of the mixture	ρ_{mix}	
Viscosity of the liquid	μ_m	
Viscosity of the mixture	μ_{mix}	
Velocity of the gas	V_g	
Velocity of the mixture	V_{mix}	
Mass flow rate	Q	

Table 5.1: Model parameters

In equation 5.1, R is the conduit radius, ρ_g is the density of the gas phase, V is the velocity of the gas phase, t is time, and z is the vertical coordinate. The right-hand side is a sink term expressing the loss of volatiles due to enhanced permeability through the country rock, which is defined as follows:

$$Q_{lat} = \frac{\rho_g \alpha k_{cr}(P - P_{lith})}{\mu_g R} \tag{5.2}$$

where α is the volumetric gas fraction, ρ_g is the density of the gas, μ_g is the viscosity of the gas (constant at 10^{-5} Pa s), and k_{cr} is the permeability of the country rock. The value of this latter parameter can vary over a range that covers several orders of magnitude between 10^{-14} and 10^{-11} (Jaupart and Allègre, 1991).

The two terms on the left hand side in equation 5.1 represent the temporal variations in the bulk density of the gas ($\tilde{\rho}_g$) and the variations in the vertical gas flux per unit area ($\widetilde{\rho V_g}$), both quite sensitive to changes in pressure and the exsolution of the volatiles and driven by forces described in the momentum equation below.

The bulk density of the gas is defined as

$$\tilde{\rho}_g = \alpha \rho_g + [(1 - \alpha)(1 - \beta)x_d]\rho_m \tag{5.3}$$

The vertical flux of gas per unit area is defined as

$$\widetilde{\rho V_g} = \alpha \rho_g V_g + [(1-\alpha)(1-\beta)x_d]\rho_m V_{mix} \tag{5.4}$$

In equations 5.3 and 5.4, β is the volumetric crystal fraction (relative to the bubble-free magma), ρ_m is the density of the melt, and x_d is the mass concentration of the dissolved gas relative to the crystal- and bubble-free magma. The density of the gas is calculated by treating water vapor as an ideal gas. The concentration of the dissolved gas is calculated as a function of pressure as defined by Henry's law: $x_d = s\sqrt{P}$ where $s = 4.11\text{x}10^{-6}\,\text{Pa}^{-1/2}$. Groundmass crystallinity increases as the magma ascends, following a relationship established using experiments on synthetic melts (Clarke et al., 2007; Couch et al., 2003):

$$\beta = min\left[\beta_{max}; \beta_0 + 0.55\left(0.58815\left(\frac{P}{10^6}\right)^{-0.5226}\right)\right] \tag{5.5}$$

Conservation of mass for the magma is

$$\frac{\partial}{\partial t}[\pi R^2(\tilde{\rho}_{mix})] + \frac{\partial}{\partial z}[\pi R^2(\widetilde{\rho V}_{mix})] = 0 \tag{5.6}$$

where $\tilde{\rho}_{mix}$ is the bulk density of the mixture and $\widetilde{\rho V}_{mix}$ the vertical mass flux of the mixture per unit area. The mixture, as stated above, consists of liquid melt, crystals, and bubbles, and its density and mass flux are defined as

$$\tilde{\rho}_{mix} = (1 - \alpha)[\beta\rho_c + (1 - \beta)(1 - x_d)\rho_m] \tag{5.7}$$

$$\widetilde{\rho V}_{mix} = (1 - \alpha)[\beta\rho_c + (1 - \beta)(1 - x_d)\rho_m]V_{mix} \tag{5.8}$$

A single equation describes the conservation of momentum for the complete mixture (liquid melt, crystals, bubbles, and gas contained in the bubbles):

$$\frac{\partial}{\partial t}\left[\pi R^2\left(\widetilde{\rho V}_g + \widetilde{\rho V}_{mix}\right)\right] + \frac{\partial}{\partial z}\left[\pi R^2\left(\widetilde{\rho V^2}_g + \widetilde{\rho V^2}_{mix}\right)\right] \tag{5.9}$$

$$= -\frac{\partial P}{\partial z} - \rho_{mix}g - \frac{8\mu_{mix}R}{R^2}V_{mix}$$

where g is gravitational acceleration. The transient changes in mixture momentum (first term on the left-hand side) and the net flux of momentum along the conduit (second term on the left hand side) are balanced by the vector sum of all forces acting on the system (right-hand side of the equation). The forces are made up of the pressure gradient (first term RHS), gravitational forces (second term RHS), and viscous forces (third term RHS). The viscous forces acting on the system are approximated using a modified Poiseuille term.

Finally, the velocities of the two phases (V_g and V_{mix}) can be related to each other as a function of the pressure gradient, assuming Darcian flow through a porous medium

consisting of an interconnected network of bubbles rising at the same velocity as the mixture:

$$V_g - V_{mag} = -\frac{k(k_0, \alpha)}{\mu_g}\frac{dP}{dZ} \qquad (5.10)$$

In eq. 5.10, the vertical permeability of the exsolved gas k (m^2) is a function of a reference permeability (k_0) and the exsolved gas volume fraction α (Melnik and Sparks, 2002; Melnik and Sparks, 1999):

$$log\left[\frac{k(\alpha)}{k_0}\right] = -10.2(\alpha \cdot 10^2)^{1.4 \times 10^{-2}\alpha^{-1}} \qquad (5.11)$$

5.2 Constraining the Rheology of a Basaltic Andesite

The model described above has been used to replicate the observed periodic cycles of extrusion and gas emissions at SHV with characteristic periods of 8 − 12 hours (de' Michieli Vitturi et al., 2013). I have made one major modification to the model, pertaining to the viscosity of the melt. The original model for SHV assumed a rhyolitic composition of the melt phase. In that case, the viscosity of the melt (μ_m) can be calculated as a function of dissolved water content and temperature using the equation developed by Hess and Dingwell (1996) for leucogranitic melts. However, the bulk composition of eruptive products at Semeru (and at similar systems mentioned above) is significantly less silicic, lying clearly in the range of basaltic andesites (see Table 5.2).

127

Given the measured phenocryst content of Semeru eruptive products, the composition of the melt is therefore likely more mafic than a rhyolite. To account for this difference, we calculate the viscosity of the melt as a function of the various oxide fractions, dissolved water content, and temperature, using a relationship developed by Giordano et al. (2008). The viscosity of the melt can be expressed as

$$\log \mu_m = A + \frac{B}{T - C} \qquad (5.12)$$

where T is the temperature of the melt in Kelvin, and A, B and C are computed from the molar fractions of the various oxides (including dissolved water).

Figure 5.2 shows some examples of the viscosity of melts of various compositions spanning a range between rhyolite and basaltic andesite, calculated with the Giordano et al. (2008) model. The Giordano model shows good agreement with the Hess and Dingwell (1996) relationship for the rhyolitic composition. As the composition of the melt becomes more mafic, the calculated viscosity is reduced by several orders of magnitude, even for small changes in composition.
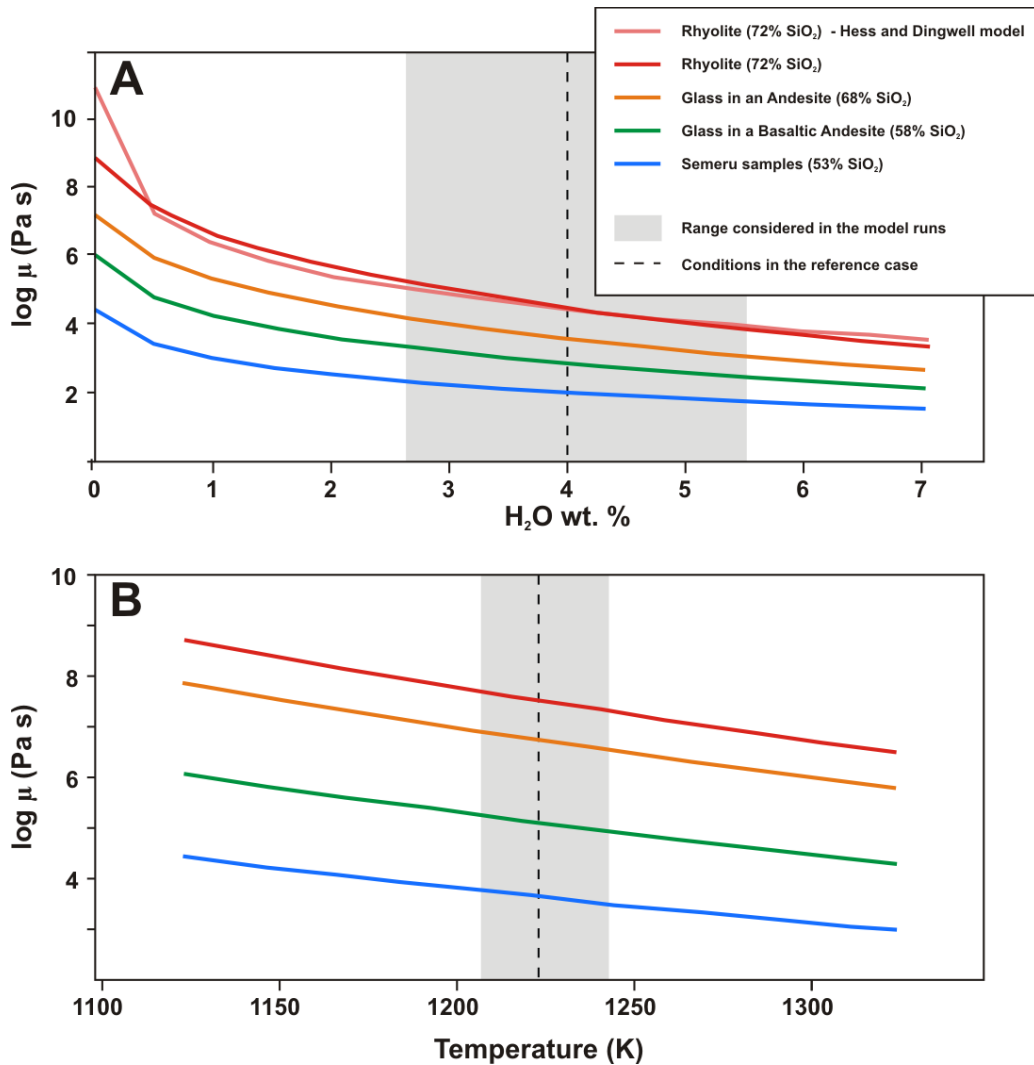
Figure 5.2: Viscosity of the considered compositions plotted against water content (A) and temperature (B). The viscosity dependencies are calculated using the model developed by Giordano et al. (2008), except for one example of a rhyolitic composition using the relationship of Hess and Dingwell (1996) for comparison in A. The range of temperatures and water contents considered in the model runs is highlighted in gray. The composition of the glasses plotted here are taken from Moore and Carmichael (1998) and listed in table 5.2.

Oxide mass fraction (wt. %)	Semeru samples			Basaltic andesite (Moore and Carmichael, 2008)		Andesite (Moore and Carmichael, 2008)	
	[1]From Carn and Pyle (2001)	Lava dome samples	Summit tephra samples	Bulk	Glass[2]	Bulk	Glass[2]
SiO_2	56.96	53.02	58.58	55.25	58.50	61.61	68.20
TiO_2	0.720	0.832	0.398	0.740	0.910	0.600	1.030
Al_2O_3	19.72	19.16	18.47	17.41	16.90	17.82	13.70
FeOt	6.94	8.82	7.38	5.98	5.03	4.85	3.16
MnO	0.177	0.183	0.155	-	-	-	-
MgO	2.3	3.49	1.69	6.68	2.80	2.54	1.20
CaO	8.04	8.57	8.43	7.28	5.35	5.70	3.20
Na_2O	3.60	3.14	3.37	3.97	2.20	4.77	4.20
K_2O	1.24	0.98	1.20	1.18	1.74	1.43	2.60
P_2O_5	0.177	0.164	0.154	0.270	-	0.200	-
Total	99.88	98.34	99.83	98.76	93.43	99.52	97.29

Table 5.2: Composition of the samples considered in this chapter. Bulk rock analysis done by XRF. Glass analysis was completed with electron microprobe analysis. Total iron expressed as ferric iron (FeOt). Semeru samples were collected during field campaigns: SL-0511-C is a piece of dome rock from a fresh lahar deposit; SE-130521 is lapilli size tephra collected at the summit. [1]Lava bomb sample from the summit of Semeru (Carn and Pyle, 2001). [2]Glass compositions are taken from high-pressure experiments (Moore and Carmichael, 1998) performed with the corresponding bulk composition: Glass in the basaltic andesite with 48% crystals at 607 bars (60 MPa); Glass in the andesite with 34% crystals at 441 bars (44 MPa).

In order to constrain the composition of a typical basaltic andesite, I collected samples at Semeru volcano in 2011 and 2013. The major oxide compositions were obtained by X-ray fluorescence (XRF) at the XRF laboratory at Washington State University. The results are presented in Table 5.2, along with other compositions considered in this section. The first set of samples were clasts from the volcanic dome that were carried down the main network of valleys to the Southeast of the volcano during block-and-ash flow events and subsequent lahars, and were sampled in a river bed approximately 15 km from the active dome. I believe them to represent the modern composition of the volcanic domes that grow in the crater. Very few data exist regarding the composition of the eruptive products at Semeru, but my samples are very similar to samples measured previously (Carn and Pyle, 2001) and can be taken to represent the bulk composition of typical Semeru lavas. I also sampled recent tephra products from the summit of the volcano, in the form of fine lapilli-sized fragments. Those samples show a more evolved composition. However, they may not represent the bulk composition of the lava, as large phenocrysts were virtually absent from the fine lapilli size fraction. Because of this sampling bias, they likely represent a composition closer to that of the melt fraction remaining after phenocryst formation at depth.

Aside from melt composition, two important factors affect the viscosity of the magmatic mixture represented in the model: the volume fraction of crystals (β) and the volume fraction of bubbles (α). Once the viscosity of the melt (μ_m) is computed using the

composition data and the dissolved water content (x_d), the viscosity of the mixture is given by:

$$\mu_{mix} = \mu_m \cdot \theta_1(\beta) \cdot \theta_2(\alpha) \tag{5.13}$$

θ_1 is a factor that increases the viscosity of the melt as a function of its crystal content using a relationship developed by Costa (2005):

$$\theta_1 = \left\{ 1 - c_1 \cdot erf \left(\frac{\sqrt{\pi}}{2} \beta \left[1 + \frac{c_2}{(1-\beta)^{c_3}} \right] \right) \right\}^{-B/c_1} \tag{5.14}$$

In this equation, $erf(x)$ is the error function (the integral of the Gaussian distribution, B is the Einstein constant, and c_1, c_2 and c_3 are adjustable parameters. θ_2 describes the changes in viscosity due to the presence of bubbles, following a generalization of Llewellin and Manga (2005) and Costa et al. (2007a) in the form:

$$\theta_2 = \omega_c(1-\alpha)^{-1} + (1-\omega_c)(1-\alpha)^{5/3} \tag{5.15}$$

where $\omega_C = 1/[(1 + 4Ca^{1.4})(1 + 4Cd^{1.4})]$ is an empirical factor yielding the best fit for a wide range of gas volume fractions.

In order to constrain a reasonable range of values for the crystal fraction, I examined thin sections of the samples described above (see Figure 5.3). I observed a

132

phenocryst assemblage composed of a large majority of plagioclase crystals, along with a smaller population of clinopyroxenes. The groundmass of all samples was filled with microcrystals, suggesting that they resided in a dome or in the upper portions of the conduit for extended periods of time. Using image analysis software and a threshold of 100 μm as the minimum size for a phenocryst, I calculated the relative area occupied by phenocrysts in a series of 50 different thin sections. I consider these values to serve as a proxy for the volumetric fraction of crystals present in the melt before ascent through from storage zone to the surface (β_{init}). This technique makes the assumption that all crystals smaller than the threshold were not present in the melt prior to ascent. This assumption may not hold for small crystals such as oxides or small olivines, which may have crystallized long before the ascent of the magma to the surface. However, these oxides and olivines represent a very small percentage of the total volume of crystals present in the samples (< 1 %) and will not significantly impact the viscosity of the magmatic mixture or the overall conclusions of this analysis. The same can be said for the effects of irregular crystal shapes, which could introduce errors when extrapolating from a relative area to a volume concentration. The samples analyzed showed a wide variety of crystal contents, ranging between 30 and 60 %. This is the range I considered in the model runs. Moore and Carmichael (1998) performed a series of high-pressure experiments using a starting composition of basaltic andesite similar to the bulk compositions measured in the samples from the Semeru dome. The crystal assemblage produced in those experiments is also very similar to what I observe in my samples. In order to approximate the composition of the glass in the Semeru lavas, I used the Moore

133

and Carmichael (1998) measured glass composition for a set of conditions that produced a high volume fraction of crystals (52 %). For reference, Table 5.2 also shows the bulk composition of an andesite from Colima, considered in the same study, and the resulting glass composition for conditions that lead to relatively high crystal content (34 %). The two glass compositions result in vastly different viscosities (see Figure 5.2).
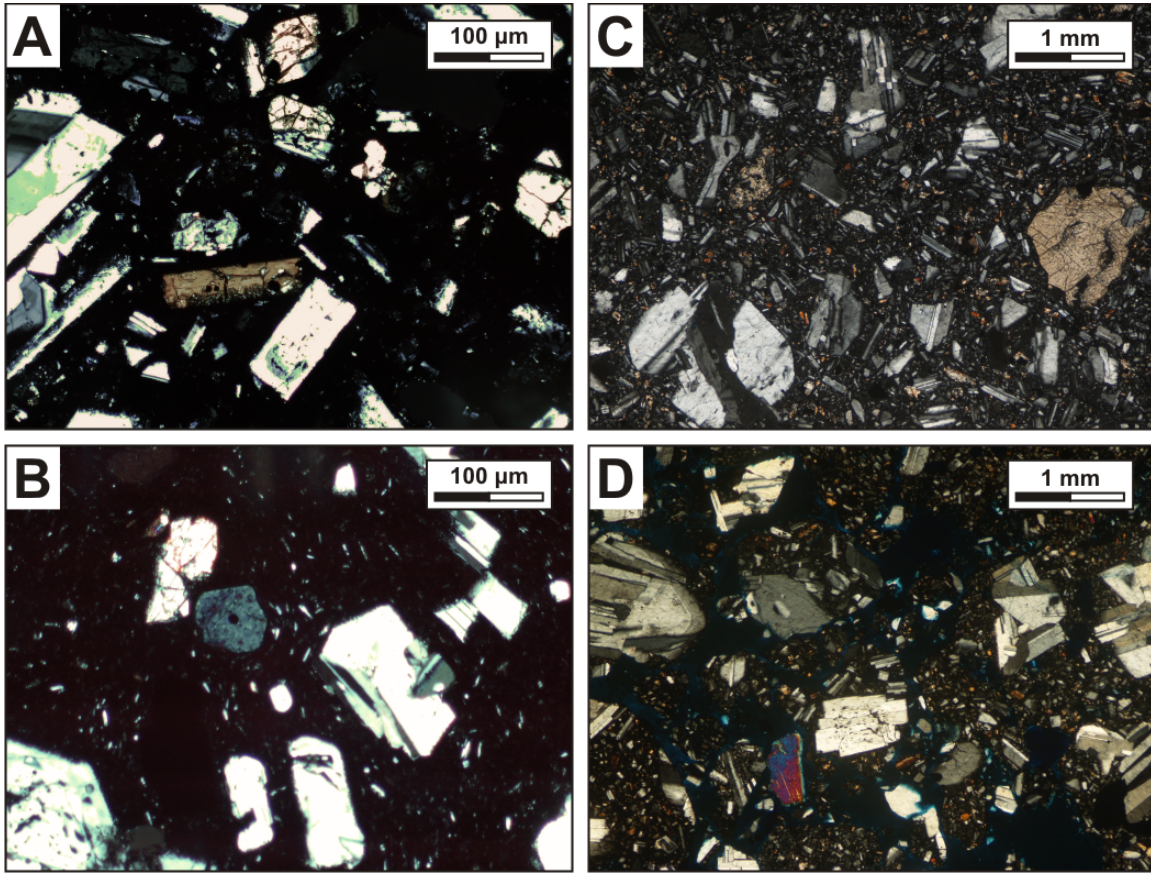
Figure 5.3: Photographs of thin sections of the samples collected at Semeru volcano in 2011 and 2013. The images were acquired under cross-polarized light using a petrographic microscope. A-B) Pieces of dome rock collected from a lahar in a valley Southeast of the volcano. C-D) Explosive tephra products collected at the summit of Semeru. C is a lava bomb; D represents the lapilli fraction. The phenocryst assemblage is similar in all samples, with a majority of plagioclase and occasional clinopyroxene. All samples also show extensive populations of microcrystals

5.3 Results

I performed several dozen runs at various conditions. Here I show only the results of runs that produced cyclic eruption activity. The range of values considered for the initial conditions in those runs are listed in Table 5.1. Water content in magmas of intermediate composition can range from 0 to 6 wt. % (Sisson and Layne, 1993; Wallace, 2005). However, I was not able to produce periodic behavior for initial water contents below 2.5 %. The range of crystal contents is derived from the thin sections analyzed above, between 30 and 60 %. The eruptive temperature of a magma depends on a range of factors including its composition and crystallization history. It can be difficult to measure directly, as a crust quickly forms around lava domes and flows, preventing the direct observation of the magma using radiometers, and contact measurement using a thermocouple presents obvious dangers. The best constraints on eruptive temperatures usually come from petrological experiments on phase equilibria. The temperatures considered in the experiments that produced the melt composition used in this study ranged from 950-1150 °C (Moore and Carmichael, 1998). However, high crystal contents such as the ones I observed in the Semeru samples are typically produced in experiments at the lower end of that temperature range. The range of temperature I considered in the model runs brackets this lower end range of values (927 - 977 °C; 1200-1250 K). Finally the geometry of the conduit was constrained by visual observations made of the dome in the crater at Semeru, in May of 2013. The dome at the time was approximately 50 m high, and a circular outline was visible at the top, with a radius of ~ 25m, which I took to

represent the absolute maximum value for the radius of the conduit. In all runs presented here, the pressure of the dome is kept constant at 1 MPa, corresponding to a dome height of ~ 45 m (assuming a density of 2250 kg m^{-3} for the dome).

Cyclic eruptions occur only for a narrow range of parameters. Figure 5.4 illustrates the various regimes produced by the model and their dependence on the assumed permeability of the country rock (k_{cr}). These regimes were generated for a single reference case with a fixed set of parameters (listed in the legend), by varying only the value of country rock permeability. For this reference case (and any single reference case), three separate regimes can develop, depending on the value of k_{cr}. As the magma approaches the top of the conduit, the solubility of water drops dramatically, and bubbles start to form in the mixture. The high viscosity of the mixture in this region creates an overpressure in the magma column, which tends to create a dramatic pressure drop from this region toward the surface and increases the ascent velocity of the liquid phase. For low values of k_{cr}, the exsolved gas cannot escape the mixture, and thus drives the column of magma upward, creating steady state effusion or explosion of a high vesicularity magma (regime 1). When k_{cr} is increased, a portion of the exsolved gas escapes from the ascending column of magma (open-system degassing) and causes the density of the mixture to increase due to bubble collapse, ultimately creating a dense, viscous plug that slows the flow of magma to the surface. In this regime (2) the associated effusion rates are smaller than those of regime 1. As k_{cr} is further increased, the density of the viscous plug also increases as more and more gas is allowed to leave the system. At some point,

at high values of k_{cr}, cyclic eruption behavior sets in (regime 3) and the effusion rate starts to oscillate between two values (the two blue lines Figure 5.4) as the plug is periodically extruded and created. For a given set of parameters, the value of the enhanced permeability does not strongly affect the frequency or magnitude of the resulting cyclic behavior (red line and difference between blue lines in Figure 5.4). As k_{cr} continues to increase, the density of the plug decreases to values close to the Dense Rock Equivalent (DRE). At that point, the viscous and gravitational forces of the plug overwhelm the driving pressure gradient and eruption is no longer possible.

The characteristic repose times of all cyclic solutions acquired here range from several minutes to 8h, and the associated flow rates at the top of the conduit vary between 1 and 2500 m^3 s^{-1}. When discussing the results below, flow rates are reported with two different values delimiting the amplitude of the oscillations. The lower value can be considered to be the baseline effusion rate in the dome-building eruption, while the higher value represents the peak in effusion rate or an explosion. Although DOMEFLOW does not simulate explosive eruption development, I interpret many of the peaks to represent explosive eruptions, because they exhibit very sharp pressure drops and subsequent extensive gas release as discussed below.
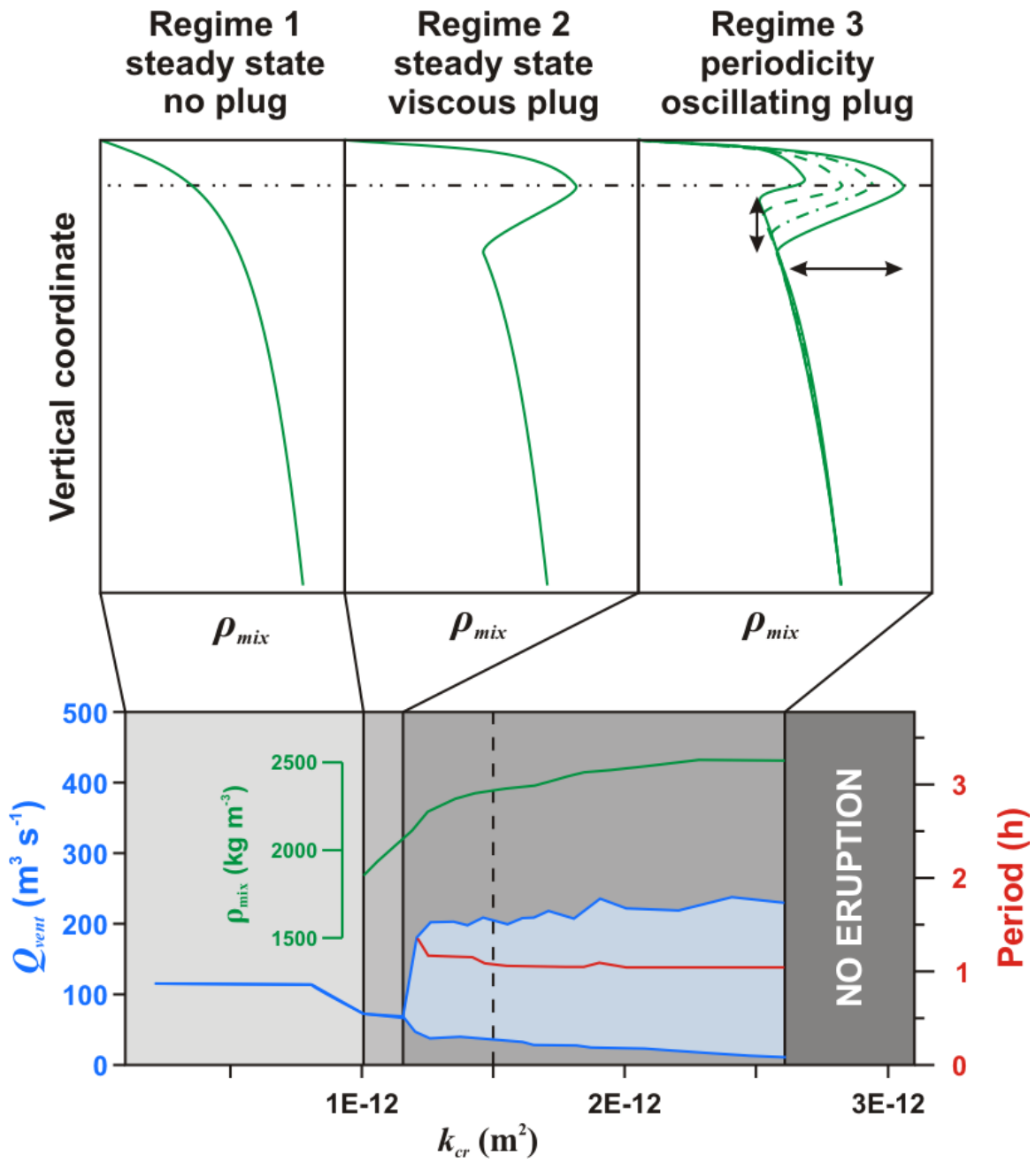
Figure 5.4 (previous page): Flow regimes produced by the model for a reference case with a set of initial conditions (see legend below). The density of the mixture as it varies vertically is plotted schematically for each regime. Regime 1 is the steady extrusion, with a magma monotonically decreasing in density as it ascends. Regime 2 is also a steady state solution but with the existence of a dense plug at the top of the conduit that inhibits extrusion. Regime 3 consists of periodic solutions, where the viscous plug is repeatedly extruded and replaced. Minimum and maximum extrusion rates (blue), and characteristic cyclic timescale (red), are plotted against enhanced permeability (k_{cr}). The value of the permeability defines the regime of the solution for a given set of otherwise fixed conditions. Note that country rock permeability has very little effect on the magnitude or frequency of the produced periodicity.

Reference conditions . . . .

Initial water content : α = 4.0 %
Initial crystal content : β = 45 %
Pressure at the inlet : P_{bot} = 122 Mpa
Temperature : T = 1223 K
Conduit radius : R = 15 m
Composition : 58.5 wt. % SiO_2

Legend

Period

Density

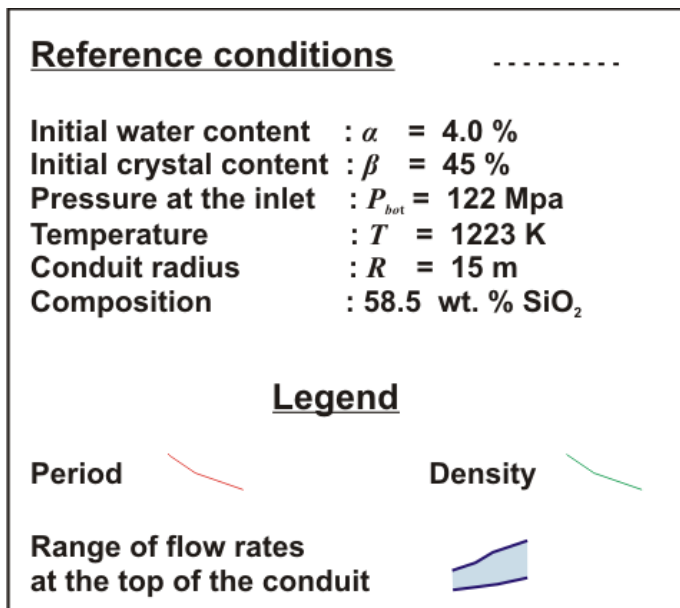Range of flow rates
at the top of the conduit

Figure 5.5 represents the results of model runs in which the main parameters were varied one at a time and the changes in period (red) and flow rate (blue) are plotted against the value of that parameter. Some parameters affect the viscosity of the mixture (temperature, initial water content, initial crystal content, composition), while others affect the inertial forces that drive the eruption (pressure at the bottom of the conduit and conduit radius). As demonstrated above, cyclic eruption for a typical basaltic andesite system is possible only for a narrow range of enhanced permeabilities. Values of enhanced permeability in a volcanic edifice are not well constrained and can vary across a range spanning several orders of magnitudes (Jaupart and Allègre, 1991). When changing a parameter, it was sometimes necessary to adjust the value of the enhanced permeability in order to remain in a periodic regime. These changes are documented on the figure.

In general, all changes that contribute to increasing the viscosity of the mixture (more silicic composition, higher initial phenocryst content, lower water content and lower temperature) produce solutions with lower flow rates and longer characteristic periods of repose. Similarly, a decrease in pressure at the bottom of the conduit also decreases the eruption rate and increases the characteristic cycle timescale. Temperature seems to have a very limited effect on cyclic activity, at least within the range explored here. In contrast, small changes in crystal content produce large variations, especially with regard to the flow rate. Runs with initial phenocryst contents of 30% produced solutions with extremely large flow rates at the top (thousands of $m^3 s^{-1}$).

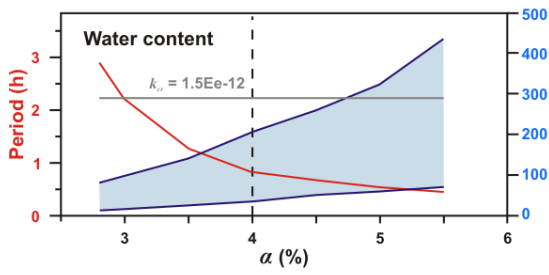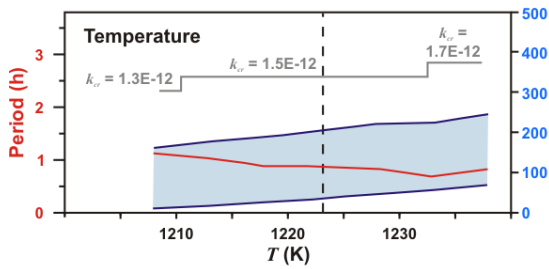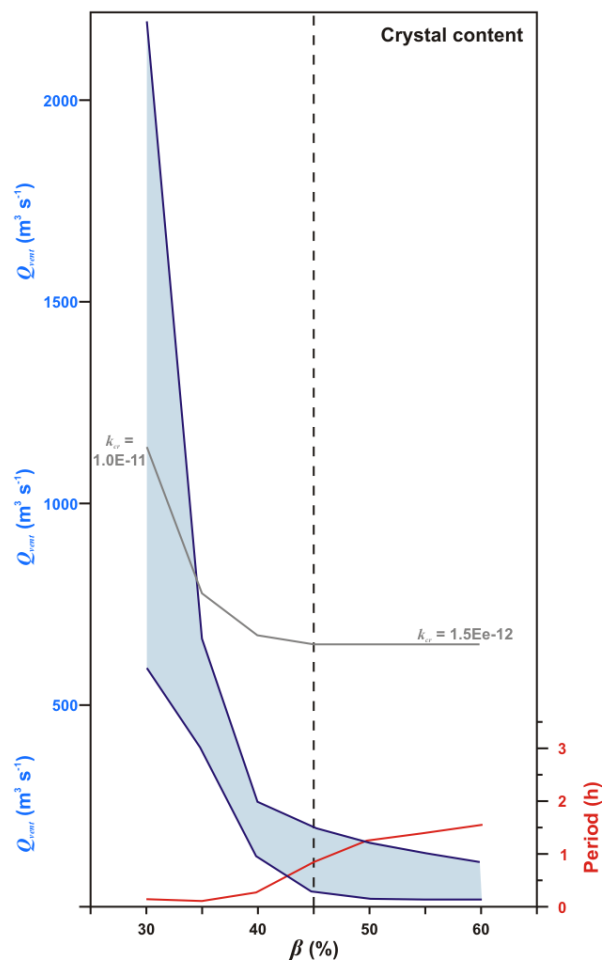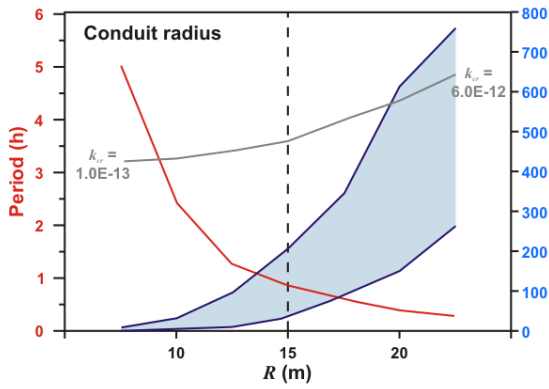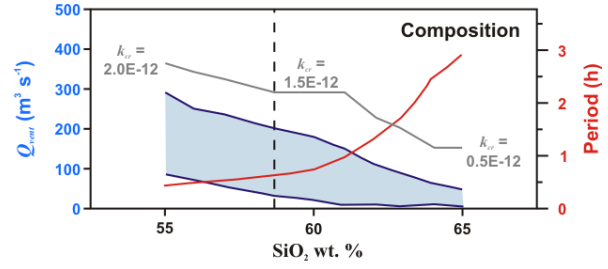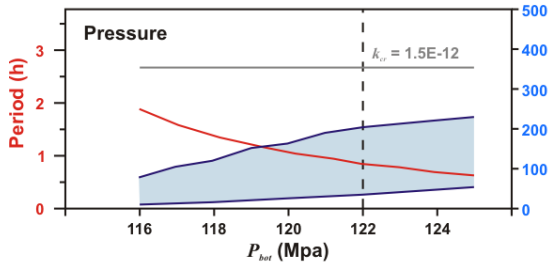**Figure 5.5 (previous page):** Results of the sensitivity analysis. The sensitivity of the model to various input parameters is tested systematically using a reference run with a set of starting conditions (listed in the legend below). For each plot, a single variable is varied around the value in the original run (black dashed line). Variations in the period (red line) and in the range of flow rate at the vent (Q_{vent}, two solid blue lines representing the minimum and maximum values enclosing a shaded area) are shown. Variations in composition are expressed in terms of SiO_2 wt. %. SiO_2 content is varied around the starting composition (Moore and Carmichael, 1998) while the content of other oxides are altered to conserve their relative proportions to one another. The value for the enhanced permeability through the country rock (k_{cr}) is adjusted in each run to produce periodicity. The gray line in each panel of the plot shows the adjustments made to that value as the considered parameter was changed. In general, more viscous conditions require higher values of k_{cr} in order to create an oscillating plug.

Reference conditions

Initial water content : α = 4.0 %
Initial crystal content : β = 45 %
Pressure at the inlet : P_{bot} = 122 Mpa
Temperature : T = 1223 K
Conduit radius : R = 15 m
Composition : 58.5 wt. % SiO_2

Legend

Period

Range of flow rates
at the top of the conduit
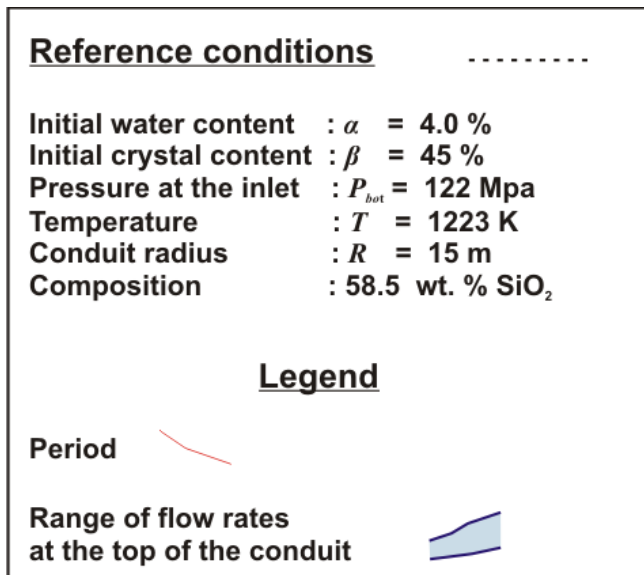
The conduit radius also has a strong influence. Smaller radii lead to a reduced flow rate, varying roughly with R^2 as expected. Smaller radii also increase the characteristic timescale of the oscillations, largely because the Poiseuille viscous term increases as R^{-1}. The influence of the melt composition is perhaps surprisingly moderate. However, large adjustments to the value of the enhanced permeability are required in order to accommodate the relatively small changes in composition shown here.
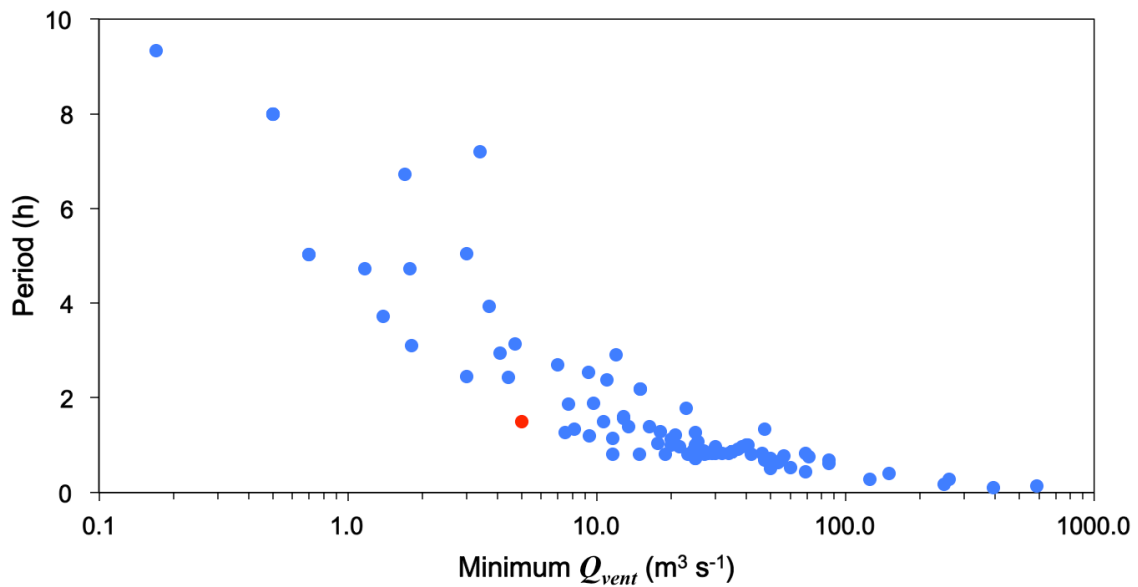

Figure 5.6: Inverse correlation between the periodicity and minimum flow rate produced by the model runs. The best match to the conditions observed at Semeru is highlighted in red.

Figure 5.6 illustrates the strong inverse correlation between period and extrusion rate for a basaltic andesite system represented here, which is best approximated by a logarithmic relationship. For that reason, exact reproduction of the cycles observed at Semeru was not achieved. The cycles at Semeru have periods varying from 10 mins to 1.5 h (Kazahaya et al., 2013; Smekens et al., 2015). Effusion rate for the volcano is assumed to be 0.2-2.8 m^3 s^{-1}, a value that was derived from satellite data in 2006 (Harris and Ripepe, 2007). Runs that produce relatively low flow rates in our simulations also exhibit large periods of several hours, while runs with periods under an hour usually correspond to large flow rates of several hundreds of m^3 s^{-1}. The best fit to the observed conditions for Semeru is illustrated in Figure 5.7. It has a minimum flow rate of ~5 m^3 s^{-1} and a characteristic timescale of repose of ~1.5h. The boundary and initial conditions for this run are listed in Table 5.3. Note that this run, contrary to all previous runs, features a dome pressure of ~2.6 MPa (dome height of ~ 118 m). I found that increasing the pressure of the dome, while keeping the pressure at the bottom of the conduit constant, decreases the period without affecting the flow rate in a significant manner. The peaks in flow rates in this run reached 95 m^3 s^{-1} after a strong acceleration that takes place during the "extrusion" of the plug. I interpret this sudden change in flow rate to be representative of explosive disruption of the plug.
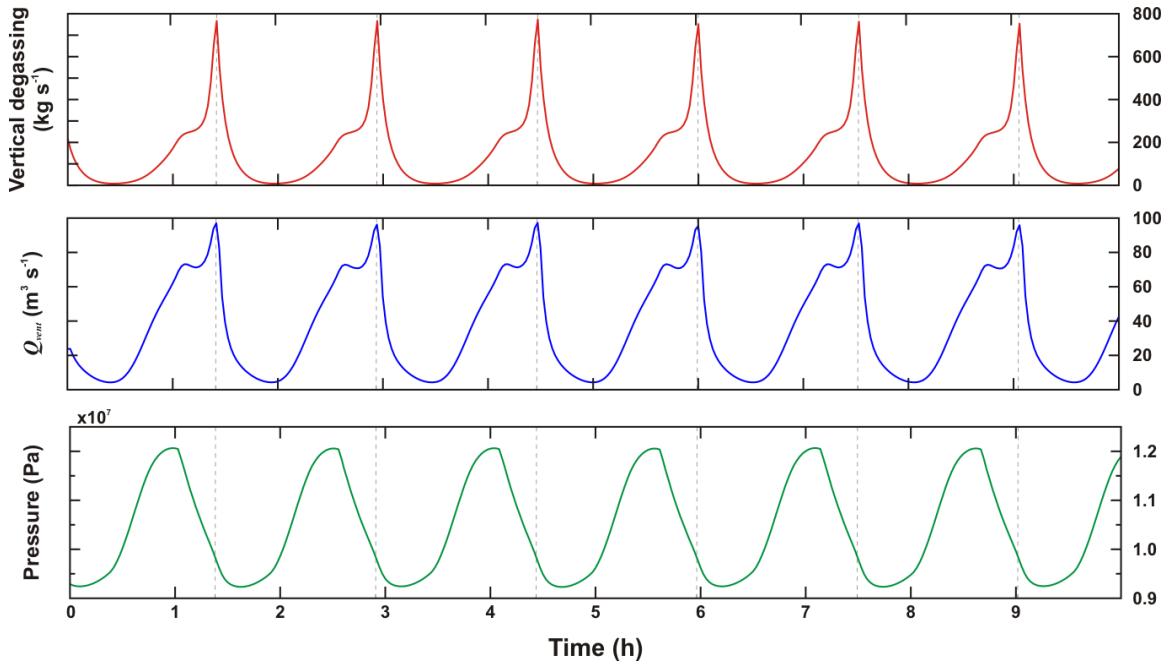
Figure 5.7: Results for the run with the best fit to the observations at Semeru. The following time series are plotted over the course of 10 h: Pressure at the base of the plug (z = 4750 m); Flow rate at the vent (blue); Vertical degassing at the vent (red). Dashed gray lines indicate the time of the maximum flow rate.

Parameter	Value
P_{bot}	117 Mpa
P_{dome}	2.6 Mpa
R	15 m
T	1223 K
α	4.0 wt. %
β	45 %
k_{cr}	1.0×10^{-12} m^2

Table 5.3: Initial and boundary conditions for the run with best fit to Semeru cycles.

146

In order to observe the relative timing of events in the conduit, Figure 5.8 shows the temporal evolution of four key system variables (normalized for clarity) on the same plot: flow rate at the conduit outlet (Q_{vent}), plug depth, overpressure at the bottom the plug (z = 4750 m), and vertical degassing. The figure also shows snapshots of the vertical distribution of density for the mixture (ρ_{mix}) and overpressure (difference between the magmatic pressure and the lithostatic pressure), at four time steps representative of the various stages of the cycle. At t = 0.4 h, the plug is fully formed and at its maximum thickness. The overpressure underneath it starts building up and drives the plug upward, extruding into or through the dome. At t = 1.07 h, the overpressure at the base of the plug reaches its maximum value. The plug itself is now thinner, but denser than at the beginning of the cycle, contributing to the build-up of overpressure. Once the pressure is able to overcome the viscous and gravitational forces, the plug is quickly extruded upwards. The third snapshot (t =1.4 h) is taken moments before the maximum flow rate is observed. At this stage, the densest part of the plug has not yet passed through the top of the conduit. Once it does, the flow rate rapidly increases to its maximum value (t = 1.5 h). The vertical profiles at this time show a small new plug reforming at depth, as the overpressure quickly drops.
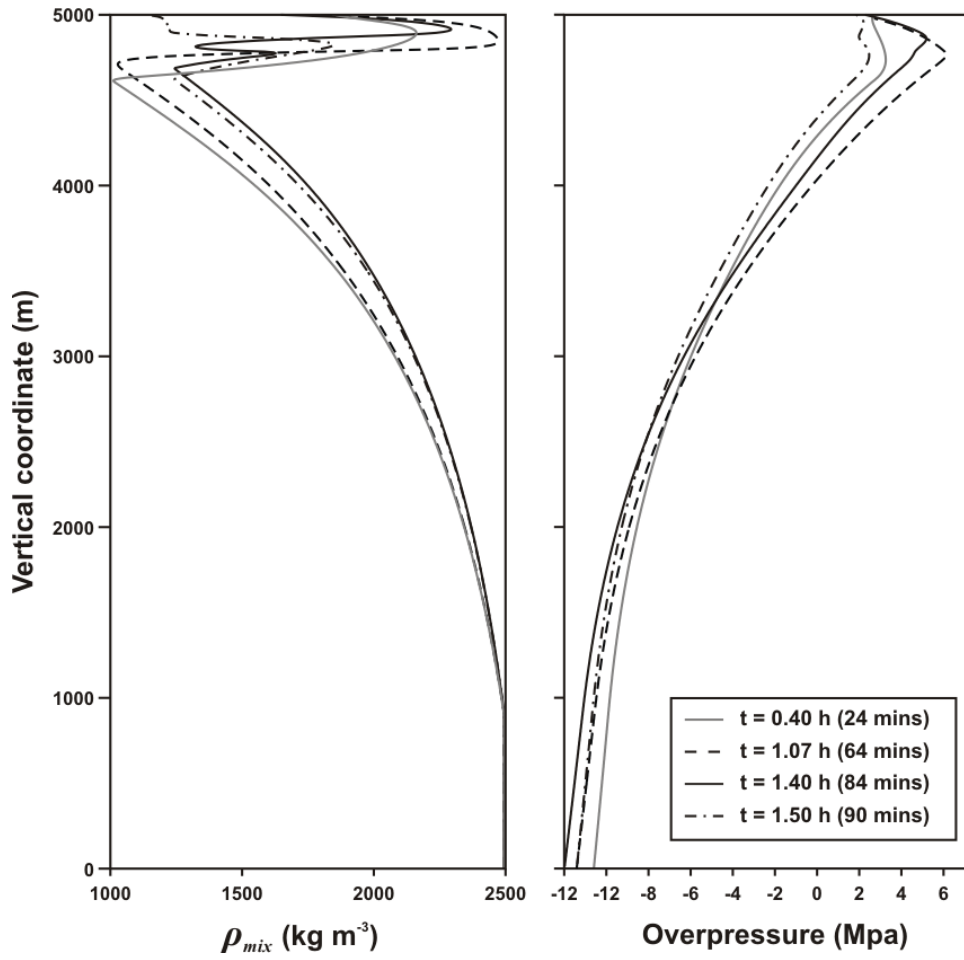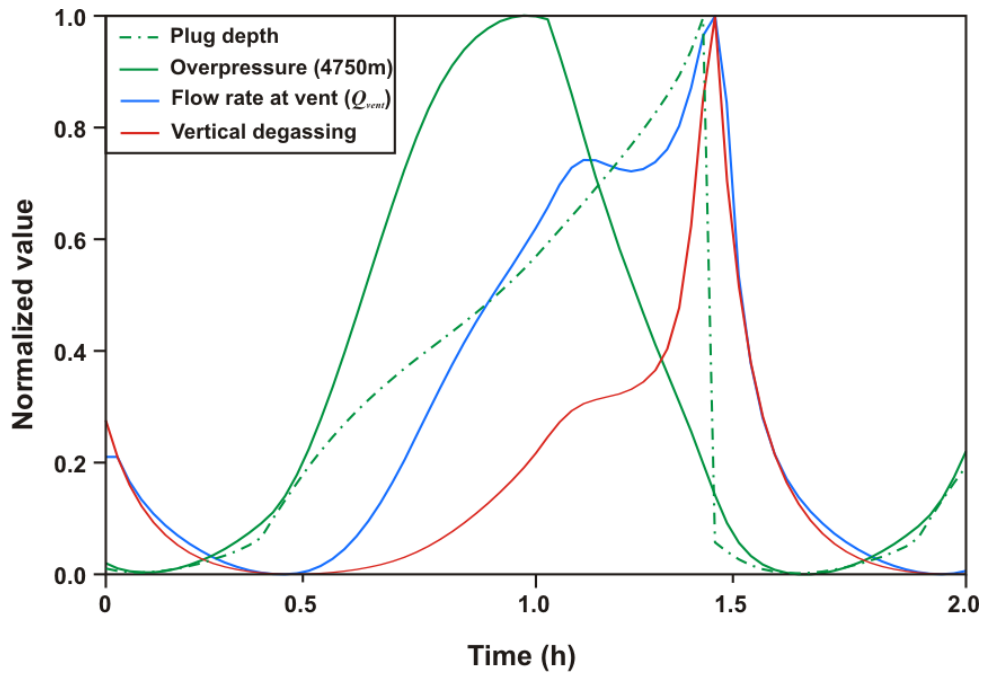
Figure 5.8 (previous page): Results of a run with best fit to the conditions observed at Semeru volcano, Indonesia. The top panel is a time series of four normalized key system variables over the course of an eruptive cycle: Plug depth (dotted green); Overpressure beneath the plug (solid green); Flow rate at the vent (blue); Vertical degassing (red). The bottom panel shows vertical profiles of the density (left) and overpressure (right) in the conduit, at four specific times during the cycle: t= 0.4 h corresponds to the largest overpressure beneath the plug; t = 1.07 h corresponds to the maximum density of the plug; t = 1.4 h is taken at the shoulder in the flow rate curve, when the densest part of the plug is being extruded; t = 1.5 h corresponds to the peak in flow rate and vertical degassing, and the creation of a new plug at depth.

5.4 Discussion

I was able to closely reproduce cycles of eruption observed at Semeru volcano using a model of magma ascent allowing the creation of a dense and viscous plug. The plug inhibits the flow of magma to the surface and creates a zone of large overpressure directly beneath it. The depth of this plug in my simulations is approximately 250 m, consistent with recent deformation observations made at the summit (Iguchi et al., 2008; Nishimura et al., 2012), which suggest a shallow depth of a few hundreds of meters for the pressure source producing the measured tilt. The maximum overpressure in our best fit run is ~ 5 MPa, similar to the overpressure produced during the runs for SHV (de' Michieli Vitturi et al., 2013). The cyclicity resulting from the repeated disruption and formation of this plug resulted in minimum effusion rates of ~5 m^3 s^{-1}; a value that is on the same order of magnitude as those measured by Harris and Ripepe (2007) using thermal satellite imagery in 2006 (0.1-2.8 m^3 s^{-1}). Repose interval in the best fit run is ~1.5 h, a value that lie at the upper bound of the range of repose intervals currently observed at Semeru (Smekens et al., 2015).

During the peak flow rates, vertical degasing reaches values of ~ 750-800 kg s^{-1}, while the average degassing rate outside of the peaks is ~ 0-50 kg s^{-1}. The value of the H_2O:SO_2 ratio is not known at Semeru volcano. However, SO_2 typically accounts for only a few percent of all emitted gases (e.g., Burton et al., 2007). By assuming an ad hoc H_2O:SO_2 mass ratio of 100:1, I calculate corresponding background SO_2 emission rates of

0-0.5 kg s^{-1}, with peaks of 7.5-8 kg s^{-1}, which are reasonable matches to our own observations at Semeru volcano (Smekens et al., 2015), where background levels of degassing were around 0.5 kg s^{-1}, with peaks at 6-8 kg s^{-1} (see Figure 5.9).
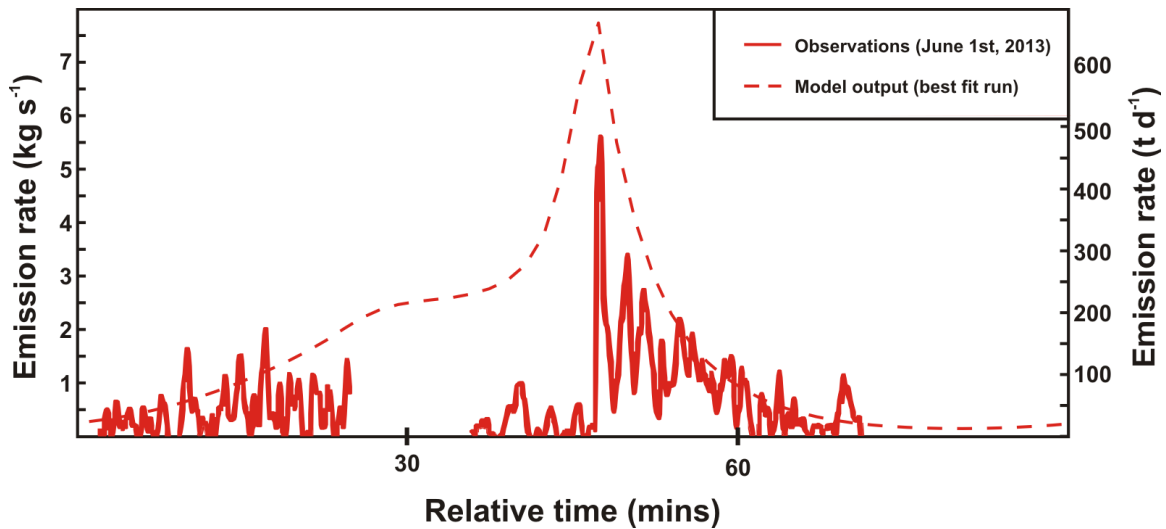
Figure 5.9: Comparison of SO$_2$ degassing patterns observed at Semeru [solid line] with emission patterns derived from model output [dashed line]. The modeled SO$_2$ degassing pattern was derived from H$_2$O degassing rates in the model output, assuming a fixed H$_2$O:SO$_2$ ratio of 100:1.

The model I used was originally designed to reproduce extrusion cycles at Soufrière Hills Volcano. The andesite system at SHV is much better constrained and the range of parameters considered in the original study (de' Michieli Vitturi et al., 2013) is narrower than those considered here. The basaltic andesite system studied here produces

151

cyclic eruptions at higher crystal contents, smaller conduit radii, and over a wider range of chamber pressures than the andesitic system. All of these changes are the direct consequence a dramatic decrease in the intensity of the viscous forces generated by the system as a result of the lower viscosity of the melt phase. This comparison suggests that periodicity can exist in more mafic systems with relatively lower chamber pressures, and may explain why these systems, such as Karymsky, Semeru, and Sakurajima, sometimes remain active for decades. As well, a wider range of timescales should be expected in a basaltic andesite system, when compared to more viscous systems. Variations in the viscosity of the melt introduced by changes in initial water content or volume fraction of phenocrysts are proportionally larger in a melt of andesitic composition (as is the case in this study), for which the starting viscosity can be up to three orders of magnitude lower than that of a rhyolite (the composition of the melt considered in the andesite system at SHV). Because the length of repose intervals in the produced periodicity is in large part controlled by the intensity of the viscous forces at the top of the conduit, the comparatively larger range of viscosities produced by a given range of initial conditions will result in a wider range of observed cyclicity (both in the magnitude of the flow rates at the vent and in the duration of the period between peaks).

In order to reduce the overall flow rate and produce periodicity, I had to consider much higher values of the enhanced permeability for the basaltic andesite system ($k_{cr} = 10^{-12}$ m^2) than for the andesitic system at SHV ($k_{cr} = 10^{-14}$ m^2). Moreover, while the andesitic system remains relatively stable for a fixed value of k_{cr}, I had to vary this value,

essentially tuning the intensity of the enhanced degassing that creates the plug to the specific conditions for each run. This sensitivity suggests that small variations in the initial conditions produce relatively large changes in the intensity of the viscous forces. Once a value is assumed for enhanced permeability, only a very specific and narrow combination of the initial conditions will produce periodicity. The magnitude and frequency of this periodicity are then defined primarily by the boundary conditions (P_{bot} and P_{top}), and the geometry of the conduit.

Sensitivity to Water Solubility Constant

The model also uses a solubility expression that was originally developed for rhyolitic melts where dissolved water content is expressed as a function of $\sqrt{P}$ and a pre-multiplying solubility constant. The solubility of water in a more mafic melt, such as the andesitic composition considered here is likely to be different. Moore et al. (1998) developed a relationship to calculate the solubility of water for a range of compositions, temperatures and pressure. Figure 5.10 shows the solubility profile (as a function of pressure) calculated using the Moore et al. (1998) relationship with the melt composition used in this study and at a temperature of 950°C. The simple Henry's law relationship considered in the model (also plotted for reference) overestimates the solubility of water when compared to a more realistic model for andesitic compositions. In an effort to understand the importance of this parameter, I performed a series of runs with Semeru-like conditions, using the best fit run described above as the starting point and changed

153

the value of the solubility constant in Henry's law from 4.11×10^{-6} Pa$^{-1/2}$ to 3.6×10^{-6} Pa$^{-1/2}$. This new value produces a solubility curve that more closely approximates the one computed with the Moore et al. (1998) relationship. The changes observed with this new solubility constant are consistent with the expected behavior of the system with respect to changes in the viscosity of the mixture. With a lower solubility along the entire vertical column, dissolved water content is decreased, leading to a mixture of higher viscosity. All other conditions being equal, a run with the revised solubility model produced a lower range of effusion rates (2-80 m^3 s^{-1}) and a slightly longer repose interval of 1.8h. Note that the two solubility curves are virtually identical below 10 MPa. These pressures are representative of the depth where the plug forms in the model. The overall lower solubility of the melt during ascent does however mean that a larger amount of exsolved volatiles are present when the magma reaches the zone of enhanced degassing at the top of the conduit. Similarly to what was done throughout this study, the value of the country rock permeability had to be increased in order to compensate for this effect and allow for the creation of the plug. Therefore, this change in solubility profile does not strongly influence the overpressures created below the plug, nor does it strongly affect the characteristic timescale of periodicity. Future work with the model will further explore of the parameter space with this revised solubility model, as well as examine the possible role of higher temperatures that may occur in basaltic andesite systems.
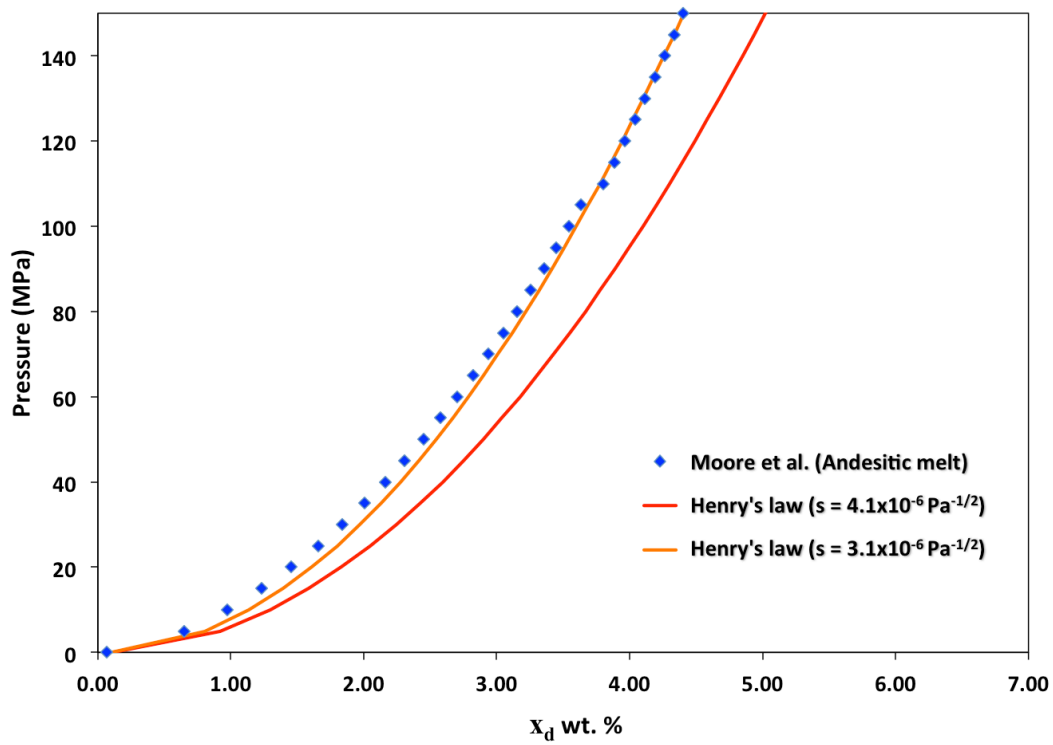
Figure 5.10: H$_2$O solubility model comparison. The solubility dependence used in DOMEFLOW is Henry's law, with a solubility constant of s = 4.1x10^{-6} Pa$^{-1/2}$ [red]. Solubility of H$_2$O in the melt can also be calculated for a melt of andesitic composition at 950°C (see Table 5.2) using the Moore et al. (1998) relationship [blue diamonds], which can be approximated by modifying the solubility constant in Henry's law to s = 3.6x10^{-6} Pa$^{-1/2}$ [orange curve].

CHAPTER 6

CONCLUSIONS

The detection and quantification of volcanic emissions of SO_2 is of special interest to both the atmospheric science and volcanology communities. The potential effect of SO_2 on climate has generated great interest in establishing global budgets of volcanic emissions to the atmosphere. Moreover, the emissions of other volcanic gases are typically derived from SO_2 fluxes. Satellite-based instruments are the ideal tools for this task, as they can provide repeated coverage of the entire Earth, and they have allowed the detection of volcanic events that would otherwise have remained unobserved. The intermittent nature and relatively small magnitude of persistently active explosive activity means that their emissions cannot be quantified by typical satellite methods and are usually ignored in global emission budgets, when in fact they represent an integral part of volcanic activity on any given day.

Most satellite sensors designed for global atmospheric observations lack the spatial resolution to observe persistent explosive volcanic activity. Instruments that do provide the necessary spatial resolution on the other hand, cannot provide frequent coverage, and often fail to capture individual, non-continuous explosions. Moreover, spatial resolution comes at the detriment of spectral resolution, thereby effectively decreasing the sensitivity of the retrieval methods. Using ASTER, the satellite-based instrument with the highest possible spatial resolution, I have shown that accurate

quantitative retrieval of the emissions at persistently active explosive volcanoes is often not possible. However, ASTER images can capture the volcanic events of interest, often containing evidence of more than one event in a single scene, making them clearly discernable in a qualitative manner. Unfortunately high amounts of ash and/or aerosols in the volcanic clouds closest to the vent render the plume opaque and prevent quantification. Moreover, these small plumes travel through the troposphere, where quantification is more difficult because most atmospheric emission in the thermal infrared occurs in the troposphere, where the atmosphere is densest. When plumes are measured in the stratosphere, the assumption can be made that the radiation measured at the sensor is similar to that exiting the top of the plume. For tropospheric plumes however, the radiation leaving the top of the plume is affected significantly by the slice of atmosphere above it, and the method becomes more sensitive to the exact determination of plume height and atmospheric profiles. In addition, and perhaps more interestingly, plumes emitted by these explosive events often remain within the boundary layer, where dynamic processes are enhanced. Consequent dilution and entrainment at that level can quickly lead to a decrease in SO_2 concentrations in the plume to undetectable levels. In addition, the chemical reactions that transform SO_2 into sulfuric acid aerosol operate faster in the troposphere, also contributing to the decrease of the measurable concentrations. I have documented this effect on a plume of passive emissions at Sakurajima volcano and measured depletion rates that fit at the higher end of observed values in the literature. For pulsatory events, where emissions are virtually null or extremely small between explosive eruptions, these depletion processes effectively

157

prevent the quantification of SO_2 in plumes at distances of more than ~5-10 km from the vent. Although satellite methods cannot quantify these depletion processes at all the volcanoes studied here, my satellite observations demonstrate that volcanoes that produce persistent and periodic explosive events may be able to serve as natural laboratories to quantify SO_2 depletion processes in the troposphere.

The difficulties illustrated above emphasize the importance of developing alternative methods to measure the SO_2 emissions at persistently active explosive volcanoes. Ground-based instruments offer the advantage of repeated and continuous measurements at selected volcanic centers. The proximity to the plumes also means that quantification of smaller amounts of SO_2 is possible. I presented the development of a ground-based instrument capable of measuring SO_2 emissions at very high frequency (up to 1 Hz), called the SO_2 camera. The SO_2 camera is an imaging system that measures radiation at two different wavelengths in the UV, and produces 2-D images of a drifting plume from the ground. Besides the high frequency of measurement, the advantages of the method include the possibility of calculating emission rates at various distances from the vent from a single observing location, and of directly determining the plume velocity from the images themselves. The dual filter approach also allows correction for the presence of ash and aerosols in the plume. Using this instrument, I was able to measure emissions of very low magnitude (< 0.1 kg s^{-1} or 8 t d^{-1}) at a coal-burning power plant in Arizona, and with an accuracy of ~ 20 %, providing the first validation of the method against an independently measured source. This exercise also emphasized the importance of selecting appropriate portions of the images to analyze for extracting emission rates.

The same near-vent effects that produce optically thick plumes affected the retrieval of SO_2 in the camera images, and I documented SO_2 depletion effects over spatial scales of only a few hundreds of meters. The SO_2 camera however, is the ideal instrument to study this type of effects, because the contextual information provided by the images allows for the calculation of emission rates all along the drift axis, leading to the most accurate determination of the source emissions.

With this new tool I documented the SO_2 emissions at Semeru volcano, a very active explosive volcano in Indonesia. Semeru typifies the style of activity that is the subject of this work. Its ongoing eruption started in 1967 and produces up to 50 explosions every day. The emissions at Semeru amount to a daily average of 7-21 t d^{-1}, corresponding to a yearly contribution of 8-26 Gg of SO_2 per year. This contribution represents 0.02-0.2 % of the total global yearly volcanic input of SO_2 to the atmosphere, depending on which study is considered. Those numbers may appear small, but they only represent the background activity of one specific volcano. Many other volcanic centers exist with similar activity, and similar or potentially larger emissions. A large part of the emissions are released during the explosive events (35-65%) with the remaining percentage emitted over the much longer repose periods (seconds- to minutes-long explosions compared to repose intervals up to 1.5 h), indicating that the system is not continuously openly degassing. The time series patterns of emissions show very low levels of degassing prior to the explosions, followed by a sharp increase, and in the case of one type of explosions (type II), an exponential return to baseline levels over a period

of ~ 15 minutes. This is consistent with the existence of a viscous plug at the top of the conduit. In this scenario, the plug seals the conduit prior to each explosion, preventing gases from escaping. The resulting pressure build-up ultimately overcomes the strength of the plug and leads to its disruption during the explosive release of gases.

I next explored the detailed mechanisms of viscous plug formation and destruction and the ways in which they control periodicity in a dome-building system similar to Semeru volcano. This possibility had been shown to be valid for an andesitic system at the Soufrière Hills Volcano (Montserrat). de' Michieli Vitturi et al. (2013) successfully reproduced the observed eruptive cycles with periods of 6-8 h using a 1-D transient numerical model of magma ascent. I modified the model for use with basaltic andesite composition, and found that periodicity occurs within a very narrow range of parameters. The intensity of the enhanced degassing at the top of the conduit strongly affects the existence of periodicity. Low permeability values lead to steady state eruptions in which the gas exsolved as the magma approaches the surface rapidly decreases the density of the mixture, and never allows for the formation of a plug. As enhanced permeability increases, a viscous plug is allowed to form at the top of the conduit and quickly leads to periodic behavior as it is repeatedly disrupted or extruded and reformed. With higher values of permeability however, the density of the viscous plug stalls the system and eruption is no longer possible. The magnitude and frequency of the periodicity are controlled by the viscosity of the magma, with lower viscosities leading to shorter periods and higher effusion rates. Following these findings, shorter

160

periods such as those observed at Semeru should be expected at more mafic systems. The effusion rates associated with these extremely short periods however, are not often observed at persistently active volcanoes, suggesting that additional mechanisms may be controlling the periodicity and extrusion rates.

This work demonstrates both the difficulty and importance of establishing detailed records of SO_2 emissions at persistently active explosive volcanoes. Variations in gas emissions during and between explosive cycles are key to understanding the degassing processes in the conduit, and continuous and repeated monitoring is essential to capture the inherent variability of emission at this type of volcano and accurately constrain their total emissions.

REFERENCES

Allard, P., Aiuppa, A., Burton, M., Caltabiano, T., Federico, C., Salerno, G. and La Spina, A., 2008. Crater gas emissions and the magma feeding system of Stromboli volcano. The Stromboli Volcano: An Integrated Study of the 2002-2003 Eruption: 65-80.

Allard, P., Carbonnelle, J., Metrich, N., Loyer, H. and Zettwoog, P., 1994. Sulphur output and magma degassing budget of Stromboli volcano. Nature, 368(6469): 326-330.

Andres, R. and Kasgnoc, A., 1998. A time-averaged inventory of subaerial volcanic sulfur emissions. Journal of Geophysical Research: Atmospheres (1984–2012), 103(D19): 25251-25261.

Bani, P., Oppenheimer, C., Tsanev, V.I., Carn, S.A., Cronin, S.J., Crimp, R., Calkins, J.A., Charley, D., Lardy, M. and Roberts, T.R., 2009. Surge in sulphur and halogen degassing from Ambrym volcano, Vanuatu. B Volcanol, 71(10): 1159-1168.

Barclay, J., Rutherford, M.J., Carroll, M.R., Murphy, M.D., Devine, J.D., Gardner, J. and Sparks, R.S.J., 1998. Experimental phase equilibria constraints on pre-eruptive storage conditions of the Soufriere Hills magma. Geophys Res Lett, 25(18): 3437-3440.

Barmin, A., Melnik, O. and Sparks, R.S.J., 2002. Periodic behavior in lava dome eruptions. Earth Planet Sc Lett, 199(1–2): 173-184.

Bluth, G.J., Doiron, S.D., Schnetzler, C.C., Krueger, A.J. and Walter, L.S., 1992. Global tracking of the SO2 clouds from the June, 1991 Mount Pinatubo eruptions. Geophys Res Lett, 19(2): 151-154.

Bluth, G.J.S. and Rose, W.I., 2004. Observations of eruptive activity at Santiaguito volcano, Guatemala. J Volcanol Geoth Res, 136(3-4): 297-302.

Bluth, G.J.S., Shannon, J.M., Watson, I.M., Prata, A.J. and Realmuto, V.J., 2007. Development of an ultra-violet digital camera for volcanic SO(2) imaging. J Volcanol Geoth Res, 161(1-2): 47-56.

Burton, M., Allard, P., Mure, F. and La Spina, A., 2007. Magmatic gas composition reveals the source depth of slug-driven Strombolian explosive activity. Science, 317(5835): 227-230.

Burton, M.R., Caltabiano, I., Mure, E., Salerno, G. and Randazzo, D., 2009. SO(2) flux from Stromboli during the 2007 eruption: Results from the FLAME network and traverse measurements. J Volcanol Geoth Res, 182(3-4): 214-220.

Campion, R., 2014. New lava lake at Nyamuragira volcano revealed by combined ASTER and OMI SO2 measurements. Geophys Res Lett, 41(21): 7485-7492.

Campion, R., Salerno, G.G., Coheur, P.-F., Hurtmans, D., Clarisse, L., Kazahaya, K., Burton, M., Caltabiano, T., Clerbaux, C. and Bernard, A., 2010. Measuring volcanic degassing of SO2 in the lower troposphere with ASTER band ratios. J Volcanol Geoth Res, 194(1–3): 42-54.

Carn, S., Krotkov, N., Krueger, A. and Yang, K., 2006. The first daily measurements of passive volcanic degassing from space, AGU Fall Meeting Abstracts, pp. 05.

Carn, S., Krueger, A., Krotkov, N., Yang, K. and Evans, K., 2009a. Tracking volcanic sulfur dioxide clouds for aviation hazard mitigation. Natural Hazards, 51(2): 325-343.

Carn, S.A., Pallister, J.S., Lara, L., Ewert, J.W., Watt, S., Prata, A.J., Thomas, R.J. and Villarosa, G., 2009b. The unexpected awakening of Chaitén volcano, Chile. Eos, Transactions American Geophysical Union, 90(24): 205-206.

Carn, S.A. and Pyle, D.M., 2001. Petrology and geochemistry of the Lamongan volcanic field, East Java, Indonesia: Primitive sunda arc magmas in an extensional tectonic setting? J Petrol, 42(9): 1643-1683.

Clarke, A.B., Stephens, S., Teasdale, R., Sparks, R.S.J. and Diller, K., 2007. Petrologic constraints on the decompression history of magma prior to Vulcanian explosions at the Souffiere Hills volcano, Montserrat. J Volcanol Geoth Res, 161(4): 261-274.

Corradini, S., Merucci, L. and Prata, A.J., 2009. Retrieval of SO2 from thermal infrared satellite measurements: correction procedures for the effects of volcanic ash. Atmos. Meas. Tech., 2(1): 177-191.

Costa, A., 2005. Viscosity of high crystal content melts; dependence on solid fraction. Geophys Res Lett, 32(22): 5-5.

Costa, A., Melnik, O. and Sparks, R.S.J., 2007a. Controls of conduit geometry and wallrock elasticity on lava dome eruptions. Earth Planet Sc Lett, 260(1–2): 137-151.

Costa, A., Melnik, O., Sparks, R.S.J. and Voight, B., 2007b. Control of magma flow in dykes on cyclic lava dome extrusion. Geophys Res Lett, 34(2): L02303.

Costa, A., Wadge, G., Stewart, R. and Odbert, H., 2013. Coupled subdaily and multiweek cycles during the lava dome eruption of Soufrière Hills Volcano, Montserrat. Journal of Geophysical Research: Solid Earth, 118(5): 1895-1903.

Couch, S., Sparks, R.S.J. and Carroll, M.R., 2003. The Kinetics of Degassing-Induced Crystallization at Soufrière Hills Volcano, Montserrat. J Petrol, 44(8): 1477-1502.

Dalton, M.P., Watson, I.M., Nadeau, P.A., Werner, C., Morrow, W. and Shannon, J.M., 2009. Assessment of the UV camera sulfur dioxide retrieval for point source plumes. J Volcanol Geoth Res, 188(4): 358-366.

de' Michieli Vitturi, M.D., Clarke, A.B., Neri, A. and Voight, B., 2010. Transient effects of magma ascent dynamics along a geometrically variable dome-feeding conduit. Earth Planet Sc Lett, 295(3-4): 541-553.

de' Michieli Vitturi, M., Clarke, A.B., Neri, A. and Voight, B., 2013. Extrusion cycles during dome-building eruptions. Earth Planet Sc Lett, 371–372(0): 37-48.

Eatough, D.J., Caka, F.M. and Farber, R.J., 1994. The Conversion of SO2 to Sulfate in the Atmosphere. Israel Journal of Chemistry, 34(3-4): 301-314.

Fischer, T.P., Morrissey, M.M., Calvache, M.L., Gomez, D., Torres, R., Stix, J. and Williams, S.N., 1994. Correlations between So2 Flux and Long-Period Seismicity at Galeras Volcano. Nature, 368(6467): 135-137.

Fischer, T.P., Roggensack, K. and Kyle, P.R., 2002. Open and almost shut case for explosive eruptions: Vent processes determined by SO2 emission rates at Karymsky volcano, Kamchatka. Geology, 30(12): 1059-1062.

Fleischmann, O.C., Hartmann, M., Burrows, J.P. and Orphal, J., 2004. New ultraviolet absorption cross-sections of BrO at atmospheric temperatures measured by time-windowing Fourier transform spectroscopy. Journal of Photochemistry and Photobiology A: Chemistry, 168(1): 117-132.

Frins, E., Ibrahim, O., Casaballe, N., Osorio, M., Arismendi, F., Wagner, T. and Platt, U., 2011. Ground based measurements of SO2 and NO2 emissions from the oil refinery, Journal of Physics: Conference Series. IOP Publishing, pp. 012083.

Galle, B., Oppenheimer, C., Geyer, A., McGonigle, A.J.S., Edmonds, M. and Horrocks, L., 2003. A miniaturised ultraviolet spectrometer for remote sensing of SO2 fluxes: a new tool for volcano surveillance. J Volcanol Geoth Res, 119(1–4): 241-254.

Giordano, D., Russell, J.K. and Dingwell, D.B., 2008. Viscosity of magmatic liquids: A model. Earth Planet Sc Lett, 271(1–4): 123-134.

Graf, H.F., Feichter, J. and Langmann, B., 1997. Volcanic sulfur emissions: Estimates of source strength and its contribution to the global sulfate distribution. Journal of Geophysical Research: Atmospheres (1984–2012), 102(D9): 10727-10738.

Granat, L., Rodhe, H. and Hallberg, R., 1976. The global sulphur cycle. Ecological Bulletins: 89-134.

Halmer, M.M., Schmincke, H.U. and Graf, H.F., 2002. The annual volcanic gas input into the atmosphere, in particular into the stratosphere: a global data set for the past 100 years. J Volcanol Geoth Res, 115(3-4): 511-528.

Harris, A., Rose, W. and Flynn, L., 2003. Temporal trends in lava dome extrusion at Santiaguito 1922–2000. B Volcanol, 65(2-3): 77-89.

Harris, A.J.L. and Ripepe, M., 2007. Regional earthquake as a trigger for enhanced volcanic activity: Evidence from MODIS thermal data. Geophys Res Lett, 34(2).

Hess, K.U. and Dingwell, D.B., 1996. Viscosities of hydrous leucogranitic melts; a non-Arrhenian model. Am Mineral, 81(9-10): 1297-1300.

Hoblitt, R., Wolfe, E., Scott, W., Couchman, M., Pallister, J. and Javier, D., 1996. The preclimactic eruptions of Mount Pinatubo, June 1991. Fire and Mud: eruptions and lahars of Mount Pinatubo, Philippines: 457-511.

Hoblitt, R.P., 1986. Observations of the eruptions of July 22 and August 7, 1980, at Mount St. Helens, Washington. US Government Printing Office.

Holland, A.S.P., Watson, I.M., Phillips, J.C., Caricchi, L. and Dalton, M.P., 2011. Degassing processes during lava dome growth: Insights from Santiaguito lava dome, Guatemala. J Volcanol Geoth Res, 202(1–2): 153-166.

Iguchi, M., Yakiwara, H., Tameguri, T., Hendrasto, M. and Hirabayashi, J.I., 2008. Mechanism of explosive eruption revealed by geophysical observations at the Sakurajima, Suwanosejima and Semeru volcanoes. J Volcanol Geoth Res, 178(1): 1-9.

Jaquet, O., Sparks, R. and Carniel, R., 2006. Magma memory recorded by statistics of volcanic explosions at the Soufrière Hills volcano, Montserrat. Statistics in volcanology. IAVCEI Spec Pub, 1: 175-184.

Jaupart, C. and Allègre, C.J., 1991. Gas content, eruption rate and instabilities of eruption regime in silicic volcanoes. Earth Planet Sc Lett, 102(3): 413-429.

Jaupart, C. and Vergniolle, S., 1988. Laboratory models of Hawaiian and Strombolian eruptions. Nature, 331(6151): 58-60.

Johnson, J.B., Lees, J.M. and Gordeev, E.I., 1998. Degassing explosions at Karymsky Volcano, Kamchatka. Geophys Res Lett, 25(21): 3999-4002.

Kantzas, E.P., McGonigle, A.J.S., Tamburello, G., Aiuppa, A. and Bryant, R.G., 2010. Protocols for UV camera volcanic SO(2) measurements. J Volcanol Geoth Res, 194(1-3): 55-60.

Kazahaya, R., Mori, T. and Yamamoto, K., 2013. Separate quantification of volcanic gas fluxes from Showa and Minamidake craters at Sakurajima volcano, Japan. Bulletin of Volcanological Society of Japan, 58(1): 183-189.

Kellogg, W., Cadle, R., Allen, E., Lazrus, A. and Martell, E., 1972. The sulfur cycle. Science, 175(4022): 587-596.

Kern, C., Werner, C., Elias, T., Sutton, A.J. and Lübcke, P., 2013. Applying UV cameras for SO2 detection to distant or optically thick volcanic plumes. J Volcanol Geoth Res, 262(0): 80-89.

Kromminga, H., Voigt, S., Orphal, J. and Burrows, J., 1999. UV-visible FT spectra of OClO at atmospheric temperatures, Proceedings of the 1st European Symposium on Atmospheric Measurements from Space. ESA Special Publication.

Krotkov, N.A., Carn, S.A., Krueger, A.J., Bhartia, P.K. and Yang, K., 2006. Band residual difference algorithm for retrieval of SO 2 from the Aura Ozone Monitoring Instrument (OMI). Geoscience and Remote Sensing, IEEE Transactions on, 44(5): 1259-1266.

Le Guern, F., 1982. Les débits de CO 2 et de SO 2 volcaniques dans l'atmosphère. B Volcanol, 45(3): 197-202.

Lensky, N., Sparks, R., Navon, O. and Lyakhovsky, V., 2008. Cyclic activity at Soufrière Hills Volcano, Montserrat: degassing-induced pressurization and stick-slip extrusion. Geological Society, London, Special Publications, 307(1): 169-188.

Llewellin, E.W. and Manga, M., 2005. Bubble suspension rheology and implications for conduit flow. J Volcanol Geoth Res, 143(1–3): 205-217.

Lopez, T., Fee, D., Prata, F. and Dehn, J., 2013. Characterization and interpretation of volcanic activity at Karymsky Volcano, Kamchatka, Russia, using observations of infrasound, volcanic emissions, and thermal imagery. Geochemistry, Geophysics, Geosystems, 14(12): 5106-5127.

Mason, R., Starostin, A., Melnik, O. and Sparks, R., 2006. From Vulcanian explosions to sustained explosive eruptions: the role of diffusive mass transfer in conduit flow dynamics. J Volcanol Geoth Res, 153(1): 148-165.

Melnik, O. and Sparks, R., 2002. Dynamics of magma ascent and lava extrusion at Soufriere Hills Volcano, Montserrat. Geological Society, London, Memoirs, 21(1): 153-171.

Melnik, O. and Sparks, R.S.J., 1999. Nonlinear dynamics of lava dome extrusion. Nature, 402(6757): 37-41.

Moffat, A.J. and Millan, M.M., 1971. The applications of optical correlation techniques to the remote sensing of SO_2 plumes using sky light. Atmospheric Environment (1967), 5(8): 677-690.

Moore, G. and Carmichael, I.S.E., 1998. The hydrous phase equilibria (to 3 kbar) of an andesite and basaltic andesite from western Mexico: constraints on water content and conditions of phenocryst growth. Contrib Mineral Petr, 130(3-4): 304-319.

Moore, G., Vennemann, T. and Carmichael, I.S.E., 1998. An empirical model for the solubility of H_2O in magmas to 3 kilobars. Am Mineral, 83(1-2): 36-42.

Mori, T. and Burton, M., 2006. The SO2 camera: A simple, fast and cheap method for ground-based imaging of SO2 in volcanic plumes. Geophys Res Lett, 33(24): L24804.

Mori, T. and Burton, M., 2009. Quantification of the gas mass emitted during single explosions on Stromboli with the SO(2) imaging camera. J Volcanol Geoth Res, 188(4): 395-400.

Morrissey, M., Garces, M., Ishihara, K. and Iguchi, M., 2008. Analysis of infrasonic and seismic events related to the 1998 Vulcanian eruption at Sakurajima. J Volcanol Geoth Res, 175(3): 315-324.

Morrissey, M. and Mastin, L., 2000. Vulcanian eruptions. Encyclopedia of volcanoes: 463-475.

Nishi, K., Hendrasto, M., Mulyana, I., Rosadi, U. and Purbawinata, M.A., 2007. Micro-tilt changes preceding summit explosions at Semeru volcano, Indonesia. Earth Planets Space, 59(3): 151-156.

Nishimura, T., Iguchi, M., Kawaguchi, R., Surono, S., Hendrasto, M. and Rosadi, U., 2012. Inflations prior to Vulcanian eruptions and gas bursts detected by tilt observations at Semeru Volcano, Indonesia. B Volcanol, 74(4): 903-911.

Oppenheimer, C., 2003. Climatic, environmental and human consequences of the largest known historic eruption: Tambora volcano (Indonesia) 1815. Progress in Physical Geography, 27(2): 230-259.

Oppenheimer, C., Francis, P. and Stix, J., 1998. Depletion rates of sulfur dioxide in tropospheric volcanic plumes. Geophys Res Lett, 25(14): 2671-2674.

Ozerov, A., Ispolatov, I. and Lees, J., 2003. Modeling Strombolian eruptions of Karymsky volcano, Kamchatka, Russia. J Volcanol Geoth Res, 122(3-4): 265-280.

Papale, P. and Dobran, F., 1993. Modeling of the ascent of magma during the plinian eruption of Vesuvius in A.D. 79. J Volcanol Geoth Res, 58(1–4): 101-132.

Platt, U. and Stutz, J., 2008. Differential Absorption Spectroscopy, Differential Optical Absorption Spectroscopy. Physics of Earth and Space Environments. Springer Berlin Heidelberg, pp. 135-174.

Prata, A., Rose, W., Self, S. and O'Brien, D., 2003. Global, long-term sulphur dioxide measurements from TOVS data: A new tool for studying explosive volcanism and climate. Volcanism and the Earth's Atmosphere: 75-92.

Prata, A.J., 1989. Observations of volcanic ash clouds in the 10-12 μm window using AVHRR/2 data. Int J Remote Sens, 10(4-5): 751-761.

Prata, F., Carn, S., Fromm, M. and Krotkov, N., 2008. A-Train satellite observations of the 2008 Chaitén eruption clouds, AGU Fall Meeting Abstracts, pp. 2183.

Pugnaghi, S., Gangale, G., Corradini, S. and Buongiorno, M.F., 2006. Mt. Etna sulfur dioxide flux monitoring using ASTER-TIR data and atmospheric observations. J Volcanol Geoth Res, 152(1-2): 74-90.

Rampino, M.R. and Self, S., 1992. Volcanic Winter and Accelerated Glaciation Following the Toba Super-Eruption. Nature, 359(6390): 50-52.

Realmuto, V.J., Abrams, M.J., Buongiorno, M.F. and Pieri, D.C., 1994. The Use of Multispectral Thermal Infrared Image Data to Estimate the Sulfur-Dioxide Flux from Volcanos - a Case-Study from Mount Etna, Sicily, July 29, 1986. J Geophys Res-Sol Ea, 99(B1): 481-488.

Rivera, C., Sosa, G., Wöhrnschimmel, H., de Foy, B., Johansson, M.E. and Galle, B., 2009. Tula industrial complex (Mexico) emissions of SO 2 and NO 2 during the MCMA 2006 field campaign using a mobile mini-DOAS system. Atmospheric Chemistry and Physics, 9: 6351-6361.

Robock, A., 2002. The climatic aftermath. Science, 295(5558): 1242-1244.

Rodriguez, L.A., Watson, I.M., Edmonds, M., Ryan, G., Hards, V., Oppenheimer, C.M.M. and Bluth, G.J.S., 2008. SO(2) loss rates in the plume emitted by Soufriere Hills volcano, Montserrat. J Volcanol Geoth Res, 173(1-2): 135-147.

Rodriguez, L.A., Watson, I.M., Rose, W.I., Branan, Y.K., Bluth, G.J.S., Chigna, G., Matias, O., Escobar, D., Carn, S.A. and Fischer, T.P., 2004. SO2 emissions to the atmosphere from active volcanoes in Guatemala and El Salvador, 1999-2002. J Volcanol Geoth Res, 138(3-4): 325-344.

Rose, W.I., 1972. Santiaguito volcanic dome, Guatemala. Geol Soc Am Bull, 83(5): 1413-1434.

Rose, W.I., 1987. Volcanic activity at Santiaguito volcano, 1976–1984. Geological Society of America Special Papers 212: 17-28.

Ruiz, M., Lees, J.M. and Johnson, J.B., 2006. Source constraints of Tungurahua volcano explosion events. B Volcanol, 68(5): 480-490.

Sahetapy-Engel, S. and Harris, A., 2009. Thermal structure and heat loss at the summit crater of an active lava dome. B Volcanol, 71(1): 15-28.

Schnetzer, C.C., 1993. The contribution of explosive volcanism to global atmospheric sulphur dioxide concentrations. Nature., 366: 327-329.

Self, S., Wilson, L. and Nairn, I.A., 1979. Vulcanian Eruption Mechanisms. Nature, 277(5696): 440-443.

Sisson, T.W. and Layne, G.D., 1993. H2O in basalt and basaltic andesite glass inclusions from four subduction-related volcanoes. Earth Planet Sc Lett, 117(3–4): 619-635.

Smekens, J.-F., Burton, M.R. and Clarke, A.B., 2014. Validation of the SO2 camera for high temporal and spatial resolution monitoring of SO2 emissions. J Volcanol Geoth Res(0).

Smekens, J.-F., Clarke, A.B., Burton, M.R., Harijoko, A. and Wibowo, H.E., 2015. SO2 emissions at Semeru volcano, Indonesia: Characterization and quantification of persistent and periodic explosive activity. J Volcanol Geoth Res(0).

Smith, S.J., van Aardenne, J., Klimont, Z., Andres, R.J., Volke, A. and Delgado Arias, S., 2011. Anthropogenic sulfur dioxide emissions: 1850–2005. Atmos. Chem. Phys., 11(3): 1101-1116.

Sparks, R.S.J., 1978. Dynamics of Bubble Formation and Growth in Magmas - Review and Analysis. J Volcanol Geoth Res, 3(1-2): 1-37.

Stix, J., Torres, R., Narvaez, L., Cortes, G.P., Raigosa, J., Gomez, D. and Castonguay, R., 1997. A model of vulcanian eruptions at Galeras volcano, Colombia. J Volcanol Geoth Res, 77(1-4): 285-303.

Stoiber, R., Malinconico, L. and Williams, S., 1983. Use of the correlation spectrometer at volcanoes. Forecasting Volcanic Events. Elsevier, Amsterdam: 425-444.

Stoiber, R.E. and Jepsen, A., 1973. Sulfur dioxide contributions to the atmosphere by volcanoes. Science, 182(4112): 577-578.

Stoiber, R.E., Williams, S.N. and Huebert, B., 1987. Annual Contribution of Sulfur-Dioxide to the Atmosphere by Volcanos. J Volcanol Geoth Res, 33(1-3): 1-8.

Sutawidjaja, I., Wahyudin, D. and Kusdinar, E., 1996. Geological map of Semeru volcano, East Java (1: 50,000 scale). Direktorat Vulkanologi, VSI, Bandung.

Tamburello, G., Aiuppa, A., McGonigle, A.J.S., Allard, P., Cannata, A., Giudice, G., Kantzas, E.P. and Pering, T.D., 2013. Periodic volcanic degassing behavior: The Mount Etna example. Geophys Res Lett, 40(18): 4818-4822.

Tamburello, G., Kantzas, E.P., McGonigle, A.J. and Aiuppa, A., 2011. Vulcamera: a program for measuring volcanic SO2 using UV cameras. Ann Geophys-Italy, 54(2).

Thomas, H.E., Watson, I.M., Kearney, C., Carn, S.A. and Murray, S.J., 2009. A multi-sensor comparison of sulphur dioxide emissions from the 2005 eruption of Sierra Negra volcano, Galapagos Islands. Remote Sens Environ, 113(6): 1331-1342.

Thouret, J.C., Lavigne, F., Suwa, H., Sukatja, B. and Surono, 2007. Volcanic hazards at mount semeru, east java (Indonesia), with emphasis on lahars. B Volcanol, 70(2): 221-244.

Urai, M., 2004. Sulfur dioxide flux estimation from volcanoes using Advanced Spaceborne Thermal Emission and Reflection Radiometer - a case study of Miyakejima volcano, Japan. J Volcanol Geoth Res, 134(1-2): 1-13.

Vandaele, A., Simon, P., Guilmot, J., Carleer, M. and Colin, R., 1994. SO~ 2 absorption cross section measurement in the UV using a Fourier transform spectrometer. JOURNAL OF GEOPHYSICAL RESEARCH-ALL SERIES-, 99: 25-25.

Voigt, S., Orphal, J. and Burrows, J., 2002. The temperature and pressure dependence of the absorption cross-sections of NO_2 in the 250–800 nm region measured by Fourier-transform spectroscopy. Journal of Photochemistry and Photobiology A: Chemistry, 149(1): 1-7.

Wallace, P.J., 2005. Volatiles in subduction zone magmas: concentrations and fluxes based on melt inclusion and volcanic gas data. J Volcanol Geoth Res, 140(1–3): 217-240.

Williams, S.N., LOWE, D.R., STOIBER, R.E., GEMMELL, J.B., CONNOR, C.B., GARCIA, N. and LONDOÑO, A., 1986. Eruption of the Nevado del Ruiz volcano, Colombia, on 13 November 1985: gas flux and fluid geochemistry. Science, 233(4767): 964-967.

Williams, S.N. and Self, S., 1983. The October 1902 plinian eruption of Santa Maria volcano, Guatemala. J Volcanol Geoth Res, 16(1): 33-56.

Wright, R., Flynn, L.P., Garbeil, H., Harris, A.J.L. and Pilger, E., 2004. MODVOLC: near-real-time thermal monitoring of global volcanism. J Volcanol Geoth Res, 135(1–2): 29-49.

Yamamoto, H., Watson, I.M., Phillips, J.C. and Bluth, G.J., 2008. Rise dynamics and relative ash distribution in vulcanian eruption plumes at Santiaguito Volcano, Guatemala, revealed using an ultraviolet imaging camera. Geophys Res Lett, 35(8).